

https://dspace.org/

Textural variations in uranium-bearing sheeted leucogranites, with specific attention to “oxidation halos” from the Rössing mine, Namibia

Shaba, Timothy

2022

https://hdl.handle.net/10539/37052

Downloaded from a DSpace repository. https://dspace.org/

UNIVERSITY OF THE WITWATERSRAND, JOHANNESBURG

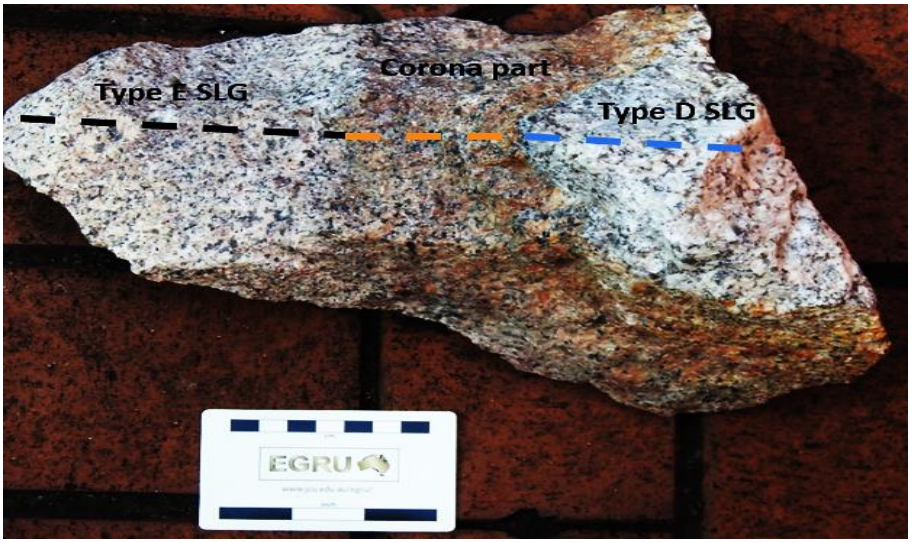
MSc. ECONOMIC GEOLOGY RESEARCH REPORT

SCHOOL OF GEOSCIENCES

TEXTURAL VARIATIONS IN URANIUM-BEARING SHEETED LEUCOGRANITES, WITH SPECIFIC ATTENTION TO "OXIDATION HALOS" FROM THE RÖSSING MINE, NAMIBIA.

BY

TIMOTHY SHABA



SUPERVISOR: PROFESSOR PAUL NEX

DECLARATION

I declare that this dissertation is my original work, except where due acknowledgement has been made. It is submitted for the degree of Masters in Economic Geology at the University of the Witwatersrand, Johannesburg. It has not been submitted before for any degree or examination in any other university.

Name: **Timothy Shaba**

Signature:…….

Date: …**14th July, 2022…..**

DEDICATION

This Dissertation is dedicated to my wife Patricia Gomani and my daughter Tiveness Shaba for your prayers, academic, moral and financial support during my stay at Wits in Johannesburg, South Africa. Through you, Tiveness Shaba, I always remember my late mother, Tiveness Nkhoma. Through our dedication, my wife, we have won the battle, and glory is to the Almighty God.

ABSTRACT

The Rössing Uranium Mine is ~60 km northeast of Swakopmund, Namibia, and it is one of the largest sheeted leucogranite-hosted primary uranium deposits in the world. The sheeted leucogranites (SLGs) are divided into six different types (A-F) based on field characteristics of colour, grain size, structural setting and mineralogy. Three pre-D_3 A-C types are barren, while post-D_3 D-F alaskites are undeformed and have potential for uranium mineralisation, especially types D and E. The E-type SLGs have notable diagnostic features; oxidation halos which occur in almost all uranium deposits in the southern Central Zone of the Damara Orogen, and have been mined for uranium since the establishment of the Rössing Uranium Mine in 1976. This project aims to document the textural variations of oxidation halos in relation to uranium mineralisation and distribution.

The Rössing uranium deposit is found within the southern Central Zone of the Damara Orogen which is composed of the Abbabis Metamorphic Complex (AMC) a Damaran-aged metasedimentary sequence and various granitic intrusions. The geology of the Rössing area comprises the Etusis, Khan, Rössing Formations and granitic intrusions. The primary uranium ore minerals at the Rössing Mine are uraninite and U-silicates. The mineralised uranium SLGs are typically found within the stratigraphic intervals of the Khan and Rössing Formations. Four techniques were used to analyse the rock samples: hand specimen observations; thin section petrographic analysis; Micro-XRF analysis to determine major element distribution of the whole E-type SLG rock sample and TIMA studies to determine mineral phases, elemental distribution, textural and alteration variations of the oxidation halos and their host rocks.

The results show that the grain size of the oxidation halos and their host rocks varies from fine to pegmatitic. In the oxidation halo sample, the D-type section and the oxidation halo core zone are pegmatitic; the E-type section has a coarse texture with centrimetric crystal sizes and the oxidation halo transition zones have a fine-grained texture. In the D-type SLG rock sample, TS1 sections 1, 3 and 6 have a fine texture, TS1 sections 2 and 5 exhibit pegmatitic textures and TS1 section 4 has a coarse-grained texture. Rock texture controlled uranium mineralisation and distribution, alteration rates and colour of the oxidation halo and their hosting rocks. The pegmatitic sections are less altered and have less abundant uranium (U)-bearing minerals. Whereas, the fine-grained textured sections are highly altered and they have abundant U-bearing minerals such as uranophane, uraninite and zircon. The pegmatitic-fine-grained textured interface acted as fluid traps, retaining more fluids for a long period causing intensive alteration of mineral phases characterising the finely-textured sections. In the pegmatitic sections, hydrothermal fluids were not retained for a long period, hence their low alteration. High abundance of U-bearing minerals in the fine-textured sections resulted in the presence of smoky quartz, which is responsible for light-dark variation in the D-type SLG rock sample. In the oxidation halo sample, red colouration is due to unequal distribution of iron oxides such as haematite and magnetite. The various alteration processes both rock samples were subjected to had three major effects: iron rich and primary U-bearing minerals were oxidised to form iron oxides and secondary U-bearing minerals, respectively; this promoted the rock permeability which in turn resulted in an uneven redistribution of U-bearing minerals across the rock samples; and controlled the rock colour variations. High abundance of uranium-bearing minerals in the oxidation halo transitional zones is a result of abundant biotite phases, whose alteration helped to provide Fe^{2+} to the REDOX system to reduce and precipitate more uranium-bearing minerals, and forming iron oxide phases such as haematite, magnetite, rutile and titanite as by-products.

ACKNOWLEDGMENTS

First and foremost, special thanks should go to my supervisor, Professor Paul Nex, for providing a fascinating research topic to work on, required materials, and guidance from the beginning of the research project to the final submission of my research report. Without your guidance and support, I could not finish this research project in time. May the Almighty God bless you for the excellent work you have done for me.

Many thanks to the Malawi Government through the Malawi University of Science and Technology for the financial opportunity to do my master's studies at Wits. To my family members, God bless you, my father Flywell Shaba, all my brothers- late Albert Shaba, Mapopa Shaba and Oliver Shaba for your endless well wishes and support all the time.

I would also like to thank all my lectures at Wits: Professor Judith Kinnaird, Professor Paul Nex, Dr Grant Bybee, Dr Robert Bolhar, and Dr Asinne Tshibubudze for lecturing me; I enjoyed your lectures, and to the lab technicians and analyst Mr Sam, Mr Caiaphas and Ms Nonku for the thin section preparation and TIMA analysis of the samples.

I am also so grateful to all my primary school teachers at Manthulu Full Primary School, secondary teachers at Kafukule Community Day Secondary School, Lozwati Private Secondary School and Euthini Secondary and Earth Sciences lectures (Dr Zuze Dulanya, Dr Charles Kankuzi, Dr Dyson Mosses, Mr Junior Chimphamba and Professor Cosmo Ngongondo) at Chancellor College, University of Malawi. However, not forgetting Mr Joel Kumwenda from Polytechnique College, University of Malawi, Mr Bosco Shaba and Mr Isaac Soko, you all have played a significant role in my current success.

TABLE OF CONTENTS

DECLARATION I
DEDICATION ii
ABSTRACT iii
ACKNOWLEDGMENTS iv
TABLE OF CONTENTS v
LIST OF FIGURES viii
LIST OF TABLES x
APPENDICES xi
ABBREVIATIONS AND ACRONYMS xii

CHAPTER ONE
INTRODUCTION

1.1 General Introduction 1
1.2 Oxidation halos 4
1.3 Previous studies 6
1.4 Research problem 6
1.5 Research aim 6
1.6 Research objectives 7
1.7 Justification 7

CHAPTER TWO
LITERATURE REVIEW

2.1 Introduction 8
2.2 Geology of the southern Central Zone 8
2.2.1 Abbabis Metamorphic Complex 8
2.2.2 Damara Supergroup 8
2.2.3 Granitoids and associated mineralisation of the Central Zone, Damara Orogen 10
2.2.4 Structural setting, granitic emplacement and metamorphism 10
2.2.5 Uranium mineralisation in the SLGs 11
2.2.6 Alteration of SLGS 12
2.3 Geology of the Rössing Area 13
2.3.1 Damara Supergroup 14
2.3.2 Structural setting, granitic intrusion and metamorphism 15
2.3.3 Mineralisation 15
2.4 Geology of the Goanikontes Area 16
2.4.1 Stratigraphy 16
2.4.2 Magmatism 17
2.4.3 Uranium mineralisation 17
2.5 Summary 18
2.5.1 southern Central Zone of the Damara Orogen 18
2.5.2 Rössing Area 18
2.5.3 Goanikontes Area 18

CHAPTER THREE
METHODOLOGY

3.1 Introduction……19
3.2 Hand specimen analysis……19
3.3 Thin section analysis……19
3.4 Micro-XRF analysis……22
3.5 TIMA (Tescan Integrated Mineralogical Analysis) ……23
3.6 Study limitations……24
3.7 Summary……24

CHAPTER FOUR
RESULTS

4.1 Introduction……25
4.2 Hand specimen observations……25
4.2.1 Textural features and mineralogy……25
4.3 Micro-XRF results……33
4.3.1 Textural variation for TS2 using µ-XRF elemental maps……33
4.3.2 Mineralogy of rock sample TS2 based on µ-XRF elemental maps……35
4.4 Thin Section Petrography……37
4.4.1 TS1 (D-type SLG) petrography……37
4.4.2 TS2 (oxidation halo) petrography……43
4.4.3 Petrography summary……51
4.5 TIMA results……52
4.5.1 BSE image result……53
4.5.2 Mineral phase maps results……54
4.5.3 Mineral phase proportion results……58
4.5.4 Mineral and alteration phase association……58
4.5.5 Alteration of mineral phases……62
4.5.6 TIMA Element Mapping……66
4.6 Summary of the results……71
4.6.1 Mineralogy……71
4.6.2 Rock colour change and alterations……72
4.6.3 Mineral grain size distribution and structures……72

CHAPTER FIVE

DISCUSSION

5.1 Introduction……73
5.2 Textural and structural features of the D-type SLG (TS1) and E-type SLG (TS2) ……73
5.3 Mineral composition, U-bearing minerals distribution and colour variation……74
5.4 Oxidation halo formation, alteration styles and distribution of U-bearing minerals……75
5.5 Texture relationship with alteration, colour variation and U-bearing minerals distribution……77

5.6 Correctness, validity and importance of the research results……77
5.7 Summary……78

CHAPTER SIX
CONCLUSIONS AND RECOMMENDATIONS

6.1 Introduction……79
6.2 Summary of the research findings……79
6.2.1 Mineralogy and rock colour variation……79
6.2.2 Rock texture and structures……80
6.2.3 Alteration……80
6.3 Conclusion remarks……80
6.4 Recommendations……81

REFERENCES……82
APPENDICES……86

LIST OF FIGURES

Figure 1.1: Map of southern Central Damara Zone showing uranium deposits……1
Figure 1.2: E-type SLG sample showing textural variation from D-type SLG part through the corona section to the E-type SLG part……5
Figure 2.1: Schematic emplacement illustration of primary mineralised SLGs in Central Zone of Damara Orogen……11
Figure 2.2: (A) Geological map of the main pit in the SJ area (B) Local geology of the Rössing Area showing the main anomalies (SH Area, SJ Area, SK Area) ……14
Figure 2.3: Geology of the Goanikonte Area west of Goanikontes Dome……17
Figure 3.1: Photograph of sample TS1 showing the division of D-type SLG based on textural variations……20
Figure 3.2: Hand specimen of rock sample TS1 (D-type SLG) showing the demarcation for thin section preparation……21
Figure 3.3: Photograph of sample TS2 showing section divisions of E-type SLG sample……21
Figure 3.4: Hand sample of rock sample TS2 (E-type SLG) showing the demarcation for thin section preparation……22
Figure 4.1: Graphical presentation of the mean grain sizes for TS1 measured using hand specimen observations……25
Figure 4.2: A graph showing average grain sizes distribution for TS2 sections……26
Figure 4.3: Photograph of sample TS1 showing the division of D-type SLG based on textural variations; TS1 sections 1, 3 and 6, TS1 sections 2 and 5, TS1 section 4……27
Figure 4.4: Section 6 of TS1 showing the association and distribution of the quartz and feldspar……28
Figure 4.5: TS1 section 4 showing some banding- smoky quartz and biotite forming dark layers……29
Figure 4.6: Photograph of sample TS2 showing section divisions of E-type SLG sample……30
Figure 4.7: TS2 section 1 mineral distribution and association and pegmatitic texture……31
Figure 4.8: Cross-section of oxidation halo section showing the core zone being dominated by pink feldspar while the boundary zone is dominated by smoky quartz……31
Figure 4.9: Hand sample of TS2 showing the oxidation halo section showing colour variation from D-type to the right to the E-type to the left……32
Figure 4.10: E-type section of sample TS2 showing mineral association of smoky quartz and pink feldspar……33
Figure 4.11: (A) TS2 whole rock sample Al, Ca, K and Si µ-XRF element map and (B) Mosaic showing mapped area in white rectangle……34
Figure 4.12: A graph showing the distribution of the mean grain sizes across the TS2 rock sample determined using µ-XRF elemental maps presented in Appendices 6 and 7……34
Figure 4.13: Micro-XRF element maps for (Si, K, Al, Fe, Mn, Zrn showing their distribution across sections of TS2 rock sample……36
Figure 4.14: TS1 sections 2 and 3 domains showing the occurrence of U-bearing minerals……40
Figure 4.15: TS1 sections 3 and 4 domains showing association of U-bearing minerals with biotite……41
Figure 4.16: Photomicrograph domains of TS1 section 4 showing uranium radiation and metamictisation alterations……42
Figure 4.17: Graphical presentation of the mean grain sizes for TS1 determined using full thin section images……43
Figure 4.18: Photomicrograph domain of TS2 section 2 (TS2-3) (XPL) showing the growth of albite exsolution yellow structures over microcline……45
Figure 4.19: Photomicrograph domain of TS2 section 4 (TS2-5) XPL image showing high association of

accessory U-bearing minerals such zircon with biotite……46
Figure 4.20: Photomicrograph domain of TS2 section 5 (TS2-3) XPL image showing iron oxide staining of albite as well as overgrowth of albite exsolution structures over microcline……47
Figure 4.21: Photomicrographs domains of TS2 section 4 (PPL) (A) and (B) is the same domain A but under rfl showing uraninite and (C) (XPL) domain of (B) showing the effects of uranium radiation alteration……48
Figure 4.22: Photomicrograph domain of TS2 section 5 (TS2-2) XPL image showing chloritised biotite being replaced by U-bearing minerals……49
Figure 4.23: Graphical presentation of the mean mineral grain sizes for TS2 determined using full thin section images……50
Figure 4.24: Photomicrograph domain of TS2 section 5 (TS2-3) XPL image showing myrmekite structure and iron oxide staining of plagioclase (haematisation)……51
Figure 4.25: BSE image domain for TS2 section 4 (TS2-5) representing various mineral phases found in both TS1 and TS2……54
Figure 4.26: Mineral phase maps showing distribution of various minerals in various thin section domains of various rock sample sections……57
Figure 4.27: A stacked bar graph showing distribution of major rock-forming mineral phase proportions for both TS1 and TS2 rock samples……58
Figure 4.28: A-B are mineral phase association graphs for TS1 sections 3 and 4, and C-E are mineral phase association graphs for TS2 sections 3, 4 and 5……61
Figure 4.29: Albite segment mineral phase map showing albite exsolution structures……62
Figure 4.30: Mineral segment phase map for kaolinite showing high kaolinite distribution in TS1 section 3 (TS1-2) (A) and low kaolinite distribution in TS2 section 4 (TS2-5) (B)……64
Figure 4.31: High muscovite distribution in TS1-2 (A) and low muscovite in low muscovite in TS2-6, indicating high sericitisation of TS1 compared to TS2……65
Figure 4.32: Elemental maps showing tin distribution in TS2 rock sample……68
Figure 4.33: Elemental maps for Si (quartz), Al (feldspar), K (orthoclase), Na (albite), Fe (haematite/magnetite) and Ti (titanite)……71

LIST OF TABLES

Table 1.1: Field characteristics of the six different SLGs……3
Table 2.1: A summary of stratigraphic sequence of the Damara Supergroup……..10
Table 3.1: Description of the rock samples……19
Table 3.2: Numbering of the thin sections prepared from both the TS1 and TS2 rock samples……..20
Table 3.3: A summary of µ-XRF settings used during the elemental mapping of the TS2 rock sample at the Mintek Mineralogy Laboratory……23
Table 3.4: Summary of the techniques used in analysing the rock samples……..24
Table 4.1: Modal proportions for quartz and feldspar determined using hand specimen observations……27
Table 4.2: Thin section descriptive summary results for rock sample TS1 (D-type SLG)……38
Table 4.3: Thin section petrographic analysis results for TS2 sample, the oxidation halo sample (E-type SLG……..44
Table 4.4: Description of the rock sample sections and domains selected for TIMA analysis……53
Table 4.5: Proportion of elements in sections of TS1 and TS2 rock samples……66

APPENDICES

Appendix 1: TS1-7 (XPL) full thin section image for TS1 section 5 showing quartz chains……86
Appendix 2: TS2-4 (XPL) full thin section image for TS2 section 4 showing two forms of quartz (Q1 and Q2), quartz chains, embayment contact and intergrowth relationship between quartz and feldspar……87
Appendix 3: TS2-5 PPL full thin section image for TS2 section 4 showing distribution of biotite in section……88
Appendix 4: Hand-specimen mineral grain size measurements for TS1 and TS2……89
Appendix 5: Descriptive statistics summary for TS1 and TS2 mineral size measurement results……89
Appendix 6: Mineral grain size measurements (mm) for TS2 sections using Micro-XRF elemental map……90
Appendix 7: TS2 descriptive statistic results for mineral grain sizes (mm)……90
Appendix 8: Mineral grain size measurements for TS1 using thin-section full images……90
Appendix 9: Descriptive statistics summary for TS1 mineral size measurement results……91
Appendix 10: Mineral grain size measurements for TS2 using full thin section images……91
Appendix 11: Descriptive statistics summary for TS1 mineral size measurements using full thin section images……91
Appendix 12: TS1 and TS2 mineral phases proportions (%) summary……91
Appendix 13: Specific areas chosen for TIMA analysis from various rock sample sections of TS1 and TS2……92

ABBREVIATIONS AND ACRONYMS

AMC: Abbabis Metamorphic Complex

AMICS: Advanced Mineral Identification and Classification Software

BSE: Back-Scattered Electrons

cps: counts per second

D_1…D_4: Deformation events phase 1, phase 2, phase 3 and phase 4

EDS: Energy Dispersive Spectroscopy

E-W: East-West direction

F_3 and F_4: Folding events associated with D_1 and D_4, respectively

FESEM: Field Emission Scanning Electron Microscope

HFSE: Highfield-strength elements

Ga: Billion years before present

GIMP: GNU Image Manipulation Program

Ma: Million years before present

Max: maximum

MSc: Masters of Science

NE: North-East direction

NNE: North-North-East direction

NW: North-West direction

PPL- Plane-polarised Light

REDOX: Reduction-Oxidation

REE: Rare Earth Elements

Rfl: Reflected light

TESCAN: Czech Republic Company producing scanning electron microscopes

TIMA: TESCAN Integrated Mineral Analyser

TS1: Timothy Shaba sample 1 (D-type SLG)

TS1-1...TS1-7: This section identity numbers prepared from various sample sections of TS1

TS2: Timothy Shaba sample 2 (E-type SLG with oxidation halo)

TS2-1…TS2-11: Thin section identity numbers prepared from various sample sections of TS2

SEM: Scanning Electron Microscope

SE: South-East direction

SLGs: Sheeted Leucogranites

S_o: Original sedimentary layering

S_1-S_4: Foliations formed during D_1 - D_4

XPL: Cross Polarized Light

XRF: X-ray fluorescence

U: Uranium

WIMLAB: Wits Imaging Laboratory

WAMLAB: Wits Automated Mineralogy Laboratory

</>: Lesser than/Greater than

$: United State Dollar

%: Percentage

Measurement units

Kv: Kilovolt

Km: Kilometre

lb: pound- a unit for measuring weight

m: metre

mbar- millibar

mm: millimetre

ms: millisecond

nA: nanoamphere

nm: nanometre

Pa: Power amplifier

pA: picoampere

µ: micro

µA: microampere

µm: micrometre

2D: Measurement in two dimensional

CHAPTER ONE

INTRODUCTION

1.1 General introduction

Primary uranium mineralisation occurs in the sheeted leucogranites (SLGs) in many uranium deposits in the southern Central Zone of the Damara Orogen, Namibia (Kruger and Kisters, 2016) (Figure 1.1). The uranium occurrences in SLGs include the well-known Rössing Uranium Mine, one of the world's largest granite-hosted primary uranium deposits and the world's longest-running open-pit uranium mine since its establishment in 1976 (Corvino and Pretorious, 2013). The Rössing Uranium Mine is situated approximately 60 km northeast of Swakopmund, Namibia (Basson and Greenway, 2004) (Figure 1.1).

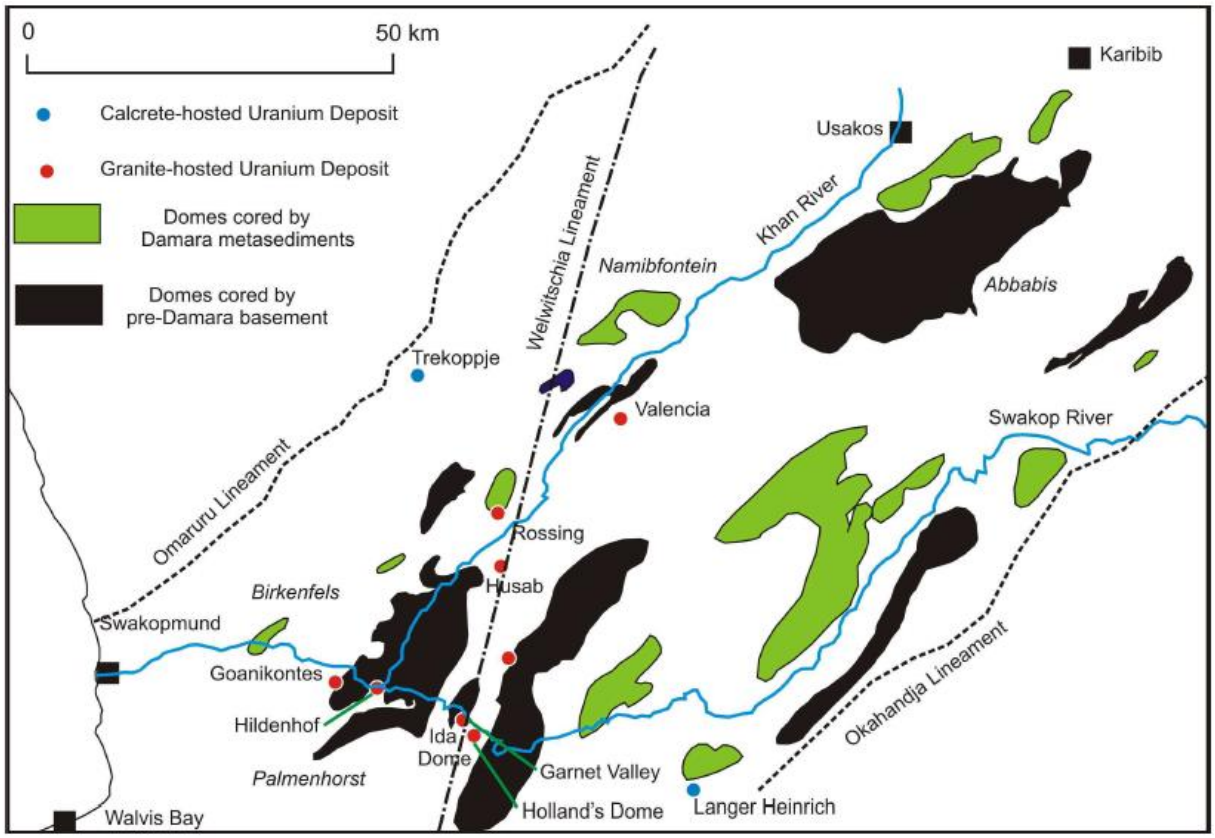


Figure 1.1: Map of southern Central Damara Zone showing uranium deposits (Kinnaird and Nex, 2007).

The SLGs consist essentially of quartz and feldspar, which may be a combination of microcline, perthite, albite, or oligoclase. They have less than 5% mafic minerals, and smoky quartz is diagnostic of high uranium content (Kinnaird and Nex, 2007). As with Goanikontes SLGs, the Rössing Mine SLGs are also divided into six types: A-type, B-type, C-type, D-type, E-type and F-type (Basson and Greenway, 2004). These SLGs are classified based on field characteristics of colour, grain size, structural setting and mineralogy together with whole rock geochemistry (Nex, 1997).

A-type SLGs are located within the NW dome limb of the Khan Formation. They have fine- to medium-grained texture and occur conformably to the S_3 foliations (Basson and Greenway, 2004). The B-type SLGs occur in the NW and SE dome of the Khan Formation, and they are strongly boudinaged with a weak S_3 foliation at the margins (Basson and Greenway, 2004). C-type SLGs are found within the NW and SE dome limbs of the Khan Formation and Etusis Formation in the dome core. They frequently occur at a high angle to foliation and pre-intruded granites. In some cases, they show pure shear and boudinaging with the partial development of weak S_3 foliation (Basson and Greenway, 2004). D-type SLGs are found within the dilated zones in the NW dome limb of Khan Formation, fault network in the Rössing Mine and highly attenuated Khan Formation streaming to the NE from the eastern edge of the dome core (Basson and Greenway, 2004). E-type SLGs occur in the fault network in the Rössing Mine, the dome core and the massive extensive outcrops to the southeast of the Rössing. The granites exhibit bifurcating body structures with variable grain sizes and colours (Basson and Greenway, 2004). Finally, the F-type SLGs are post-kinematic and exhibit parallel sides cross-cutting all the pre-existing structures. They are up to 30 m wide and may form massive tabular bodies (Basson and Greenway, 2004).

Of these six types (A-F), three pre-D_3 types are barren (A-C), while post-D_3 sheets (D-F) are undeformed and more prospective for uranium, especially types D and E (Nex, 2007). The SLGs range in colour from white, through cream, to grey or pink. According to Kinnaird and Nex (2007), the sheets are highly variable in texture, ranging from granophyric, aplitic and fine-, medium-, or coarse-grained granitic to pegmatitic. In size, the sheets vary from a few centimetres in width to over 100 m across and the larger sheets tend to show mineralogical banding (Freemantle, 2015). Table 1.1 summarises the field characteristics of the SLGs.

Table 1.1: Field characteristics of the six different SLGs (Nex, 1997; Kinnaird and Nex, 2007; Kinnaird and Nex, 2016).

Type	Description	Scintillometer measurements
A-type	Infrequent: thin <1 m wide, irregular in form, very light pink, cream to white, bedding-parallel, very few accessories, often foliated, folded, and boudinaged with prominent biotite streaks at the margins.	Low
B-type	Common: up to 10 m thick, light pink, garnetiferous, either medium- to fine-grained and homogeneous or pegmatitic with clear quartz. Often bedding parallel folded and boudinaged. Garnet occurs in clusters or as disseminated grains, mostly < 1 cm in size, with sillimanite in the pegmatitic facies within the Kuiseb Formation at Valencia.	Low
C-type (accessory-free)	Widespread, extensive sheets or coalescences of sheets, predominantly in upper Nosib and Swakop Groups, white to light pink, variably coarse-grained occasionally boudinaged, minimal accessories except entrained biotite.	Low
C-type (tourmaline)	Widespread, typically 2-5 m across. Light pink or white, mostly relatively coarse-grained to pegmatitic, occasionally boudinaged with massive tourmaline < 6 cm, often in clusters. Occur parallel to bedding in Kuiseb and Khan schists and gneisses.	Low
C-type (magnetite)	Uncommon, > 1m across, occur parallel to bedding/cleavage/foliation. Distinctive pink and white colour, medium to very coarse and pegmatitic in patches. Magnetite is the dominant accessory as clusters or disseminated. These may also have accessory tourmaline accompanied by clear quartz.	Low-high in patches
D-type	Common but localised sheeted intrusion, often at the Khan-Rössing boundary, extends into Chuos or higher where the Rössing Formation is attenuated or absent. White and black or grey patches, medium to coarse-grained homogeneous granular texture, sometimes banded smoky quartz, and very little accessory biotite. May have yellow uranium secondary phases on exposed surfaces and joint planes.	Very high
E-Type	Common but localised tabular, occasionally bifurcating, highly haematised light pink to deep red inhomogeneous. Smoky quartz, variable biotite concentration. Oxidation halo are interpreted to be hydrothermally altered D-types (Nex, 1997).	High-very high
F-type	Widespread, but not abundant. Tabular, parallel-sided, deep brick red to pink, coarse to pegmatitic, characteristic milky quartz, cross cuts most features and granites.	Low

The E-type SLGs have notable diagnostic features, oxidation halos (iron rings or coronas) noted by previous workers (Barnes, 1981; Corner, 1982; Nex, 1997; Kinnaird and Nex, 2007; Ashworth, 2014; Freemantle, 2015), and only minor work has been done to understand the genesis of these features. Oxidation halos are reported to occur from all uranium deposits in the Damaran southern Central Zone (Figure 1.1). The primary aim of this project is to document the petrology of textural transitions across an oxidation halo to try and further constrain how these enigmatic structures formed.

Granite-hosted uranium mineralisation in Damara Belt was first noted in the early 1920s by the occurrence of the mineral davidite near Rössing Mountain (Kinnaird and Nex, 2007; Kinnaird & Nex, 2016). After the Second World War, the nuclear age resulted in high demand for uranium for nuclear power and weapons production. Countries started intensive prospecting and exploration for

uranium worldwide in the 1950s, with Namibia and South Africa dominating uranium exploration in southern Africa (Freemantle, 2015). In 1955 several uranium occurrences were discovered in Namibia's Damara Orogen through airborne radiometric surveys, which are grouped into the Rössing, Trekkopje and the Langer Heinrich deposits (Roesener and Schreuder, 1994). In 1956 the Anglo-American Company prospected and explored the Rössing uranium deposit (Abraham, 2009). In the 1960s and 1970s there was a lack of oil supply from the Middle East producing areas because of a supply cut and as a direct result of armed conflict in the late 1970s. The lack of oil supply forced other countries to consider alternative energy sources including nuclear power, and the search for uranium further intensified (Freemantle, 2015). Later in 1966, Rio Tinto Company took a licence over the Rössing deposit. The company re-assessed the Rössing deposit and started mining uranium at the Rössing Mine in 1976 (Kinnaird & Nex, 2016).

An increase in uranium prices to over $120/lb in the early 2000s because of speculation and the expected shortfall of production against world consumption also helped to revive uranium exploration in the southern Central Zone (Freemantle, 2015). The increase in world uranium consumption during this period was due to the development and construction of new nuclear reactors worldwide (Kinnaird and Nex, 2007). Recent exploration activities have led to the discovery and development of more primary-hosted deposits such as the world-class Husab uranium deposit discovered in 2007 (Spivey et al., 2010).

This manuscript is organised into six chapters: Introduction, literature review, methodology, results and discussions and conclusion. The introduction chapter gives a general background of the study, oxidation halos and previous studies. The chapter also describes the research problem, objectives of the research and significance of the study. The Literature review provides an overview of both the regional and local geological setting of the Rössing Area, and it includes lithostratigraphic units, structural settings, metamorphism and uranium mineralisation. The methodology chapter explains the techniques used in analysing the rock samples. It also clarifies how data was analysed and the study limitations. The results and discussion chapter discusses and interprets the results presented in chapter four. The conclusion chapter summarises the research findings and gives recommendations for further studies to improve knowledge about the oxidation halos.

1.2 Oxidation halos

Oxidation halos are diagnostic features of E-type SLGs (Nex, 1997; Kinnaird and Nex, 2007; Ashworth, 2014; Freemantle, 2015). They are sub-ovoid or irregular in two-dimensional sections with a long axis or banding parallel to sheet orientation. The size of individual coronas varies from 0.5 to several metres in diameter (Nex, 1997). The oxidation halos are of two types; grey-cored and amorphous red-cored oxidation halos (Nex, 1997; Ashworth, 2014). According to Nex (2007), grey-cored oxidation halos are similar to D-type SLGs. The cores have well-defined reddened rims with the rim's internal boundaries, sometimes being gradational on a millimetric scale, while the external rim boundary is always gradational. Amorphous red cores comprise reddened and infrequently yellow-stained feldspar, abundant smoky quartz and a higher proportion of opaque minerals in relation to biotite (Nex, 1997; Ashworth, 2014). These red cores do not have well-defined margins and the colour variation grades into the rest of the sheet. The red cores always have higher counts per second (cps) on a scintillometer (max. 250) compared to the rest of the sheet (Nex, 1997).

Types E SLGs have an average counts per second (cps) of 20-40, but frequently contain high cps areas (100-300). The high counts occur within the oxidation halos but may also occur within smoky quartz trails or irregular reddened areas with a high proportion of opaque minerals. The reddened areas also have occasional surficial beta-uranophane and yellow-stained feldspars (Nex, 1997). Oxidation halos appear to be a late magmatic feature (Nex, 1997). This explanation agrees with Freemantle's (2015) observation in Garnet Valley, south of the Swakop River where prominent oxidation halos occur in the granitic pavement at some distance from the reactive marbles and skarns.

In trying to understand the phenomenon of oxidation halos, Corner and Henthorn (1978) carried out a paleomagnetic study on these features to establish their origin. It was noted that the cores of the oxidation halos have a similar mean direction of magnetisation to other Damara metamorphic rocks. Outside these halos, the mean direction of magnetisation is similar to that of the present-day earth's field. Based on the paleomagnetic results, the alaskitic granites enclosed by the oxidation halos are the original magmatic rocks. According to Corner and Henthorn (1978) the oxidation halos represent an encroaching alteration front that had already destroyed the Damara orogenic event's initial thermo-remnant magnetisation. Corner and Henthorn (1978) also concluded that the negative geomagnetic anomaly zones in which the uranium mineralised SLGs occur in the Damara belt formed because of hydrothermal/metasomatic alteration.

Textural variation is noted when moving from the D-type to the E-type of the oxidation halos (Figure 1.2). The texture changes from coarse-grained in the D-type SLG to the more equigranular, pink and finer-grained E-type SLG. This project also aims at understanding the textural variations of oxidation halos in relation to uranium mineralisation.

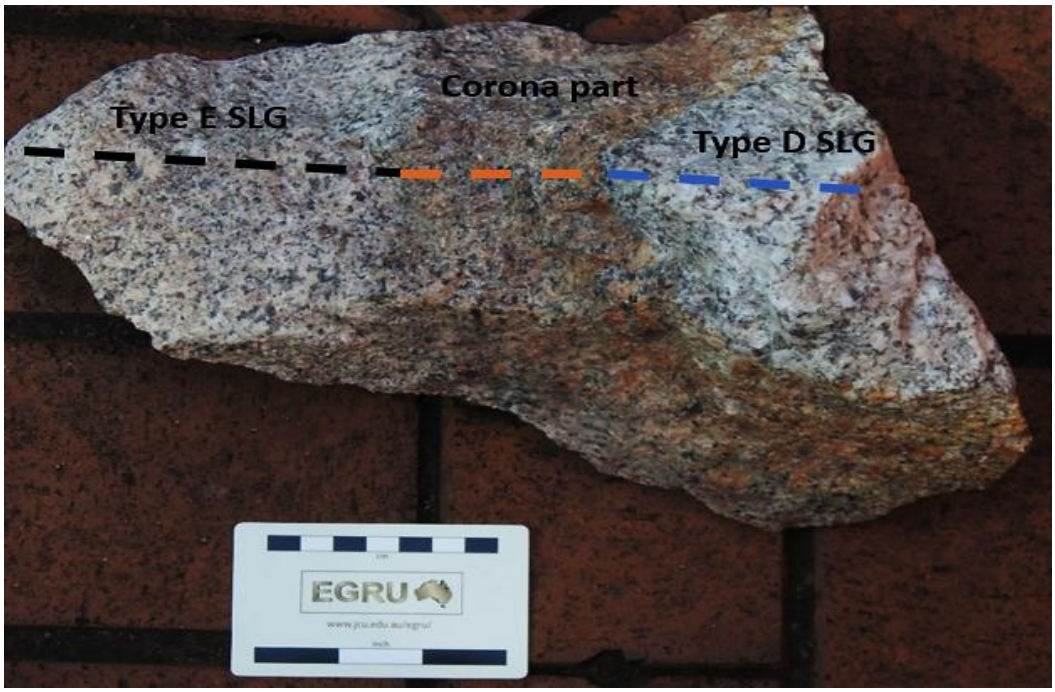


Figure 1.2: E-type SLG sample showing textural variation from D-type SLG part through the corona section to the E-type SLG part.

1.3 Previous studies

Since the beginning of the uranium exploitation at Rössing Mine in 1976, several studies have been conducted to understand the mineralised SLGs at the mine and the nearby deposits. According to Basson and Greenway (2004), these studies included understanding the petrogenesis, spatial correlations between uranium mineralisation and regional aeromagnetic lineaments (Corner, 1982, 1983, 2000; Jacob et al., 1986), the mineralogical and chemical processes operating during mineralisation and granite intrusion (Barnes and Hambleton-Jones, 1978; Cuney, 1980; Marlow, 1981; Miller, 1983a; Kerr, 1990; Mestres-Ridge, 1992; Bowden et al., 1995; Herd, 1997) and the metamorphic setting of sheeted granite emplacement (Jacob et al., 1986, 2000; Nex, 1997; Nex et al., 2001a). Basson and Greenway in 2004, also investigated the structural setting of uranium at Rössing Mine to understand the localisation of voluminous SLGs in the Rössing deposit. A similar study was done in 2007 by Kinnaird and Nex, who reviewed the geological controls on uranium mineralisation in SLGs of Damara Orogen. In 2009, Abraham also studied the Rössing deposit, focusing primarily on investigating the local geology and spatial distribution of primary and secondary mineralisation and variation in the composition of primary U-bearing minerals of the SK area.

Then in 2015, Freemantle also described the distribution of uraniferous SLGs, structural and fluid controls on uranium mineralisation in the Rössing area and the nearby deposits. The uranium deposits are near an Abbabis basement, and the mineralisation occurs within the Khan and Rössing Formations. The mineralised SLGs were emplaced during the transition from ductile to brittle deformation, and they intruded along existing fractures, faults, bedding planes, axial planes and axial planar cleavages. The Khan-Rössing contact boundaries acted as REDOX boundary where U^{6+} was being reduced and precipitated forming uraninite (Freemantle, 2015). Fluid composition controls also played a great role in precipitating uraninite in the SLGs. Through the de-carbonisation reaction, $CaCO_3 + SiO_2 = CaSiO_3$ (diopside, skarns) + CO_2, the CO_2 concentration was increased and this caused the melt/H_2O equilibrium to adjust by raising the silicate melt solidus to higher temperatures forcing the SLGs to crystallise within or below marble layers (Freemantle, 2015). This means that the SLGs were forming within the Khan-Rössing REDOX boundary where the dissolved uranium was being reduced and precipitated.

1.4 Research problem

Despite many studies done on the mineralised SLGs in the southern Central Damara Zone in the past, fewer petrological studies have been done on the diagnostic features of E-type SLGs of the Rössing Mine, the oxidation halos.

1.5 Research aim

The aim of this study is to document and interpret the petrological features of the mineralised oxidation halo and their hosting rocks in the Damaran southern Central Zone, particularly the Rössing Mine.

1.6 Research objectives

The following specific objectives were considered to achieve the principal aim of the study:

- To describe and document the texture and mineralogy of the oxidation halos and their host granitic material.
- To describe and document the distribution of U-bearing minerals in relation to the oxidation halos.

1.7 Justification

Even though the oxidation halos have been mined for uranium since the establishment of the Rössing Mine in 1976, no detailed study of this kind on the oxidation halos has been done to understand the role textural variation played in concentrating more U-bearing minerals in the diagnostic features of E-type SLGs, the oxidation halos. This research project has helped to bridge that knowledge gap by providing detailed information on the mineralogy and the distribution of U-bearing minerals in the oxidation halo and the hosting rocks in relation to their textural changes.

CHAPTER TWO

LITERATURE REVIEW

2.1 Introduction

This chapter gives an overview of the geological setting of the uranium mineralised SLGs of the Rössing area deposit and the regional geology of the southern Central Zone of the Damara Orogen.

2.2 Geology of the southern Central Zone

The Geology of the southern Central Zone comprises three main lithostratigraphic units: The Abbabis Metamorphic Complex (AMC), the Damara Supergroup and the associated granitic intrusions.

2.2.1 Abbabis Metamorphic Complex

The AMC is divided into the lower Tsawisis Formation, the Noab Formation and the upper Narubis Granitoid Complex (Brandt, 1987). The Tsawisis Formation is made up of the feldspathic quartzite, biotite schist and biotite-sillimanite with minor amphibole schist, marble and calc-silicate units (Brandt, 1987). The Noab Formation comprises a lower biotite schist member, a middle quartzite, marble and calc-silicate member and an upper metavolcanic member (Brandt, 1987). Finally, the Narubis Granitoid Complex contains numerous phases of granitic intrusions which were deformed to form the augen gneisses (Longridge, 2012).

2.2.2 Damara Supergroup

The Damara Supergroup is divided into two groups: The Nosib Group and the Swakop Group. The Nosib Group forms the base of the Damara Supergroup, and it is divided into the Etusis Formation and the overlying Khan Formation (Longridge, 2012; Ashworth, 2014). The Etusis Formation comprises quartzites, conglomerates and arkoses which were deposited in an extensive sandy braided river; and massive clinopyroxene and hornblende-bearing gneisses and calc-silicates (De Kock and Botha; 1988; Henry, 1992). Many of the outcrops of the Etusis Formation are wedge-shaped, suggesting that the deposition occurred in half-grabens (Miller, 2008). The Khan Formation comprises very fine-grained, thinly- to thickly- bedded and massive clinopyroxene and hornblende-bearing gneisses and calci-silicates (Miller, 2008; Longridge, 2012). The Khan Formation contains cyclical sedimentary units and structures formed by current action suggesting that the rocks were deposited in a low energy, distal fluvial system characterised by floodplains and ephemeral lakes (Henry, 1992). The metasedimentary lithologies of the Khan Formation show evidence of extensive metamorphism and metasomatism/hydrothermal alteration (Henry, 1992; Miller, 2008).

The Swakop Group overlies the older Nosib Group conformably, and it is divided into the Ugab Subgroup comprised of the Rössing Formation and the Khomas Subgroup comprised of the Chuos, Arandis, Ghaub, Karibib and Kuiseb Formations (Ashworth, 2014). In general, the lower Swakop Group commences with intercalated siliclastic, pelitic metasediments and pyritic quartzites toward

the top. The upper Swakop Group was deposited in a passive margin setting as the evolved into a seaway, where carbonate platforms were deposited forming shelves and peri-platforms at the edge of an abyssal plain (Longridge, 2012).

The Rössing Formation marks the first appearance of carbonate in the Damara Supergroup, and it is the lowermost unit of the Swakop Group (Longridge, 2012). Quartz-biotite and quartz-calc-silicates, pelitic schists and marbles dominate the Rössing Formation (Miller, 2008), which was deposited in a shallow marine environment such as an epicontinental marine platform (Henry, 1992). According to Henry (1992) and Nex (1997), the Rössing Formation shows high variability laterally, and its upper limit is bounded by an unconformity. The Chuos Formation overlies the Rössing Formation, and it is dominated by unsorted diamictite, with subordinate matrix-banded ironstones, quartzites, minor marble and pelitic units (Miller, 2008). The Chuos Formation is correlated with the world-wide Sturtian glaciation, which occurred at approximately 710 Ma (Hoffman, 2005). The Arandis Formation is divided into the Spes Bona (intercalated biotite schists and calc-silicates), Okawayo (turbidites, interbedded marbles, marble breccias, biotite schists and calc-silicate horizons) and Oberwasser Members (calc-silicates, metagreywackes, schists and carbonates). According to Stanistreet et al. (1991), the Arandis Formation units were deposited during a time of large-scale marine transgression and basin deepening. The extent of the Okawayo Member indicates that sedimentation occurred during a period of crustal stability in warm, shallow water (Badenhorst, 1992). The Ghaub Formation overlies the Oberwasser Member of the Arandis Formation, and it is comprised of diamictites and graded siltstones and shales and also dropstones (Miller, 2008). It is further divided into the Kachab Member composed of dropstone-bearing siliciclastic rocks and Daheim Member composed of metamorphosed alkaline, basic pillow lavas and pyroclastic rocks (Badenhorst, 1992). The glacial event preserved in the Ghaub Formation is correlated with the world-wide Marinoan glaciation, which occurred at about 635 Ma (Hoffmann, et al., 2004). The overlying Karibib Formation is mainly composed of marbles and dolomites, which were deposited during an extended period of marine transgression between 625 and 600 Ma (Miller, 2008). The Kuiseb Formation is the uppermost stratigraphic unit in the Swakop Group, which formed when the basin was increasing in size. It is composed of a very thick meta-turbidite sequence with fine- to coarse-grained biotite-rich quartzo-feldspathic schists being the dominant lithologies (Miller, 1983). The dominant lithologies in the formation are fine- to coarse-grained biotite-rich quartzo-feldspathic schists which contain cordierite, amphibole and sillimanite porphyroblasts (Miller, 2008). Table 2.1 summarises the stratigraphic succession sequence of the Damara Supergroup, which unconformably overlies the AMC.

Table 2.1: A summary of stratigraphic sequence of the Damara Supergroup (Smith, 1965; Nash, 1971; Miller, 1983(a); Hoffmann, 1987 (a); Henry, 1992; Hoffmann and Prave, 1996; Anderson and Nash, 1997; Nex 1997; Miller, 2008).

Damara Supergroup in the Central Zone				
Group	Subgroup	Formation	Lithologies	Thickness (m)
Swakop	Khomas	Kuiseb	Biotite-rich quartzo-feldspathic schist, biotite-garnet-cordierite schist, minor amphibolite schist, quartzite, calcsilicates and marble: basal graphitic schist with calcsilicate rock lenses (Tinkas Member)	3000
		Karibib	Marble, dolomite, biotite schist, quartz schist, calcsilicate rocks, shale.	700
		Ghaub Diamictite	Siliciclastics with drop stones, shales and mudstones, volcanic rocks,	<100 m
		Arandis Member	Schist, calcsilicate, marble, pelitic gneiss, quartzite	100
		Chuos	Mixite, diamictite, pebble- and boulder-bearing schist, minor quartzite, shale-BIF, schist.	700
	Discordance			
	Ugab	Rössing (Reducing Lithologies)[9]	Very variable: marble, quartzite, conglomerate, meta-greywacke, biotite schist, biotite-cordierite schist and gneiss, aluminous gneiss, biotite-hornblende schist, calcsilicate rocks.	200
Conformable transition with recognised REDOX boundary				
Nosib		Khan (some reducing Lithologies)	Pyroxene-amphibole feldspathic quartzite, amphibole-pyroxene gneiss, aluminous gneiss, biotite-hornblende schist, calcsilicate rocks.	1100
		Etusis	Pink-grey well-bedded feldspathic quartzite, arkoses, conglomerate, quartzo-feldspathic gneiss; minor biotite schist, marble, amphibolite, meta-rhyolite and calcsilicate rocks.	3500

2.2.3 Granitoids and associated mineralisation of the Central Zone, Damara Orogen

There are over 300 intrusions within the Central Zone; 96% are granitic intrusions and 4% are calc-alkaline gabbroic to granodioritic rocks (Kinnaird and Nex, 2007). The granitic intrusions are subdivided into the Red granite gneiss (oldest intrusions), Salem granites, Red granites, Grey granites and SLGs (youngest intrusions) (Abraham, 2009).

2.2.4 Structural setting, granitic emplacement and metamorphism

The southern Central Zone experienced high temperature and low-pressure conditions during the orogenesis that happened in four deformation phases (D_1 to D_4). High-temperature and low-pressure metamorphism were primarily due to the advective heat transfer by magmas derived from deeper structural levels during the early rifting stage (Mc Dermott, 1987). These deformation events were associated with regional metamorphism whose grade increases from the east towards the west, where it reaches high-grade conditions with local partial melting and exhibiting upper amphibolite to granulite facies near the Atlantic coast (Nex et al., 2001b; Longridge et al., 2009). The D_1 deformation produced tight isoclinal folds and developed widespread gneissosity, while D_2 resulted in more open folds (Longridge et al., 2009). There was further deformation during D_3, resulting in dome formation focused at the basement/cover interface, interpreted as a mid-crustal extensional detachment according to Oliver (1994). The D_4 deformation included modification of the

Rössing Dome orientation by anticlockwise rotation but also resulted in other domes in the Damara orogen to exhibit overturned south-western and north-eastern margins (Longridge et al., 2009). It was during the D_4 event when the NNE Welwitschia Lineament Trend (Figure 1) formed. The distribution of primary uranium deposits in the southern Central Damara Zone shows that there is a close association between the uranium deposits and the Welwitschia Lineament as most of these deposits occur close to or along this lineament (Oliver, 1994; Nex, 1997; Basson and Greenway, 2004; Freemantle, 2015).

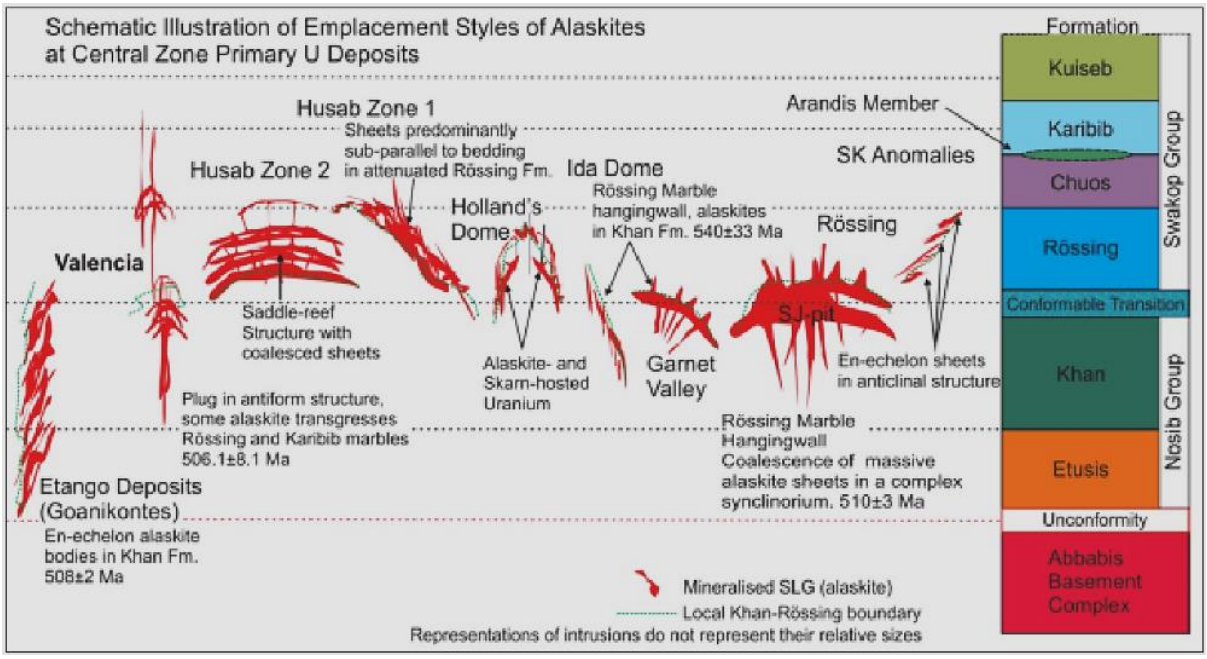


Figure 2.1: Schematic emplacement illustration of primary mineralised SLGs in the Central Zone of Damara Orogen (Freemantle, 2015).

Structurally, mineralised SLGs were emplaced during the transition from ductile to brittle deformation (Oliver, 1994; Nex, 1997; Basson and Greenway, 2004; Kinnaird and Nex, 2007; Freemantle, 2015). The SLGs intruded along the existing fractures, faults, bedding planes and axial planar cleavages. The stratigraphic intervals (Figure 2.1) where mineralised SLGs were emplaced formed REDOX contrasts between the magma and fluids and the country rocks (Freemantle, 2015). The stratigraphic REDOX boundaries played a critical role in reducing and crystallising uranium. The essential REDOX boundaries are between the Khan and Rössing Formations; the Khan and Chuos Formations where the Rössing Formation is absent, and sometimes in the sulphide-bearing reduced sediments of the Arandis Member occurring below the Karibib Formation (Figure 2.1) (Munro et al., 2011; Freemantle, 2015).

2.2.5 Uranium mineralisation in the SLGs

Uranium mineralisation in the Damaran southern Central Zone is stratigraphically controlled, which was in two-fold. First, the gneissic rocks provided the easiest pathway for the melt migration, while

the marbles, quartzites and schists of the Rössing (and Arandis) Formations provided a physical impediment to the melts, as well as hosting reduced minerals with which oxidised U-bearing magmas and fluids could react to precipitate uranium. Uraninite is the dominant primary uranium-bearing mineral with minor betafite and davidite, which may be locally abundant in the mineralised SLGs. The uraninite forms black, resinous subhedral to euhedral crystals, 3-5 mm in size in microcline or plagioclase, or at crystal boundaries between feldspar, quartz and biotite (Kinnaird and Nex, 2016). Uranium also occurs in secondary U-bearing minerals such as betauranophane, coffinite, matahaweeite, carnotite, gummite, thorogummite, autunite, uraniferous monazite, boltwoodite, torbernite and uranothallite (Kinnaird and Nex, 2007).

According to Cuney and Kyser (2008), sulphur^{-} plays an important role in reducing hydrothermal U into insoluble state, whereby the reduced sulphides provide Fe^{2+} and promote uraninite crystallisation. Where sulphide is absent or in low abundances, Fe tends to accompany uranium mineralisation. Oxidised iron is the most obvious indicator of uranium mineralisation in the leucogranites, as iron is the most likely reducing agent of soluble U in magmatic U systems (Cuney and Kyser, 2008). According to Walker (1956), in hydrometallurgical processes, Fe^{3+} is the principal reagent for the oxidation reaction required to oxidise U (IV) into soluble U (VI) before the sulphuric acid leach stage. This process would form Fe^{2+} minerals if the mixture were to solidify. In the deposition of uranium in the mineralisation system in the rock the opposite would have to happen, Fe^{2+} in minerals would donate electrons to U (VI) in order to reduce it to insoluble U (IV). In effect producing $Fe^{3+,}$ haematite as by-product of uranium mineral deposition.

The uraniferous SLGs host chlorite and epidote, and these minerals typically form from the breakdown of biotite (Waters, 1989; Moore and McStay, 1990). Freemantle (2015) noted that biotite and uraninite are closely associated at all of the Central Zone primary deposits, and the following observations were made: biotite in uraniferous granites is almost always chloritised as a result of late fluid alteration; biotite textures such as skeletal blades and irregular grain boundaries, biotite nests/enclaves occur in many uraniferous leucogranites; Altered biotite hosts exsolved magnetite-ilmenite, which may be indicators of relative oxidation-reduction conditions; biotite hosting uraninite inclusions are observed in samples from all the deposits in this study; and fluorite is particularly abundant as an inclusion in biotite, with the Husab deposits potentially hosting the highest concentrations. According to Freemantle (2015), these observations indicate that biotite was in variable equilibrium with the melt, that a significant component was entrained, and that biotite might have provided an important source of Fe to the REDOX system as a result of alteration. FeO-bearing minerals such as biotite and magnetite provide a source of reductants (undergoing oxidation- losing electrons) in soluble iron, promoting reduced (undergoing reduction- gaining electrons) type uranium minerals. These reactions are taking place at the fluid circulation stage and the role of REDOX control may be enhanced by pH at lower temperatures (Cuney and Kyser, 2008).

2.2.6 Alteration of SLGS

Several hydrothermal alteration events affected the mineralised SLGs at Goanikonte, Ida Dome, Valencia and Hildenhof (Freemantle, 2015), as well as in the Rössing area (Nex, 1997). The first alteration event was an alteration by a late-stage magmatic fluid. This alteration event involved sodic alteration characterised by rimmed plagioclase with myrmekite development, albite growth in microcline and mesoperthite exsolution in microcline. Silicification and de-silicification, corrosion of magnetite and uraninite, production of uranophane in the partially oxidised environment also

characterise the alteration by a late-magmatic fluid (Freemantle, 2015). The second alteration event took place after the last crystallisation of the granites. This alteration event was responsible for further oxidation of uraninite to uranophane and subsequent redistribution of the oxidised minerals along fractures and existing grain boundaries; and formation of new euhedral and anhedral quartz-veinlets at the expense of feldspars and intensive alteration of biotite to chlorite. It was also responsible for remobilisation and development of botryoidal haematite, minor albitisation of oligoclase, albite rim growth and zonation of plagioclases, and new mesoperthite development at the expense of tartan-twinned microcline (Freemantle, 2015). Alteration facilitated by the percolation of meteoric fluids via brittle fractures was the third alteration event, and it is very prominent in surface and near-surface rock samples (Freemantle, 2015). Then, there was a later stage alteration event which led to the development of new mica, sericite, saussurite and coarse muscovite in feldspar cleavages. At the surface, clays and calcite develop in the rock samples, whereas at depth, the rock samples are characterised by chlorite and epidote (Freemantle, 2015).

2.3 Geology of the Rössing Area

The geology of the Rössing area comprises the Damara Supergroup (Etusis, Khan and Rössing Formations) and granitic intrusions (Gray, 2015), and Figure 2.2 summarises the geology of the Rössing area.

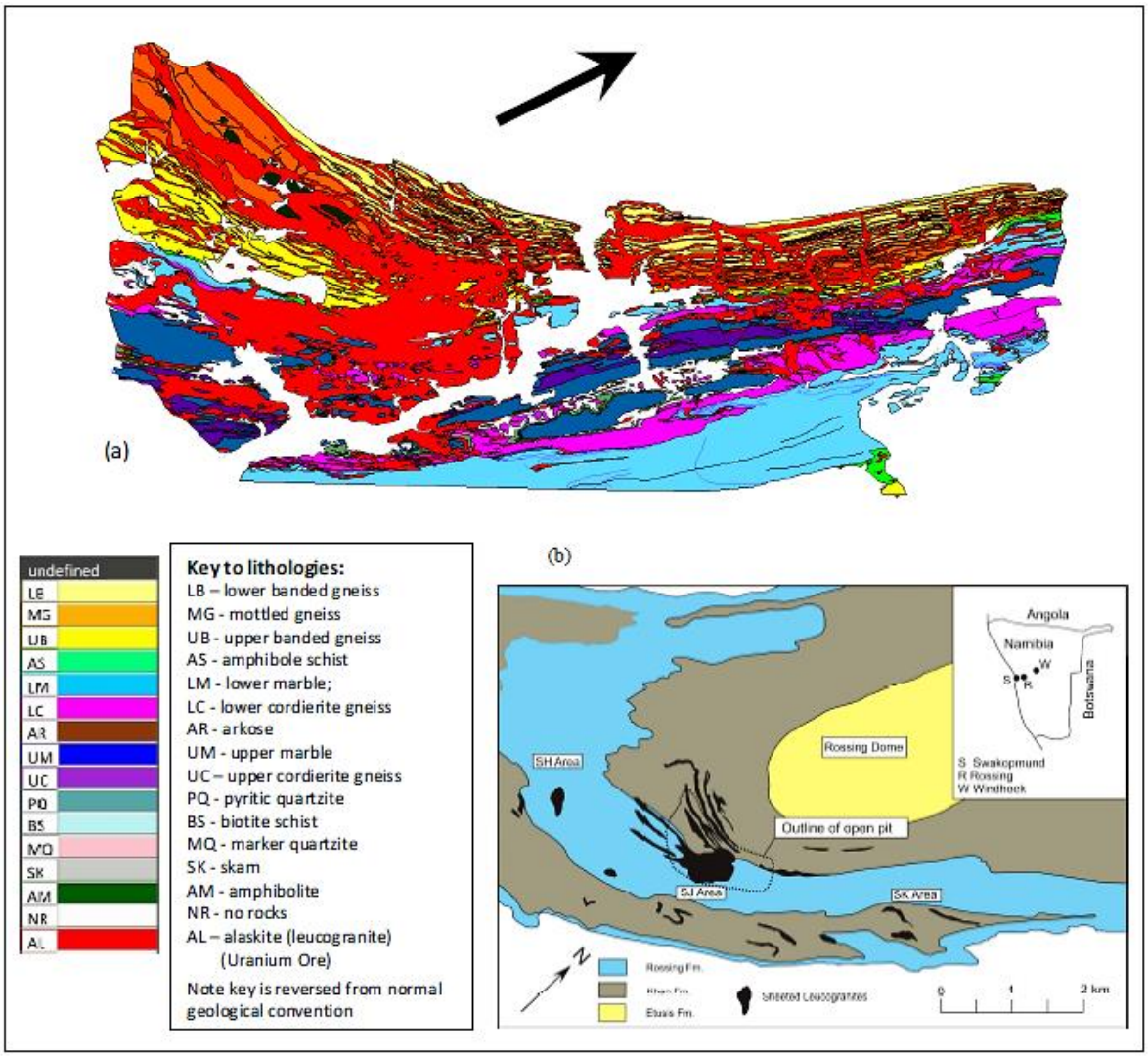


Figure 2.2: (A) Geological map of the main pit in the SJ area (B) Local geology of the Rössing Area showing the main anomalies (SH Area, SJ Area, SK Area) (Kinnaird and Nex, 2016).

2.3.1 Damara Supergroup

In the Rössing Area, psammites of the Etusis Formation form the core of the Rössing Dome (Oliver & Kinnaird, 1996; De Kock et al., 2000). The Etusis Formation comprises quartzites and meta-arkoses which have a pale pink colouration and exhibit cross-bedding on a small scale, with a highlighted concentration of the Fe-Ti oxide minerals (Abraham, 2009). The Etusis Formation forms the basal unit of the Damara Supergroup (Oliver and Kinnaird, 1996). The Khan Formation comprises locally banded migmatitic amphibole–clinopyroxene gneisses. Amphibole-biotite schist with minor, discontinuous deformed pebble horizons marks the formation of the uppermost package (Gray, 2015).

The Rössing Formation can be subdivided into several informal units including lower serpentine marble, meta-pelitic gneiss, and an upper siliceous and serpentine metacarbonate unit interbedded with granofelsic/schistose layers succeeded by meta-pelitic gneiss subunits (Gray, 2015). A typical Khan/Rössing contact succession occurs in the SJ pit, where the Khan and Rössing Formations are separated from each other by biotite amphibole schist that bisects the pit (Abraham, 2009).

2.3.2 Structural setting, granitic intrusion and metamorphism

The Rössing area is characterised by the Rössing Dome, which is surrounded by migmatised Etusis Formation meta-quartzites and metapelites (Oliver and Kinnaird, 1996; Basson and Greenway, 2004). There is a synclinorium with a sheared anti-formal core at the southern end of the dome, with an accompanying anti-formal structure to the immediate southwest (Basson and Greenway, 2004). There is also a sheared sequence of the Khan Formation gneiss along the south eastern flank of the dome. The Rössing SJ deposit occurs in a complex synclinorium, cored by the Rössing Formation marble with an axial plane that trends approximately east-west (E-W).

The original sedimentary layering (S_o) is preserved in the form of bedding within the Etusis and Rössing Formations (Abraham, 2009). S_1 and S_2 migmatitic bandings to the west of the Rössing are preserved within the Khan and Etusis Formations, whereas in the Rössing Formation, S_1 and S_2 occur as foliations. The D_3 deformation is characterised by ductile flow-folding in marbles of the Rössing Formation. D_3 is a polyphase folding (F_3), and it was followed by the development of a post-D_3 to D_4 Welwitschia Lineament, sinistral-slip strike zones and north-north-east (NNE) orientation of the Dome axis. The orientation differences between the folds and the dome were caused by the dome rotation during F_3 to F_4 (Basson and Greenway, 2004). The development of anticlinoria and synchronoria in the Rössing area was caused by the tectonic events (Abraham, 2009). Most of the uraniferous SLGs in the Rössing area are located near the major F_4 NNE trending lineament and local folds are parallel to this structure (Abraham, 2009).

The SLGs at the Rössing Uranium Mine are intruded parallel and sub-parallel to banding within the Khan and Rössing Formations mainly at the SK (anticline) and SJ (syncline) areas. Within the SH area, the leucogranites constitute a plug flanked by sheets on the margins of the Khan and Rössing Formations (Basson and Greenway, 2004).

The Rössing area experienced both contact and regional metamorphism. According to Abraham (2009), contact metamorphic effects are evident in metasedimentary rocks bordering the granite bodies, particularly where the granites have intruded the Rössing Formation marbles. The area also experienced high-temperature regional metamorphism. Regional metamorphism is evident by garnet, cordierite and unoriented sillimanite within Etusis psammites (Abraham, 2009).

2.3.3 Uranium mineralisation

The mineralised uranium-bearing SLGs in the Rössing area occur within the Rössing Formation, or between the Rössing Formation and the Khan Formation (Kinnaird and Nex, 2007; Abraham, 2009; Munro et al., 2011), and they are more prominent along the flanks of Rössing Dome (Kinnaird and Nex, 2007; Shanyengana et al., 2020). The mineralised SLGs are syn/post-D_3 alaskites, mainly D-type and E-type, which preferentially intruded into pyroxene-hornblende gneiss and biotite-amphibole schist units of the Khan Formation in the northern ore zone, and into biotite-amphibole schist/lower marble/lower biotite-cordierite gneiss of the Rössing Formation in the central ore zone (Basson and Greenway, 2004; Munro et al., 2011).

The main primary U-bearing minerals in the Rössing area are uraninite and betafite, which are included in quartz and feldspar, occur interstitially between these minerals or show preferential association with biotite and zircon (Berning et al., 1976; Cuney, 1979; Berning, 1986). Primary

uranium mineralisation in the area is e recognised by the unusually low concentrations of the rare earths (REE) and thorium (Rich et al., 1977). Secondary uranium mineralisation formed due to hydrothermal or surficial weathering, takes the form of uranophane, beta-uranophane, gummite, torbernite, carnotite, matahaweeite and thorogummite. According to Basson and Greenway (2004), a major part of the supergene mineralisation forms mineral coatings along joints, cracks, contact zones, fault planes, subsidiary shears, as well as penetrating mineral cleavages, and grain boundaries in quartz and feldspar, and between flakes of biotite. Fluid inclusions studies by Nex et al. (2002) indicate that the SJ area contains high content of H_2O, high H_2O/CO_2 ratios and high total fluids. The high content of the fluids in the area represents a localised fluid flux that resulted in uranium redistribution from uraninite into secondary U-bearing minerals such as beta-uranophane, which according to Nex et al. (2002) the sub-vertical orientation of the tabular granite sheets facilitated greater fluid movement.

2.4 Geology of the Goanikontes Area

The Goanikontes deposit is located 30 km east of the coastal town of Swakopmund, and about 40 km south of the Rössing Mine (Valois and Walgenwitz, 1979; Marlow, 1981; Mouillac et al. 1986; Nex, 1997).

2.4.1 Stratigraphy

The augen gneisses of the pre-Damaran Basement are unusually absent from the Goanikontes Dome (Mouillac et al., 1986). According to Nex and Kinnaird (1995) and Nex (1997), the augen gneisses are covered by the Damara sequence composed of Etusis, Khan, Rössing and Chuos Formation metasediments. These formations are in tectonic contact with the older pre-Damaran Basement, with only intermittent and attenuated portions of the Rössing Formation in the outcrop. The Etusis and Rössing Formations are attenuated and mostly absent on the surface north of the Swakop River. South of the river, the Damaran lithologies wrap around the southern lobe of the inlier, the Palmenhorst Dome, and the Damaran Formations are thicker than along the dome margin.

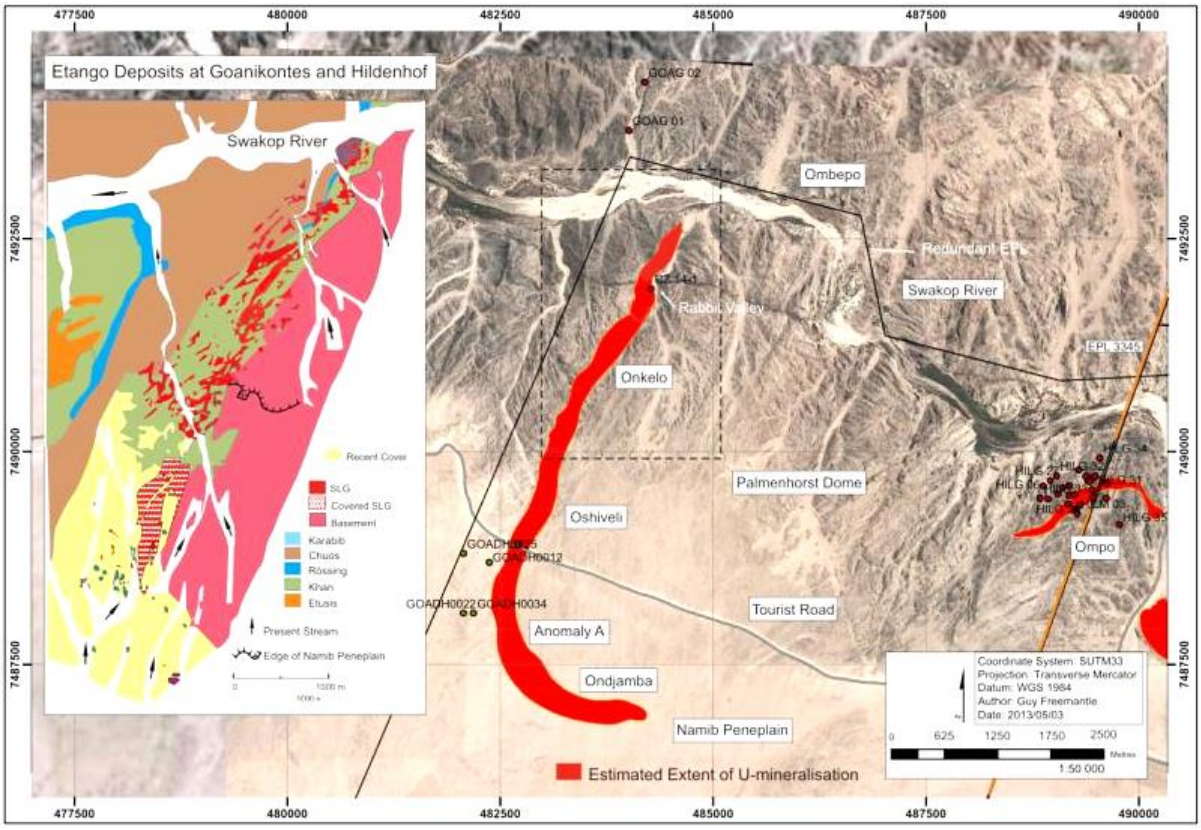


Figure 2.3: Geology of the Goanikonte Area west of Goanikontes Dome. The map shows the SLGs predominantly intruding the Khan and Chuos Formations (from Nex, 1997 modified after Mouillac et al., 1997 and Marlow, 1983 as cited by Freemantle (2015).

2.4.2 Magmatism

According to Nex (1997), granitoid intrusions are extremely well exposed in the area and they intrude both basement and Damaran metasediments. The granitoid intrusions are divided into early intrusions (the Red and Grey granites) and late intrusions, the SLGs, which are preferentially located within the high-strain zone. The SLGs are classified into six types (Table 1.1) based on field appearance, cross-cutting nature, mineralogy and petrology (Nex and Kinnaird, 1995; Nex et al., 2001a, b). SLGs are dived into those deformed by D_3 and D_4 (A-C types) and those which are post-D_3 (D-E types) (Nex et al., 2001a, b). The earliest type A are irregular in form, boudinaged and folded by D_3, and geochemically distinct with notably low HFSE; type B are white, weakly foliated, folded by D_3, garnetiferous and highly peraluminous; type C SLGs are tourmaline-bearing, occasionally boudinaged and exhibit the typical sheet-form within the cover rocks. Of the post-D_3 sheets, type D, which is restricted to the high strain zone is characterised by smoky quartz, high radioactivity and often by visible betafite or beta-uranophane; type E, the dominant type within the high strain zone contains prominent oxidation halos and type F is red in colour, coarsely pegmatitic and has the highest concentration of alkalis. The uranium-mineralised type D sheets have consistently higher fluid and CO_2 content than other sheeted leucogranites (Nex et al., 2001a, b).

2.4.3 Uranium mineralisation

Uranium ore deposits are situated to the west and southwest of the Goanikontes Dome. Elevated uranium grades predominate where the SLGs intrude the Khan, Rössing and Chuos Formations, with

a noticeable drop in in grade where the SLGs intrude the Etusis and Basement gneisses. According to Mouillac et al. (1986), high-grade uranium mineralisation occurs at the top of the Khan and in the Lower Chuos Formations. Primary uranium mineralisation of the SLGs and their emplacement occurred between 509 Ma and 508 Ma ago (Brique et al., 1960). Uranium mineralisation peaked in D-type SLG, with average (100 cps) and maximum (400 cps) scintillometer readings that are an order of magnitude higher than those of the other granites (Nex et al., 2001a).

2.5 Summary

2.5.1 southern Central Zone of the Damara Orogen

The geology of the southern Central Zone of Damara Orogen is composed of the AMC, the Damara Supergroup and the granitic intrusions. The AMC comprises the Tsawisis Formation, the Noab Formation and the Narubis Granitoids. The Damara Supergroup is divided into the Nosib Group which is composed of the Etusis and Khan Formations and the Swakop Group consisting of the Rössing, Chuos, Arandis, Ghaub, Karibib and Kuiseb Formations. The granitic intrusions of southern Central Damara Orogen comprise Red Granite gneiss, Salem Granite, Red Granite, Grey Granite and the SLGs.

The southern Central Zone of the Damara Orogen experienced four phases of deformation (D_1-D_4). These deformation events resulted in the formation of various structures such as folds during the D_1 and D_2, dome formation (D_3), and dome modification and development of the NNE Welwitschia Lineament (D_4).

Uranium mineralisation is stratigraphically and structurally controlled, and it occurs mainly in the vicinity of the Khan-Rössing Formations boundary and also within the Rössing-Arandis Formations which acted as REDOX zones. Uraninite is the major primary uranium-bearing mineral, while beta-uranophane occurs as a major secondary uranium-bearing mineral in the southern Central Damara Zone of the Damara Orogen.

2.5.2 Rössing Area

The geology of the Rössing area comprises the Damara Supergroup; the Etusis, Khan and Rössing Formations, and granitic intrusions such as the SLGs. The Rössing area also experienced four phases of deformation (D_1-D_4). D_1 and D_2 events are characterised by S_1 and S_2 migmatic banding and foliations within the Khan and Rössing Formations, D_3 by the ductile-flow folding in the Rössing Formation and D_4 by the development of Welwitschia Lineament. The mineralised D-type and E-type SLGs mainly occur close to the Khan-Rössing Formations boundary. Uraninite and betafite are the main primary U-bearing minerals, whereas uranophane is the dominant secondary uranium-bearing mineral in the Rössing Area.

2.5.3 Goanikontes Area

The geology of Goanikontes area is composed of pre-Damaran Basement augen gneisses, overlain by Damaran Supergroup metasediments (Etusis, Khan, Rössing and Chuos Formations). In the area, there are also granitic intrusions divided into the early intrusions (Red and Grey granites) and late intrusions (SLGs). High-grade uranium mineralisation occurs where the D-type SLGs intruded the Khan, Rössing and Chuos Formations.

CHAPTER THREE

METHODOLOGY

3.1 Introduction

Previously collected sample materials (Table 3.1) were made available for this study by my supervisor since it was not possible to visit the study area due to Covid-pandemic travel restrictions. Four techniques were employed to analyse the rock samples: visual hand sample descriptions, thin section examination using a petrographic microscope, Micro (μ)-XRF analysis and automated mineralogical scanning studies using a TESCAN Integrated Mineral Analyser (TIMA).

Hand specimen and thin section analyses were done in the MSc. Economic Geology Laboratory, School of Geosciences, University of the Witwatersrand. Thin section preparation was done in the Geoscience General Laboratory, whereas thin section imaging was done in WIMLAB (Wits Imaging Laboratory). Elemental mapping for major and minor elements of the whole TS2 rock sample using μ-XRF was done at the Mintek Mineralogy Laboratory. TIMA studies were done at the School of Geosciences, the University of Witwatersrand, in the Wits Automated Mineralogy Laboratory (WAMLAB).

Table 3.1: Description of the rock samples

Sample #	Year of collection	Location	Sample type	Remarks
SJ-06-02	February 2006	Rössing SJ Pit	E-type SLG	Herein regarded as TS2
7-1	January 2007	Rabbit Valley (Goanikontes)	D-type SLG	Herein regarded as TS1

3.2 Hand specimen analysis

Rock samples were examined for their mineral composition, texture, colour, crystal habit, contact relationships between crystals and structures. The observations were made under two conditions; before and after wetting the samples. Soaking the samples helped to enhance the visualisation of some features such as mineral colour and texture, which were not so clear when the sample was dry.

3.3 Thin section analysis

In total, 19 thin sections were prepared from both rock samples: 8 thin sections from TS1 (Figure 3.1; Figure 3.2) and 11 thin sections from TS2 (Figure 3.3; Figure 3.4; Table 3.2). The selection of thin sections for preparation was based on textural variation, mineral composition and colour. All prepared thin sections were observed under the petrographic microscope, with much attention to four thin sections of TS1 (TS1-2, TS1-3, TS1-5, TS1-7) and five thin sections of TS2 (TS2-1, TS2-4, TS2-5, TS2-6, TS2-9). Thin sections analysed in detail represented other thin sections with similar petrographic features from various rock samples sections they were prepared from (Table 3.2). The

Olympus BX41 Petrographic Microscope was used to examine thin sections for their textural and mineralogical features. Mineral grain size measurement using full thin section images and micro-XRF elemental map was done with the help of GIMP software.

Table 3.2: Numbering of the thin sections prepared from both the TS1 and TS2 rock samples

Rock sample	Rock sample section	Thin section number
TS1	TS1 section 2	TS1-1
	TS1 section 3	TS1-2
	TS1 section 4	TS1-3, TS1-5, TS1-7
	TS1 section 5	TS1-6, TS1-7
TS2	TS2 section 1	TS2-1
	TS2 section 2	TS2-4, TS2-3, TS2-7, TS2-10
	TS2 section 3	TS2-6, TS2-12
	TS2 section 4	TS2-5, TS2-11
	TS2 section 5	TS2-3, TS2-9

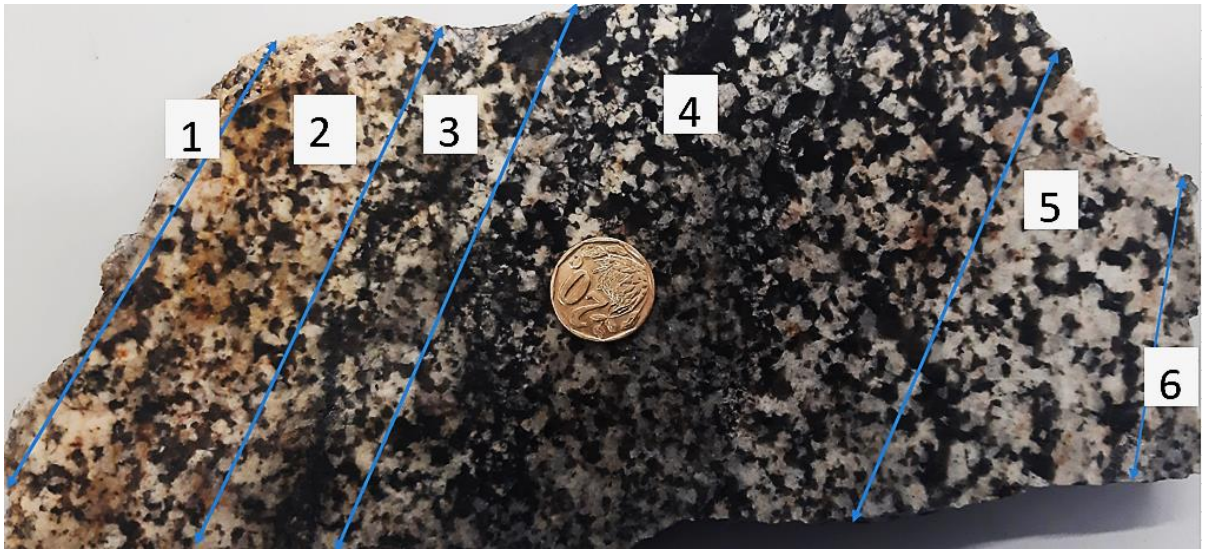


Figure 3.1: Photograph of sample TS1 shows sections division of D-type SLG based on textural variations: TS1 sections 1, 3 and 6 (medium-grained), TS1 sections 2 and 5 (pegmatitic), TS1 section 4 (coarse).



Figure 3.2: Hand specimen of rock sample TS1 (D-type SLG) shows the demarcation for thin section preparation.

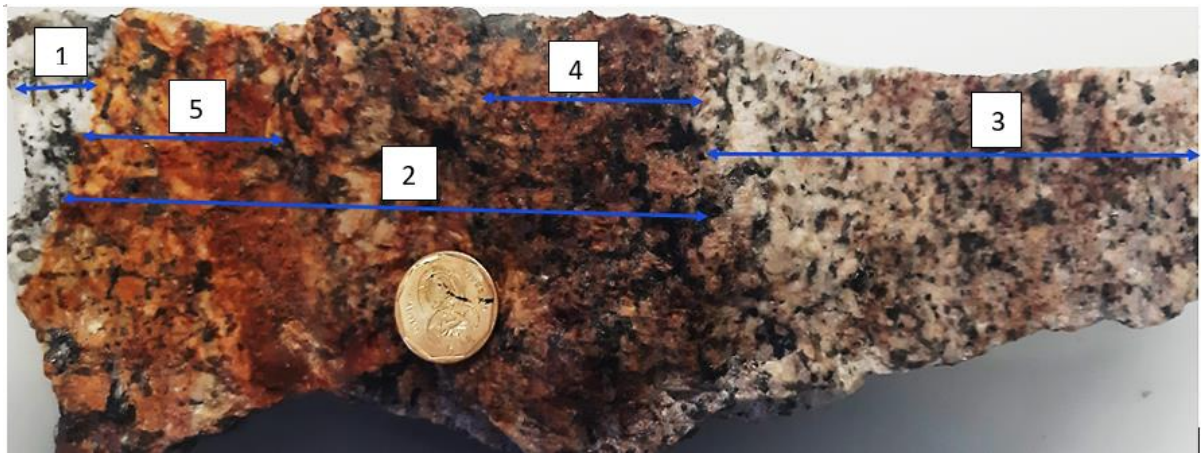


Figure 3.3: Photograph of sample TS2 shows section divisions of E-type SLG sample: 1- TS2 section 1 (D-type SLG D-type), 2- TS2 section 2 (oxidation halo section), 3- TS2-section 3 (E-type), 4- TS2 section 4 and 5- TS2 section 5.

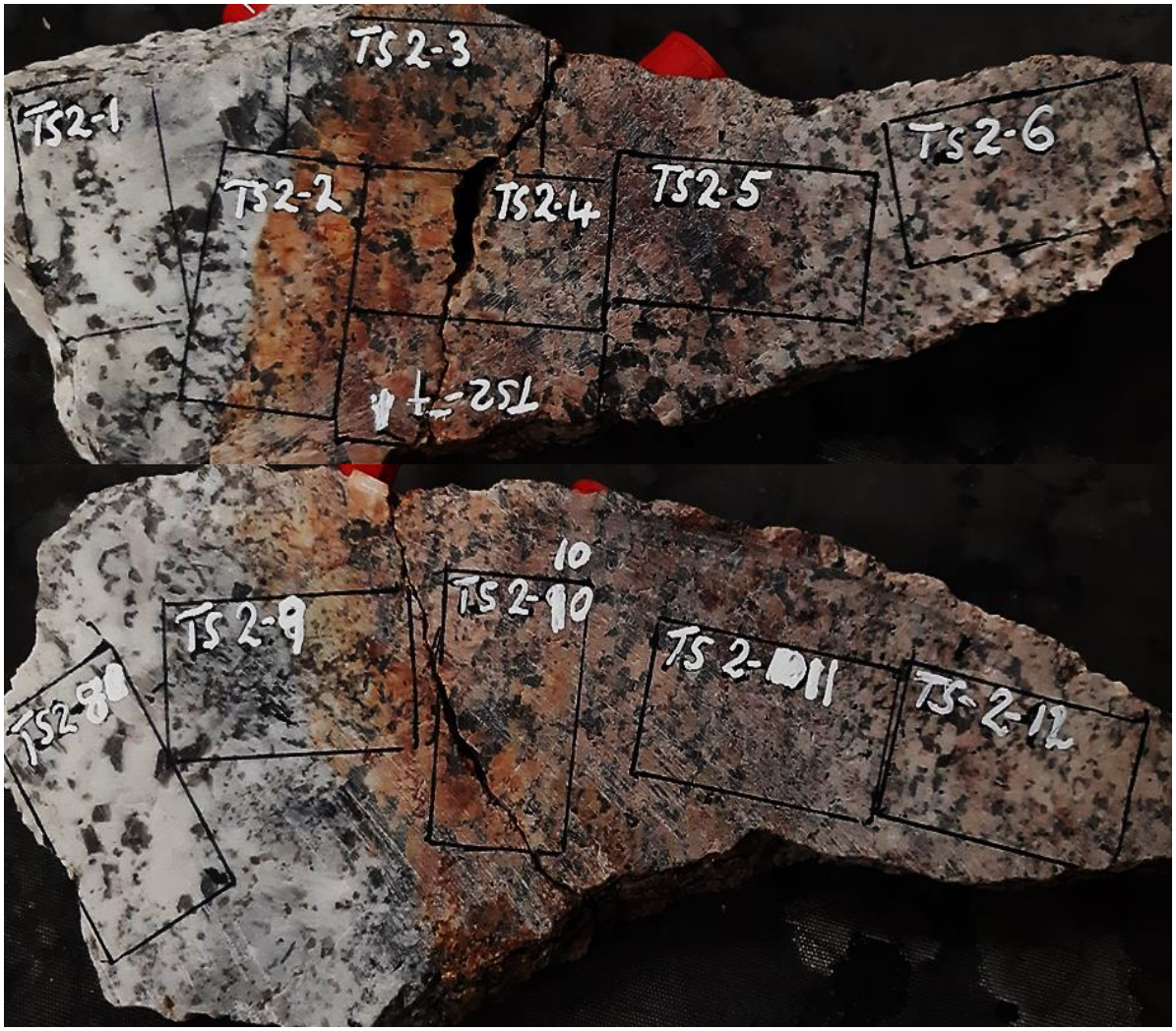


Figure 3.4: Hand sample of rock sample TS2 (E-type SLG) shows the demarcation for thin section preparation.

3.4 Micro-XRF analysis

The Bruker µ-XRF M4 Tornado is an automated, benchtop mineral analyser using the same principles as XRF (Warwick, 2017). It has a spatial resolution many orders of magnitude smaller than that of a conventional XRF. The µ-XRF uses X-ray optics to restrict the excitation beam size to a small spot to map small features on the sample surface. High restriction of a beam of light blocks much of the X-ray flux which has an adverse effect on the sensitivity of trace elemental analysis. This technique brings together fast, high-resolution elemental distribution analysis using the M4 Tornado and powerful mineral identification and classification using the AMICS (Advanced Mineral Identification and Classification Software) (Warwick, 2017). The analysis of the rock samples down to the micrometre scale helps to identify mineral phases by X-rays without the cost of SEM and also minimal or no sample preparation is needed.

The elemental maps for major and minor elements occurring in the oxidation halo sample (TS2) were produced using Bruker µ-XRF to understand the mineralogical composition and distribution of the mineral phases. The elemental maps were also used to determine the textural variations across the whole TS2 sample. Table 3.3 below summarises the settings of the Bruker µ-XRF used to analyse the TS2 rock sample.

Table 3.3: A summary of µ-XRF settings used during the elemental mapping of the TS2 rock sample at the Mintek Mineralogy Laboratory.

Mapping parameters	Description	Acquisition parameters	Description	Tube parameters	Description
Width	183 mm (1830 pixel)	Pixel time	10 ms/pixel	High voltage	50 kV
Height	85 mm (850 pixel)			Anode current	599 µA
Pixel size	100 µm			Filter	Empty
Total pixel number	1555500 pixels			Optic	Lens
				Spot Size	20 µm
				Chamber at	Air 2 mbar
				Anode current	Rh

3.5 TIMA (Tescan Integrated Mineralogical Analysis)

TIMA is a high-resolution Field Emission Scanning Electron Microscope (FESEM) equipped with four fully integrated silicon drift EDS: Energy Dispersive Spectroscopy (EDS) detectors designed for automated mineralogy (Hrstka et al., 2018). It uses fast BSE (Back-scattered Electrons) and EDS detectors simultaneously to reliably identify and measure minerals and create mineral images (Hrstka et al., 2018). Thin section samples prepared for petrographic analysis were also used for TIMA analysis. Sections of specific areas within the samples for TIMA analysis were selected based on the petrographic analysis, and the selected sections/areas represented all the four divisions of the oxidation halo (Figures 1.2 and 4.4).

TIMA studies included mineral phase identification, BSE and elemental maps were produced to determine mineral concentrations, distribution and textural properties of the oxidation halo and their host granitic material. TIMA studies were also used to assess mineral composition and alteration, which could not be fully done using petrographic analysis. Phase maps were used primarily for understanding the distribution and proportions of minerals, the texture, structure and mineral phase association. Mineral texture and structure features were investigated through mineral segmentation analysis.

BSE maps were used to identify mineral phase types in the rock samples. Dense minerals contain elements with high atomic numbers such as uranium which are bright, whereas, low-density minerals contain elements with low atomic numbers such as feldspars and quartz and are dark in phase maps.

Phase and elemental maps of minerals were quantified by energy-dispersive X-ray spectroscopy (EDS) using the VEGA3 SEM instrument and the VEGA3 X64 TESCAN TIMA 1.7.0. The beam conditions for VEGA3 X64 TESCAN SEM during quantitative analyses were 25 kV accelerating voltage, 43 µA emission current, a working distance of 21.33 mm, a specimen beam current of 17.68nA, and the spot size of 590.00 nm with an absorption current of <1pA. The scanning mode was set at resolution mode, the heating at 47%, the filament live time was at 431 hours, and the gun pressure was at 1.6×10^{-3} Pa while the column pressure was at 5.5×10^{-3} Pa. The system is also designed to perform high-resolution mapping (liberation and modal analysis) concurrently with imaging with a

resolution of up to 2 µm per pixel with a working distance of 15 mm. Then Table 3.3 below summarises the four techniques used to analyse the rock samples in this study.

3.6 Study limitations

There were four major limitations that affected this study. The first challenge was the sample size as only two rock samples were made available for the analysis. If more samples were analysed, comparable results could have been produced to improve the interpretation of the research results. The second challenge was the lack of chemical analysis. Much emphasis was on the distribution of U-bearing minerals between the halos, the different texture types, and the unaltered/altered portions of the rock samples. TIMA and µ-XRF do not appear to have quantified uranium distribution, with just one section (TS2 section 4) having identifiable primary uranium-bearing mineral (uraninite) using TIMA. The portions of the sample that the thin sections were cut from ideally could have been analysed by conventional handheld XRF as a check against the perceived uranium distribution by thin section petrography, µ-XRF and TIMA although this was not possible due to COVID restrictions in the laboratories. Another study limitation was the collection of rock samples from different sites; the E-type SLG (TS2) was collected from the Rössing SJ Pit and the D-type SLG (TS1) was collected from the Rabbit Valley at Goanikontes instead of both coming from the Rössing SJ Pit. Various sites may have different local geological conditions, resulting in different rock compositions and textures for the same rock types. The last challenge is the low detection limit of the µ-XRF and TIMA techniques used. These techniques failed to resolve and classify most of the accessory uranium-bearing mineral phases the mineralised SLGs are known for.

3.7 Summary

Four techniques were used to analyse the rock sample as summarised in Table 3.4.

Table 3.4: Summary of the techniques used in analysing the rock samples

Technique	Instruments	Laboratory	Samples	Purpose of the technique
Hand specimen observation	Measuring ruler and pencil (grain size measurement)	MSc Economic Geology (Wits)	TS1 (TS1 sections 1-5) TS2 (TS2 sections 1-5)	Determining mineral composition, texture, rock colour and structures
Thin section analysis	Olympus BX41 Petrographic Microscope GIMP software (grain size measurement)	Geoscience General Laboratory (Wits) MSc, Economic Geology, WIMLAB	TS1 (TS1-1, TS1-2, TS1-3, TS1-3, TS1-5, TS1-7) TS2 (TS2-1, TS2-4, TS2-5, TS2-6, TS2-9)	To determine textural and mineralogical features and alteration styles
Elemental mapping	Bruker µ-XRF, GIMP software	Mintek Mineralogy	Whole TS2 rock sample	Mapping major and minor elements distribution Determining textural variations
TIMA analysis	VEGA3 X64 SEM, VEGA3 X64 TESCAN TIMA 1.7.0, GIMP software	WAMLAB	Same as those under thin section analysis	Determining mineral concentration and distribution, textural properties and alterations

CHAPTER FOUR

RESULTS

4.1 Introduction

The aims of this research project are to document and interpret petrological features of the mineralised oxidation halos and their host rocks. Therefore, this chapter presents the results obtained through the various analytical techniques used in analysing the rock samples, including hand specimen observations, thin section petrography, Micro (µ)-XRF elemental mapping and TIMA studies.

4.2 Hand specimen observations

The hand-specimen observations were made to document the textural features and mineralogy of various rock sample sections for both TS1 and TS2 rock samples.

4.2.1 Textural features and mineralogy

Freemantle (2015) classified the SLGs into a fine-grained texture (<2 mm), medium-grained texture (2-5 mm), coarse-grained texture (5-10 mm) and pegmatitic texture (>10 mm) based on mineral grain sizes range. Appendix 4 presents the mineral grain size measurements measured through hand specimen observations. The mean average grain size, the modal grain sizes and the grain size range (Appendix 5) were then determined using Appendix 4 results. Figure 4.1 and Figure 4.2 show how average mineral grain sizes are distributed in the sections of both rock samples.

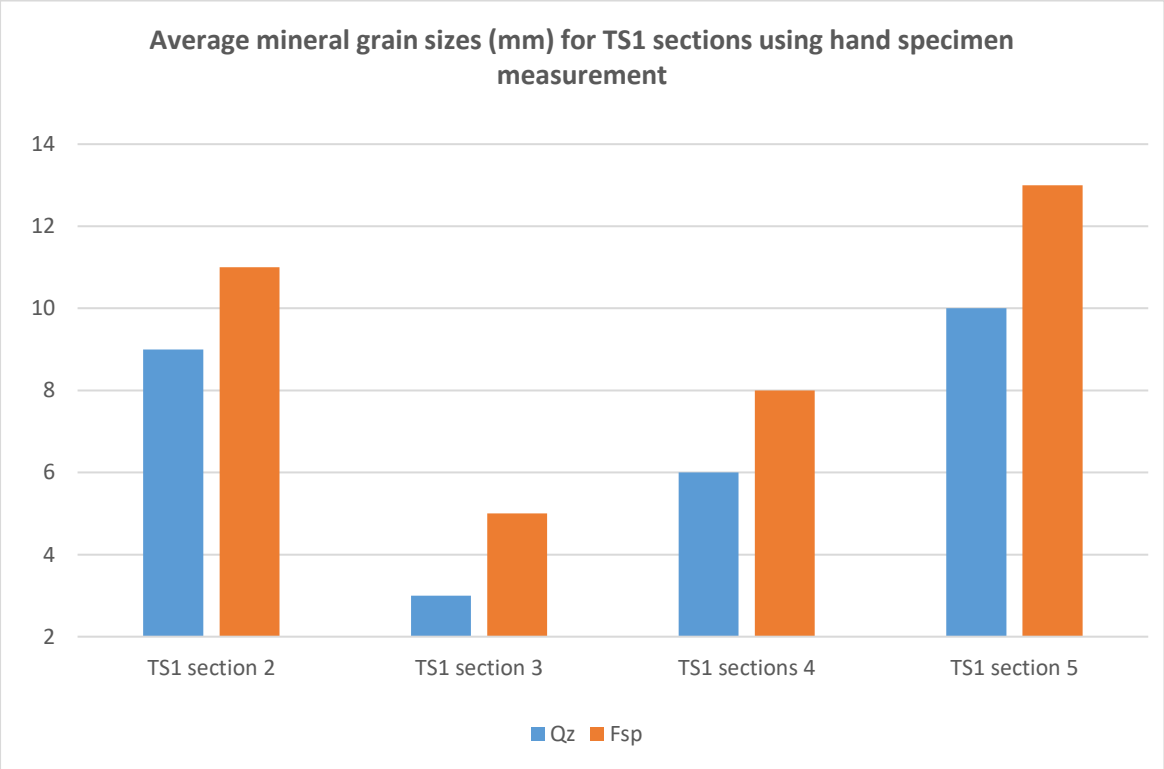


Figure 4.1: Graphical presentation of the mean grain sizes for TS1 measured using hand specimen observations. Note: Measurements for TS1 section 3 also represent the TS1 sections 1 and 6. Note: Qz- quartz, Fsp- feldspar.

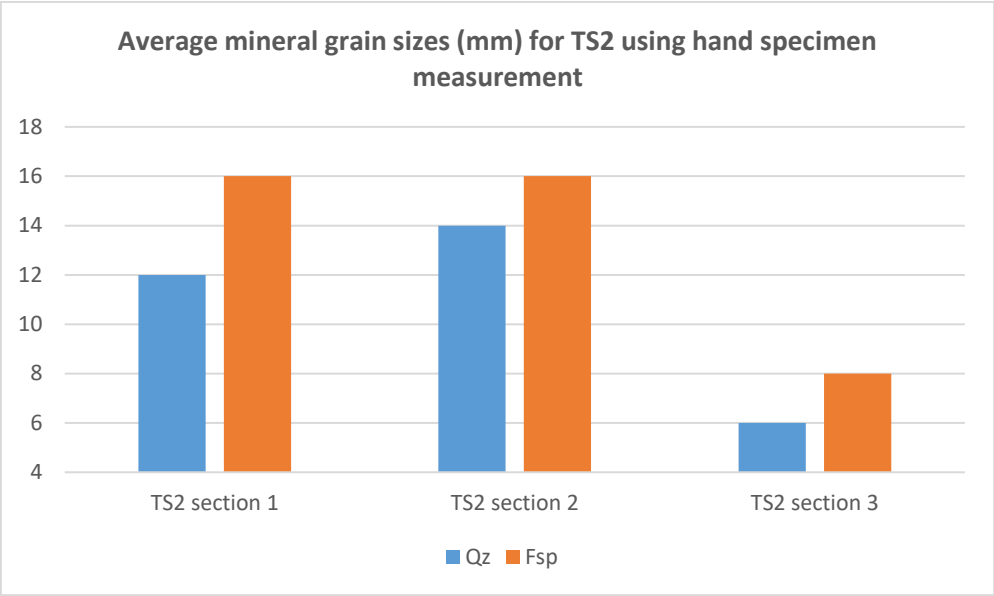


Figure 4.2: A graph showing average mineral grain sizes distribution for TS2 sections. Note: Qz-quartz, Fsp-feldspar.

The results show that in both rock samples, mineral grain sizes range from medium-grained to pegmatitic. In the TS1 rock sample, TS1 sections 2 and 5 are dominated by pegmatitic mineral grain sizes, while TS1 sections 3 and 4 have medium- and coarse-grained as their dominant mineral grain sizes, respectively (Figure 4.1). For the TS2 rock sample, the D-type (TS2 section 1) and the oxidation core section (TS2 section 2), are dominated by pegmatitic mineral grains, while the E-type (TS2 section 3) is dominated by coarse-grained minerals.

TS1 (D-type SLG)

The subsequent sub-sections describe the mineral modal composition, grain size measurements and structures observed across the sections of the TS1. The mineral grain sizes were counted and measured without any bias.

TS1 sections 1, 3 and 6 (medium-grained)



Figure 4.3: Photograph of sample TS1 showing the division of D-type SLG based on textural variations; TS1 sections 1, 3 and 6, TS1 sections 2 and 5, TS1 section 4

The TS1 sections 1, 3 and 6 (Figure 4.3) show similar rock texture (dominated by medium-grained textured minerals), as well as the distribution of minerals. Table 4.1 below shows the modal proportions for biotite, quartz and feldspar for TS1 sections.

Table 4.1: Modal proportions for quartz and feldspar determined using hand specimen observations

Rock sample section	Quartz modal proportion (%)	Feldspar (plagioclase) modal proportion (%)	Biotite modal proportion (%)
TS1 sections 1, 3 and 6	48	52	<1
TS1 section 2	40	60	<1
TS1 section 4	50	47	3
TS1 section 5	43	56	1

The modal proportion results (Figure 4.4; Table 4.1) show that the TS1 sections 1, 3 and 6 are dominated by quartz and feldspar. The average mineral grain size for quartz is 3 mm, and it ranges from 1-5 mm. Quartz colour varies from colourless to a dominantly dark colour (smoky quartz). Feldspar crystals have an average grain size of 5 mm, which range from 2-8 mm (Appendix 5). In most cases, small quartz grains occur as inclusions in the feldspar. Quartz and feldspar also show an intergrowth relationship. The modal grain sizes range for both quartz and feldspar is 2-5 mm (Appendix 5).

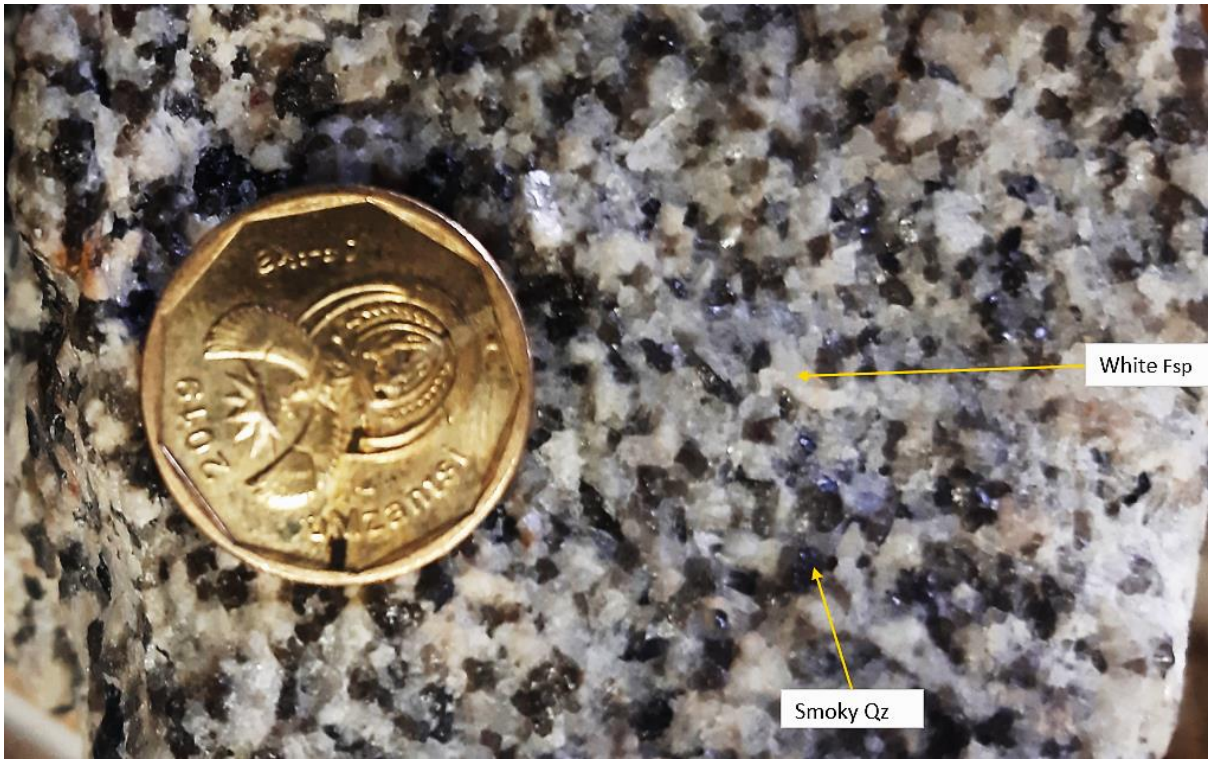


Figure 4.4: Section 6 of TS1 shows the association and distribution of the quartz and feldspar.

TS1 section 2 (coarse-grained to pegmatitic)

TS1 section 2 is also dominated by quartz and feldspar (Table 4.1). Quartz has an average grain size of 8.6 mm, and the grain sizes range from 1-18 mm in size (Appendix 5). Quartz crystals exhibit an anhedral shape, and they also form quartz chains and clusters in some areas of the section (Figure 4.3). Feldspar has an average grain size of 11.1 mm, and it ranges from 2-23 mm (Appendix 5). The high abundance of plagioclase (white) feldspar makes TS1 section 2 looks more light than other sections. Feldspar shows both euhedral and anhedral shapes, while quartz exhibits mainly anhedral forms. In this section, there are also clear contact and intergrowth relationship between quartz and plagioclase crystals. The modal grain sizes ranges for both quartz and feldspar are 5-10 mm and 10-23 mm, respectively (Appendix 5).

TS1 section 4 (coarse-grained)

In TS1 section 4, the mineral modal proportion results (Table 4.1) indicate that the section is dominated by quartz and feldspar. The section has also a significant amount of biotite making up approximately 3% of the section. Quartz has an average grain size of 6 mm, and it ranges from 2-10 mm (Appendix 5). The quartz crystals exhibit an anhedral shape, and they also form quartz chains and some clusters (Figure 4.3). Feldspar has an average grain size of ~8 mm, and the grain sizes range from 4-18 mm. The most dominant mineral grain sizes for both quartz and feldspar range between 5-10 mm, though feldspar has a significant amount of >10 mm grain sizes (Appendix 5). TS1 section 4 also contains dark- and light-coloured mineral layers. Biotite and smoky quartz compose the dark layer, while the light layer is dominated by feldspar (Figure 4.5).



Figure 4.5: TS1 section 4 shows some banding- smoky quartz and biotite forming dark layers.

TS1 section 5 (pegmatitic)

In TS1 section 5, Table 4.1 shows that quartz and feldspar also dominate this section. Quartz crystals average about 10 mm, with a range of 4-18 mm (Appendix 5). In this section, quartz crystals also exhibit an anhedral form, and they also form quartz clusters. Feldspar has an average grain size of 12.6 mm, and it ranges from 5-18 mm. Both quartz and feldspar have mode grain sizes ranging from 10-18 mm (Appendix 5). Feldspar crystals exhibit both euhedral and anhedral shapes. The section also has approximately 1% biotite.

TS2 (E-type SLG)

Figure 4.6 shows the demarcation of the TS2 (E-type) rock sample sections: TS2 sections 1 and 2 (pegmatitic), TS2 section 3 (coarse-grained) and TS2 sections 4 and 5 (medium-grained).

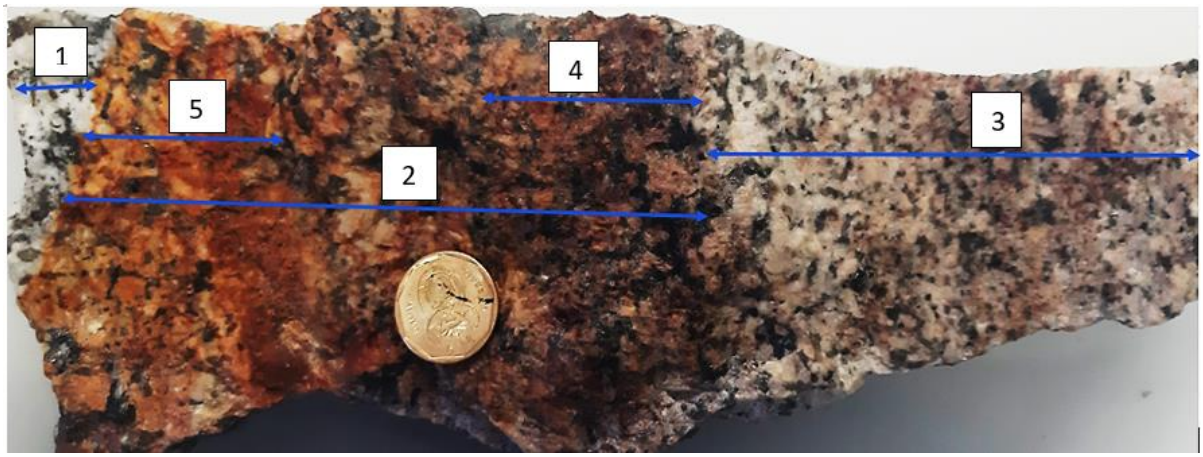


Figure 4.6: Photograph of sample TS2 showing section divisions of E-type SLG sample; 1- SLG D-type section, 2- Oxidation halo section, 3- SLG E-type, 4- transition zone from oxidation halo section to E-type and 5- transition zone from D-type section to oxidation halo zone.

TS2 section 1 (D-type SLG) (pegmatitic)

The D-type SLG section contains approximately 38% quartz, whose average grain size is around 12 mm, and it ranges from 4-25 mm (Appendix 5). The appearance of quartz changes from colourless to dark (smoky quartz). Large quartz crystals adjoining each other form chain-like and cluster structures. In terms of grain size, quartz crystals vary from fine to pegmatitic. In the D-type-oxidation halo transition zone, quartz crystals occur as tiny granular and elongated crystals. TS2 section 1 (Figure 4.7) also contains about 2% biotite, whose content increases towards the corona and occurs as laths. Mineral grain size for biotite ranges from <1 mm to 3 mm, with 1 mm as the average grain size. Feldspar in the section forms about 50% of the total section mineral composition, and it has an average grain size of ~15.5 mm with a range of 1-35 mm (Appendix 5). Feldspar exhibits both euhedral and anhedral crystal forms. There are isolated inclusions of reddish and yellowish minerals within the feldspar, probably haematite and U-bearing minerals, respectively.

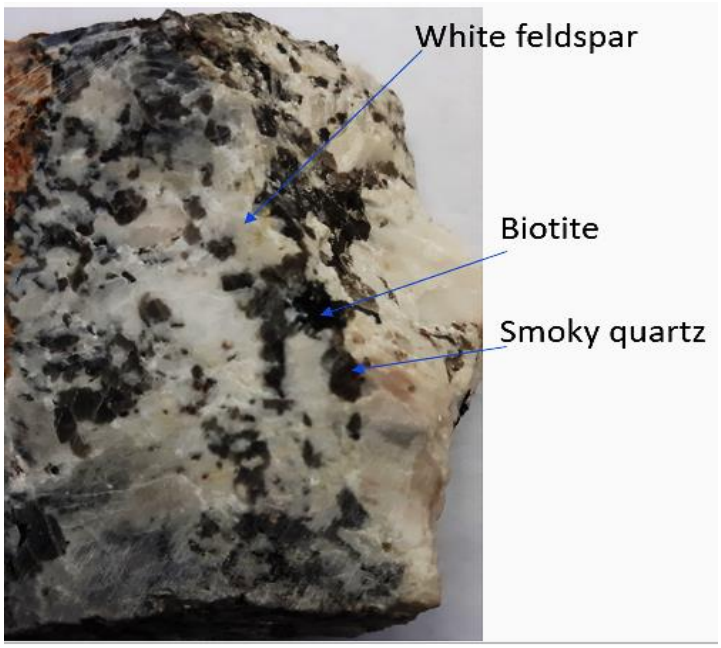


Figure 4.7: TS2 section 1 mineral distribution and association and pegmatitic texture.

TS2 section 2 (oxidation halo core zone) (pegmatitic)

The oxidation halo section contains about 43% quartz. Quartz grain sizes average about 14 mm, and the mineral grain sizes range from 3-26 mm in size (Appendix 5). Quartz crystals exhibit both euhedral and anhedral shapes; the euhedral quartz crystals are observed in the oxidation halo core zone and the TS2 section 5 (Figure 4.8). Smoky quartz crystals are darker in the oxidation halo boundary zones, where they show an intergrowth relationship with biotite. Biotite composes about 3% of the TS2 section total mineral composition. Large quartz crystals also form the quartz chain and cluster structures (Figure 4.8).



Figure 4.8: Cross-section of oxidation halo section showing the core zone being dominated by pink feldspar while the boundary zone is dominated by smoky quartz.

The oxidation halo section contains about 54% feldspar, whose grain sizes range from 5-25 mm, and has an average grain size of about 16.1 mm. The primary colour of feldspar is pink, but it changes from yellow-pink to red-pink to pink due to differences in iron oxide (haematite) staining (Figure 4.9). In the oxidation halo section, feldspar has inclusions of yellow and red coloured minerals, possibly uranium- and iron-bearing minerals. The oxidation halo is zoned into the core, intermediate and outer zones. The core zone is mainly pink as there is less red staining of feldspar. In the intermediate zone, the central boundary zone between the oxidation halo and E-type sections has a deep red colouration and a high content of smoky quartz associated with abundant biotite. Yellow staining of K-feldspar dominates the outer core, mainly in the boundary zone between oxidation halos and D-type material (Figure 4.9).

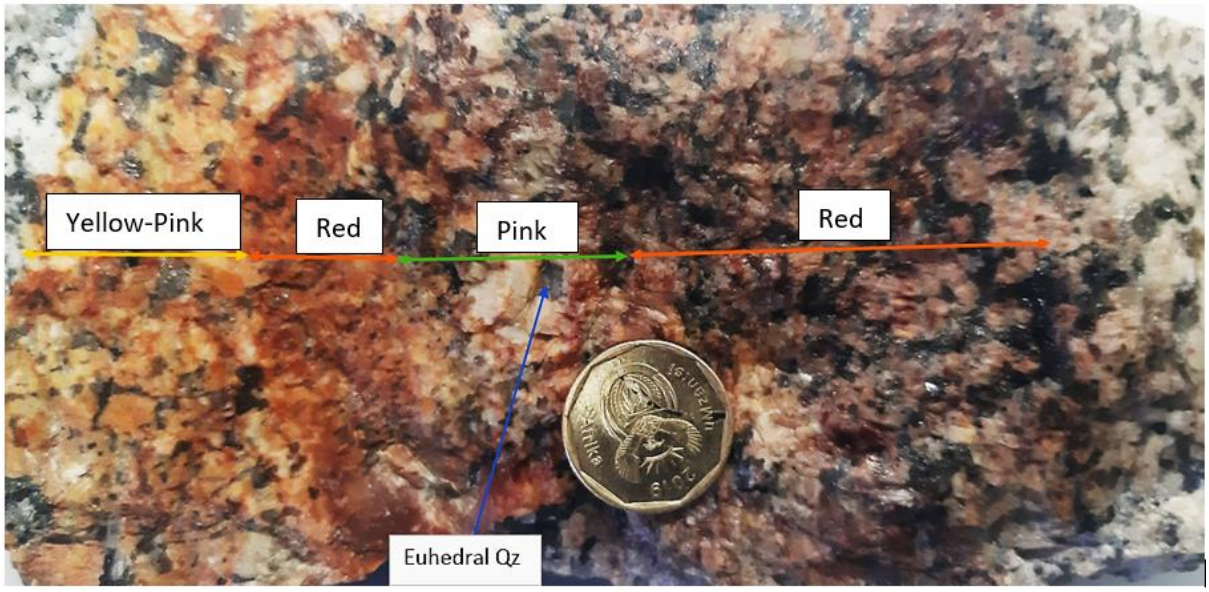


Figure 4.9: Hand sample of TS2 showing the oxidation halo section showing colour variation from D-type to the right to the E-type to the left. Note: The presence of high abundances of biotite and smoky quartz in the transitional zone between the oxidation halo core and E-type section make this section to have deep red colouration compared to that observed between oxidation halo core zone and D-type section.

TS2 section 3 (E-type SLG) (coarse-grained)

The E-type SLG section contains approximately 44% quartz, with a 6 mm average grain size and a range of 1-14 mm (Appendix 5). Quartz appearance in the TS2 section also changes from colourless to dark (smoky quartz). When quartz occurs as small granular crystals, they tend to be included in feldspar (Figure 4.10). The E-type section also has feldspar forming about 51% of the total section mineral composition. Feldspar mineral phases also have a few inclusions of red-coloured minerals whose concentration increases towards the oxidation halo. The average grain size for feldspar is about 8 mm, and the mineral grain sizes range from 1-18 mm (Appendix 5). The primary crystal forms for feldspar in this section are both euhedral and anhedral. TS2 section 3 also has ~2% biotite, which mainly occurs in association with the smoky quartz. This section primarily appears pink (Figure 4.10) since it is less stained with iron oxides minerals such as haematite.

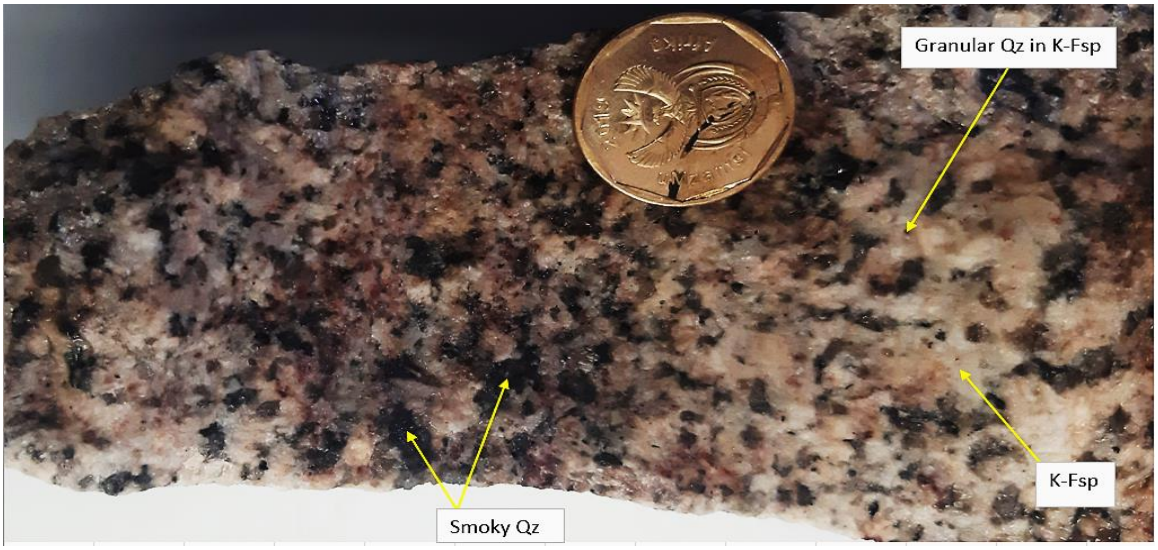


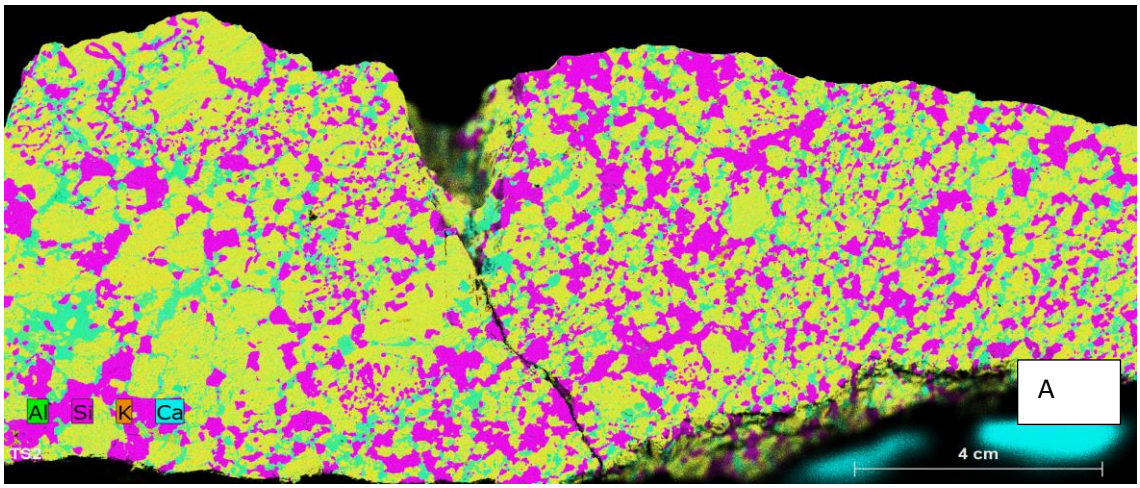
Figure 4.10: E-type section of sample TS2 showing mineral association of smoky quartz and pink feldspar.

4.3 Micro-XRF results

The TS2 rock sample analysis for the major elements using the µ-XRF helped to determine the major rock-forming mineral composition and distribution patterns, as well as identifying certain U-bearing minerals for the entire rock sample. Through the µ-XRF elemental maps, the exact textural change for the whole TS2 rock sample was determined. The elemental maps depicted the exact boundary zones of major elements representing various rock-forming minerals (Figures 4.11) resulting in quantifiable mineral grain size measurements.

4.3.1 Textural variation for TS2 using µ-XRF elemental maps

Mineral grain sizes using Al, Ca, K and Si elemental maps for all TS2 sections (Figure 4.9A) were measured using GIMP 2.10.22 software.



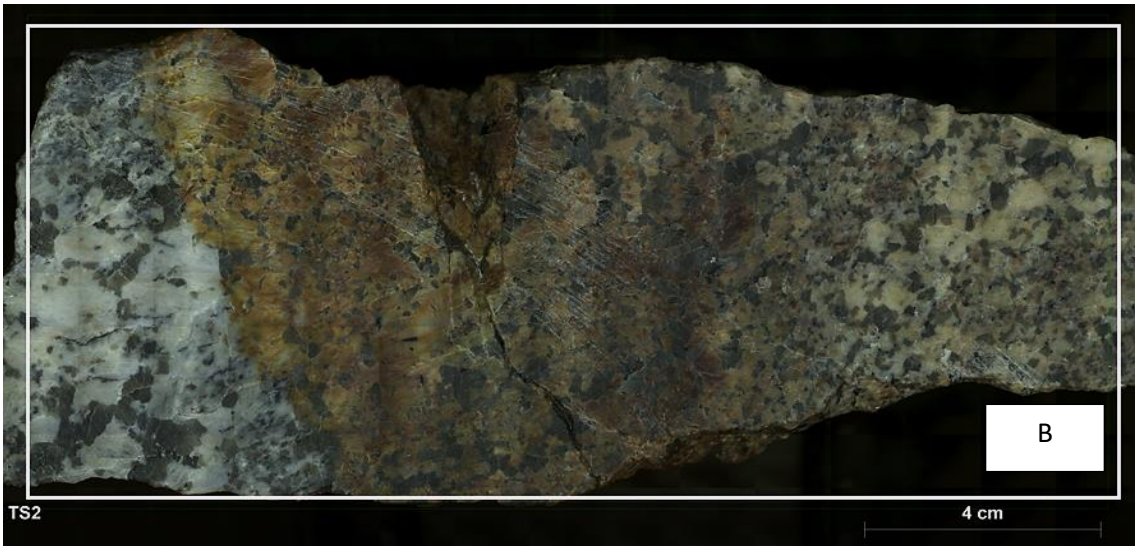


Figure 4.11: (A) TS2 whole rock sample Al, Ca, K and Si µ-XRF element map and (B) Mosaic showing mapped area in the white rectangle. Note: Al- Aluminium (green), Ca- Calcium (blue), K- Potassium (yellow), Si- Silicon (purple)

Appendices 6 and 7 represent mineral grain size measurements and descriptive statistic results for TS2 rock sample sections. The results show that TS2 sections 1 and 2 all are dominated by mineral grains of >10 mm, while TS2 section 3 has 5-10 mm mineral grain sizes as a modal range, whereas TS2 sections 4 and 5 are dominated by 2-5 mm mineral grain sizes. Figure 4.12 and Appendix 7 show the distribution of the mean mineral grain sizes across the TS2 rock sample. Figure 4.12 shows that TS2 sections 1 and 2 are dominated by pegmatitic texture, TS2 section 3 by coarse-grained minerals and TS2 sections 4 and 5 by medium-grained textured minerals. Within the TS2-section 2, most coarse grain sizes of feldspar (represented by K in Figure 4.11A) occur at the oxidised interface unlike in the other areas of the same section.

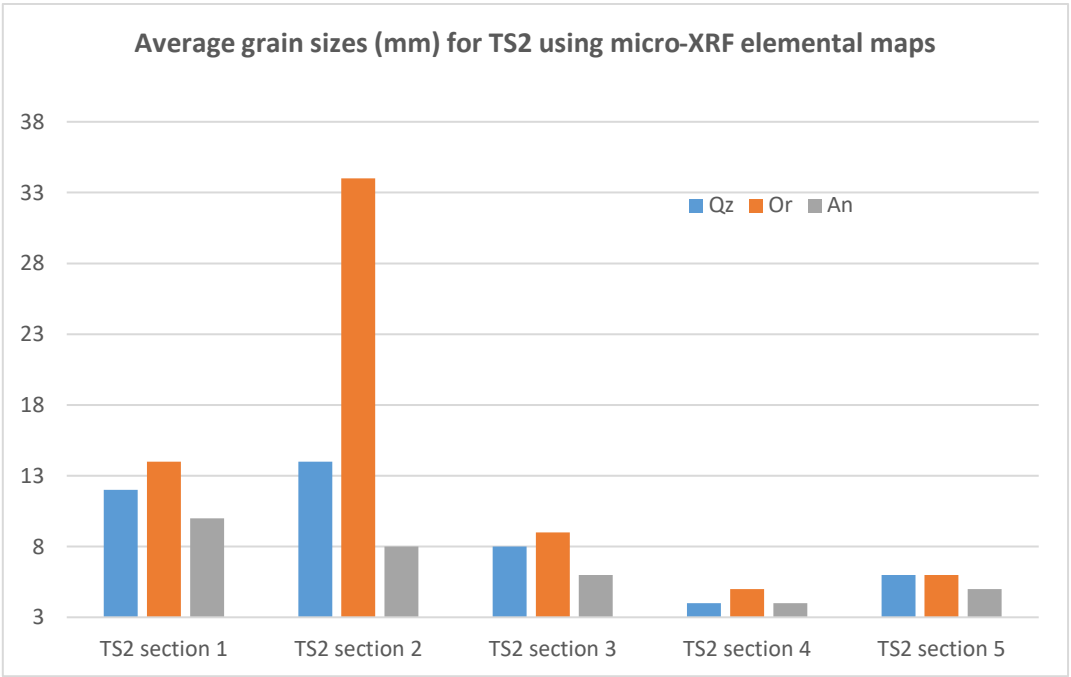


Figure 4.12: A graph showing the distribution of the mean grain sizes across the TS2 rock sample determined using µ-XRF elemental maps presented in Appendices 6 and 7. Note: Qz- quartz, Or- orthoclase, An- anorthite

4.3.2 Mineralogy of TS2 based on µ-XRF elemental maps

The rock-forming minerals identified through µ-XRF elemental maps are quartz, orthoclase and anorthite, while accessory minerals include biotite, haematite, magnetite, rutile, titanite and zircon. In the micro-XRF results, there are no inclusions of uranium minerals. This is the case because the micro-XRF works by highly restricting the beam of light to a small sport blocking much of the x-ray making it difficult to analyse sensitive trace elements such as uranium.

Quartz (Si) distribution

Si is the major component for quartz (**Si**O_2), and the Si elemental map (Figure 4.13) shows that quartz is unevenly distributed across the TS2 rock sample. Quartz abundance is high within the oxidation halo section and relatively low in TS2 sections 1 (~30%) and 3 (~36), respectively. Within the oxidation halo, quartz concentration is high in TS2 sections 4 (~38%) and 5 (37%) compared to TS2 section 2 (~36%). Tiny quartz grains throughout the rock sample occur as inclusions in feldspar, whereas coarse and pegmatitic quartz crystals form quartz chains and clusters, which are common in the oxidation halo transition zones.

Orthoclase (K, Al and Ca) distribution

Potassium (K) and Aluminium (Al) are the most dominant elements distributed with a high concentration throughout the TS2 rock sample (Figure 4.13). These elements signify the presence of K-feldspar, in particular, orthoclase based on the µ-XRF results. Ca also occurs throughout the rock sample, but its concentration is relatively high in TS2 sections 1 and 3 compared to the oxidation halo. Within the oxidation halo, Ca is higher in TS2 section 2 than in TS2 sections 4 and 5. Based on the chemical composition of orthoclase (**K**$AlSi_3O_8$) and anorthite (**Ca**$Al_2Si_2O_8$), the distribution of K and Al in TS2 represents orthoclase while Ca and Al indicate the presence of anorthite.

Throughout the rock sample, orthoclase crystals are highly fractured, and the fractures are filled with quartz resulting in intergrowth relationship structures between orthoclase and quartz. The fracturing of orthoclase is very high in TS2 sections 4 and 5, where the concentration of quartz is higher compared to the other sections.

Titanium (Ti) and Zirconium (Zr) distribution

The titanium and zirconium elemental maps (Figure 4.13) indicate these elements are unevenly distributed in the TS2 sections. A high concentration of Ti and Zr is in TS2 sections 4 and 5, with section 4 having the highest concentration. Ti is a diagnostic feature of both rutile (**Ti**O_2) and titanite (Ca**Ti**O_6) meaning that in the TS2 there is probably a high occurrence of rutile and titanite.

Iron (Fe) and manganese (Mn) distribution

Iron is a primary chemical component for haematite (**Fe**$_2O_3$**)** and magnetite (**Fe**$_3O_4$). It is also a significant component for biotite (K (Mg, **Fe**)$_3AlSi_3O_{10}(OH)_2$). Manganese is not a free element in nature, and it always occurs in association with iron-bearing minerals like haematite and magnetite *(https://en.wikipedia.org/wiki/Manganese).* So, the occurrence of Fe and Mn in TS2 rock samples

signifies the presence of haematite/magnetite and biotite. Fe and Mn elemental maps show that these elements are distributed throughout the rock sample, however, a high concentration occurs in the oxidation halo, especially in TS2 sections 4 and 5 (Figure 4.13). High Fe concentration within the oxidation halo demarcates the extent of oxidation halo boundaries (Figure 4.13).

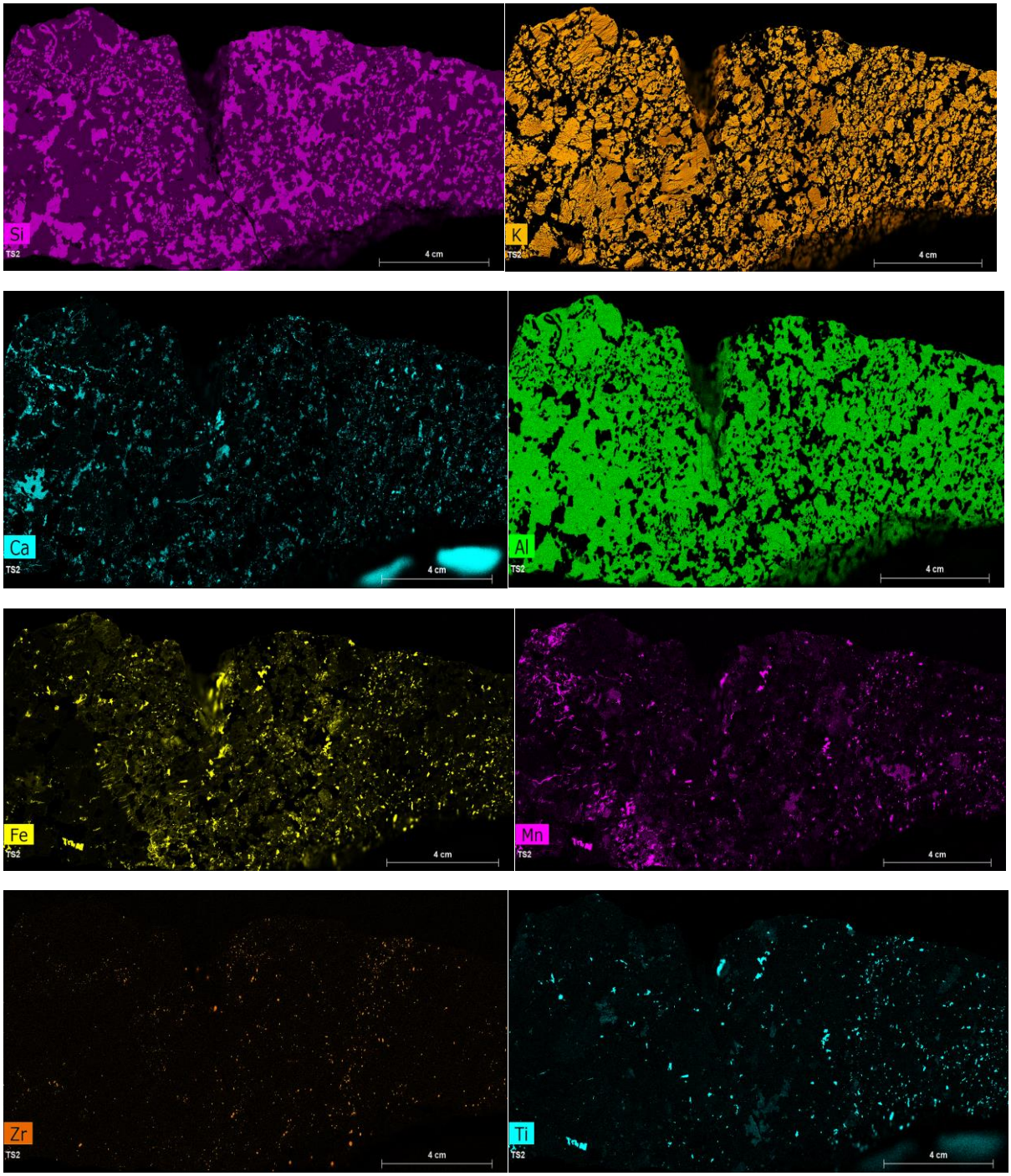


Figure 4.13: Micro-XRF element maps for (Si, K, Al, Fe, Mn, Zr, Ti) showing their distribution across sections of a TS2 rock sample. Note: Si- silicon, K- potassium, Ca- calcium, Al- aluminium, Fe- iron, Mn- magnesium, Zr- zirconium, Ti- titanium

4.4 Thin Section Petrography

The petrographic analysis of the thin sections was done to document detailed information about mineralogy, textural and structural features of the rock samples. The thin section observations also helped to determine alteration types occurring in both rock samples.

4.4.1 TS1 (D-type SLG) petrography

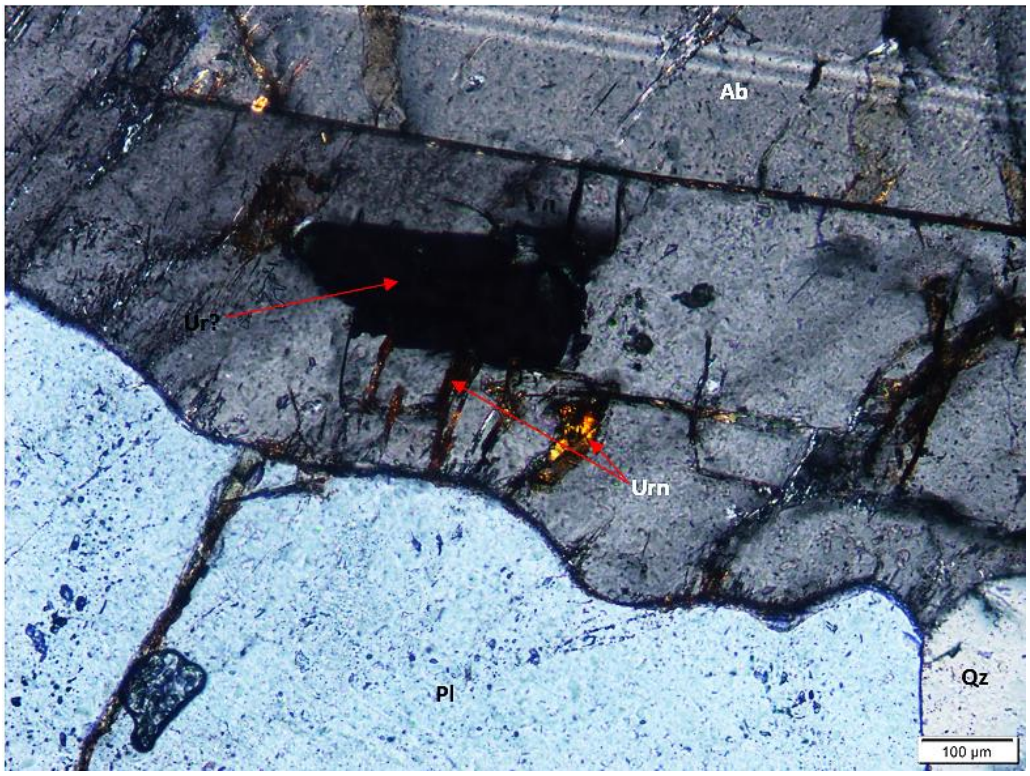
Eight thin sections were analysed for mineralogy, textural and structure features and alteration styles using a petrographic microscope. Mineral grain size measurements using full thin section images were done with the help of the GIMP software.

Mineralogy

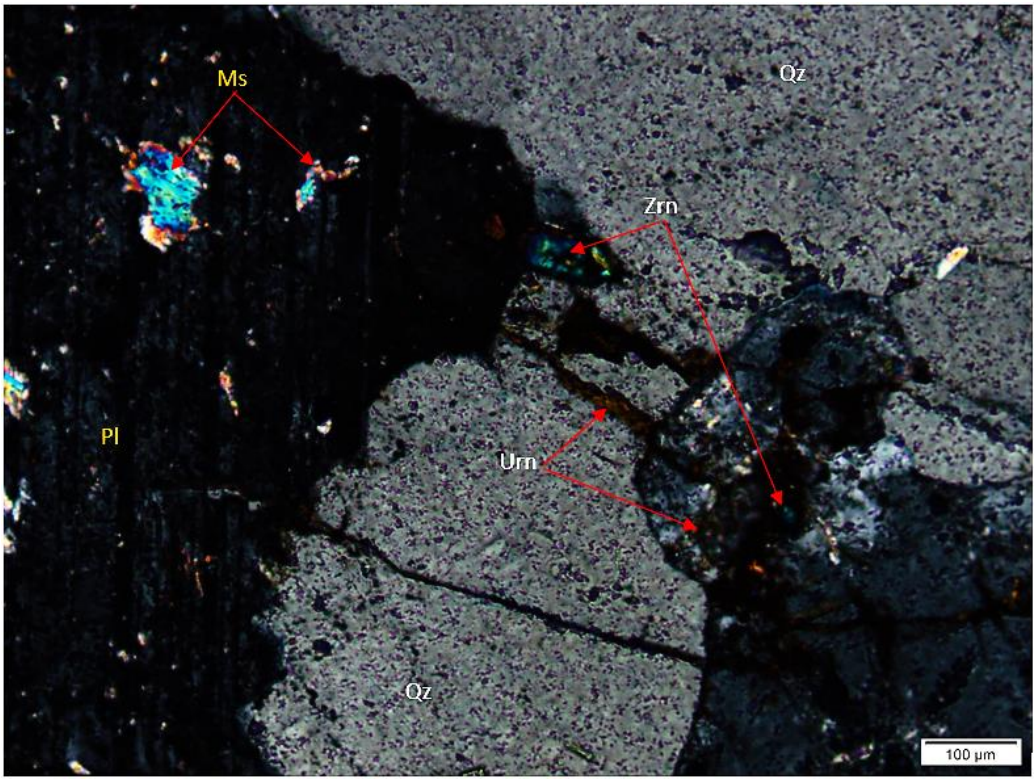
Thin section observations show that the major rock-forming minerals dominating sample TS1 are quartz and plagioclase feldspar mainly albite (Table 4.2). Accessory minerals observed in TS1 include biotite, haematite, muscovite and U-bearing minerals (uraninite, uranophane and zircon). Uranophane and zircon are common in the feldspar-quartz contact zones, feldspar cleavage and fractures and less in the quartz fractures. Uraninite also occurs in association with haematite being surrounded by a uranophane halo (Figure 4.14c). Among the TS1 sections, a high occurrence of uranophane is observed in TS1 sections 2 and 3 (Figure 4.14).

Table 4.2: Thin section descriptive summary results for rock sample TS1 (D-type SLG)

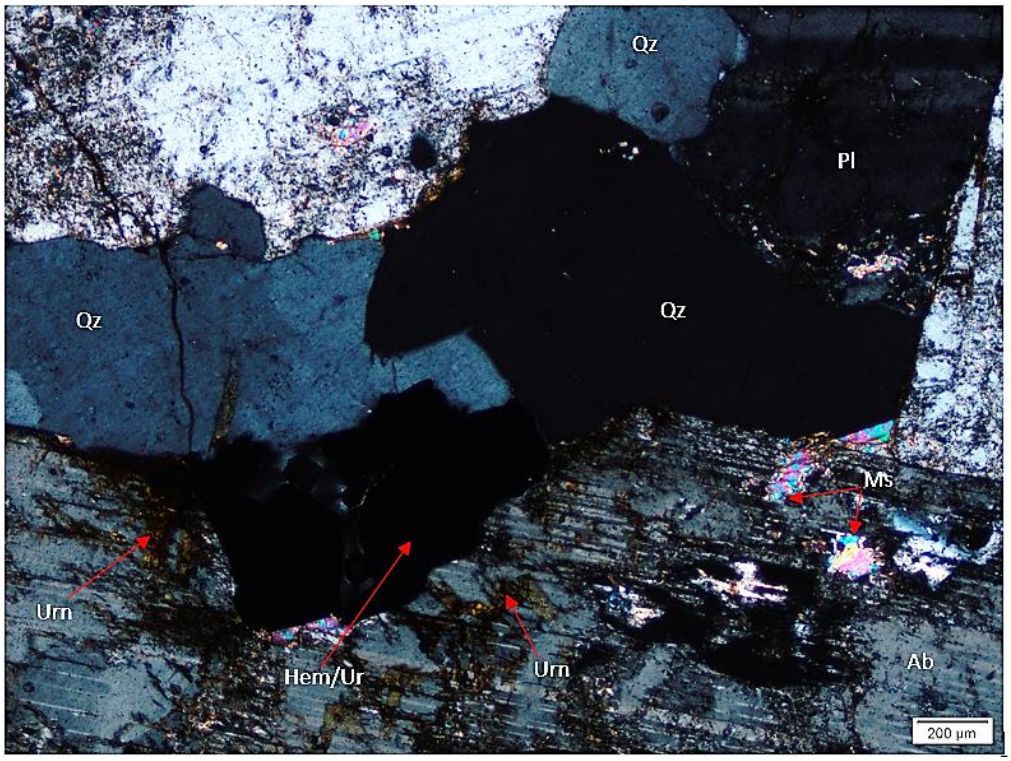
Rock sample section 9	Rock-forming minerals	Accessory minerals	Shape/boundary	Texture/ structures	Alteration	Remarks
TS1 section 2 (TS1-1)	Feldspar (~55%), quartz (~42%) and muscovite (~3%)	Uranophane, uraninite? and zircon	Subhedral-euhedral plagioclase, subhedral-anhedral (quartz). Embayment contact and intergrowth relationship between quartz and feldspar.	Pegmatitic (quartz: ~1mm - <8mm and feldspar: ~1mm - >11mm). Few quartz chains structures.	Feldspar sericitisation, uranium radiation alteration of quartz-feldspar contacts zones and metamictisation	U-bearing minerals are common in the quartz-feldspar contact zone, within feldspar fractures and less in quartz. U-bearing minerals occurrence show high concentration where feldspar is highly altered.
TS1 section 3 (TS1-2)	Feldspar (~45%), quartz (~52%) and, muscovite (~3%)	Same as above	Same as above	Coarse-grained (quartz: <1mm - <10mm and feldspar: ~1mm - < 8mm). Quartz chains and clusters	Same as TS1 section 2	More uranophane in both feldspar and quartz fractures and quartz-feldspar contact zones.
TS1 section 4 (TS1-3 and TS1-5)	Quartz (~53%), Feldspar (~43%), muscovite (~2%) and biotite (~2%)	Same as above except for uraninite	Same as above and with also quartz and biotite having intergrowth relationship	Coarse-grained (TS1-3) to pegmatitic (TS1-5). Quartz chains and clusters	Same as TS1 section 2, but also with biotite chloritisation	High occurrence of zircon in quartz-feldspar contacts zones, but also in biotite. Less uranophane is observed compared to TS1 sections 2 and 3, but its concentration is > the TS1 section 5. High uranium radiation alteration of quartz-feldspar contacts zones radiating fractures around zircon and staining of quartz-feldspar edges with dark coloured materials.
TS1 section 5 (TS1-6 and TS1-7)	Quartz (~47%), feldspar (~53%), Ms (~2%)	Same as above except for uraninite	Same as above	Pegmatitic (quartz: ~6mm - <18mm and feldspar: ~1mm - <12mm). Quartz chains and clusters	Same as TS1 section 2 but with less alteration	Less uranophane in quartz-feldspar contacts zones compared to TS1 sections 2 and 3 but > in TS1 section 4.



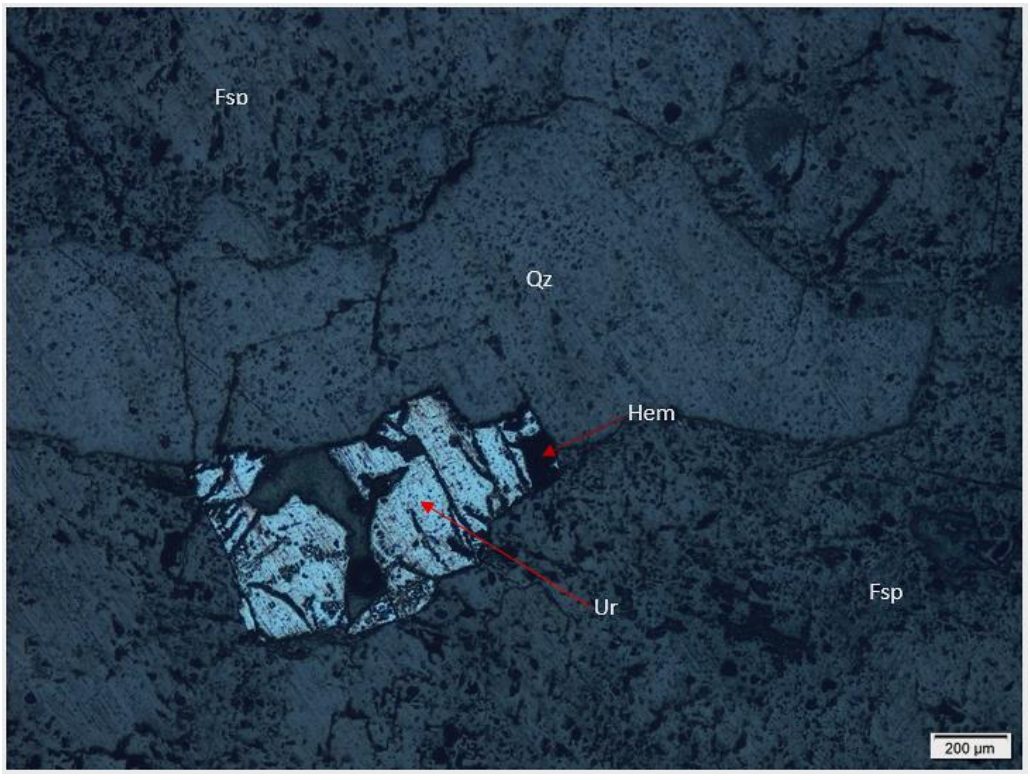
A



B



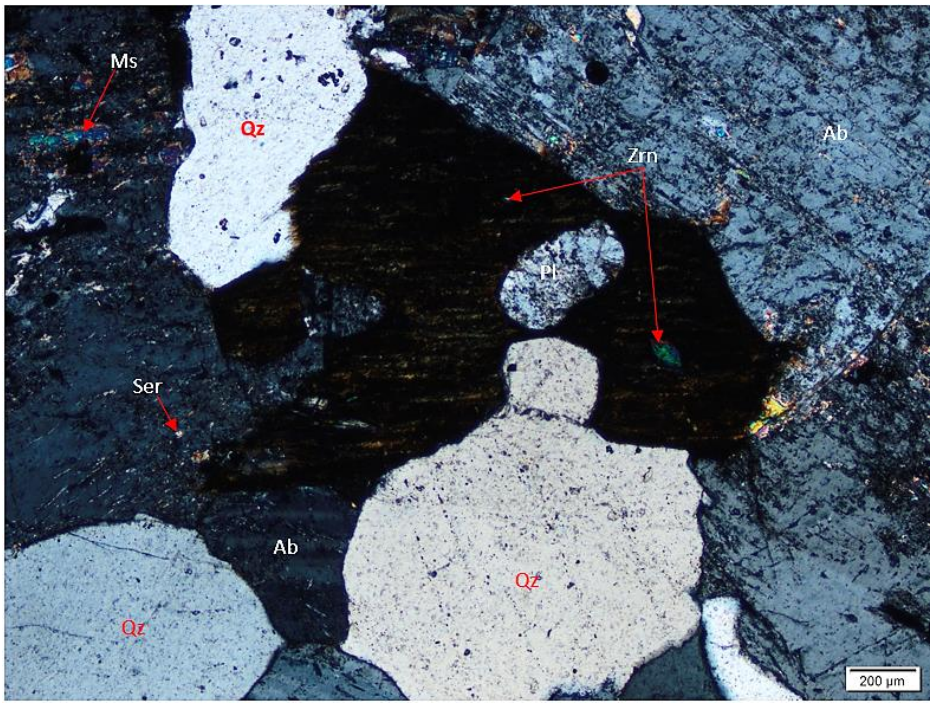
C



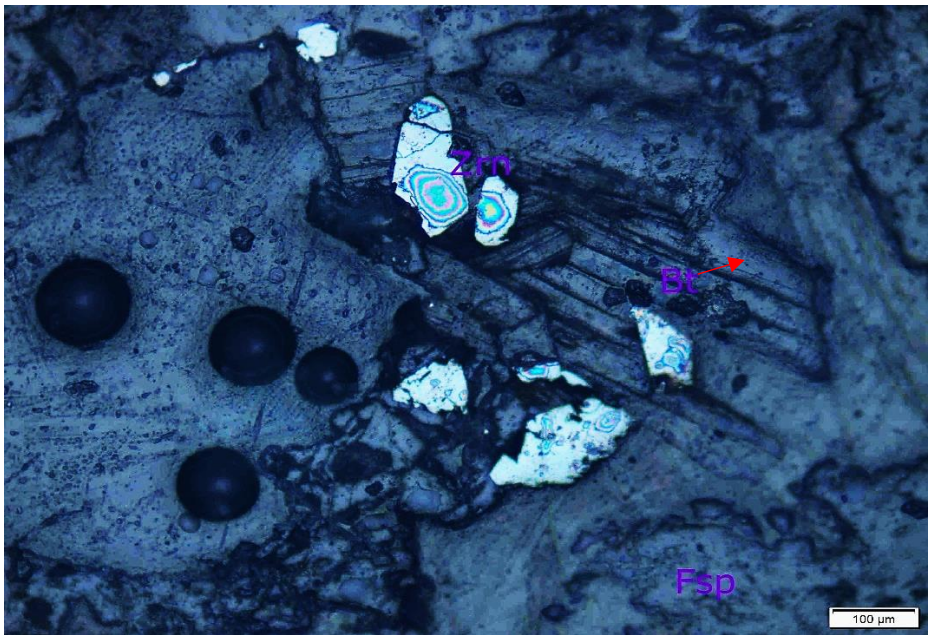
D

Figure 4.14: TS1 sections 2 and 3 domains showing the occurrence of U-bearing minerals. A) TS1-2 (XPL) domain of TS1 section 2 showing the distribution of U-bearing minerals in feldspar. B) TS1-3 (XPL) domain of TS1 section 3 XPL image showing zircon and uranophane in quartz-feldspar contact zones, and uranophane within plagioclase and quartz fractures. C) Another area TS1 section 3 showing haematite/uraninite being associated with uranophane. D) Reflected light (rfl) photograph of B) showing haematite and uraninite. Note: Ab- albite, Ms- muscovite, Fsp- feldspar, Zrn- zircon, Qz- quartz, Hem- haematite, Ur- uraninite, Urn- uranophane.

Although the accessory U-bearing minerals occur throughout the sample, the greatest abundance of these minerals is observed in the TS1 section 3 (TS1-3) and TS1 section 4 (TS1-5) compared to the other sections in the sample. Zircon shows a strong association with biotite in the TS1 sections 3 and 4, the only sections in the D-type SLG sample being observed with biotite (Figures 4.15).



A



B

Figure 4.15: TS1 sections 3 and 4 domains showing association of U-bearing minerals with biotite. A) TS1 section 3 (TS1-3- XPL) showing chloritised biotite having abundant zircon, and B) TS1 section 4 (TS1-5- rfl) showing clusters of zircon crystals associated with biotite. The rainbow halos on the minerals in B are probably finger grease. Note: Fsp- feldspar, Bt- biotite, Qz- quartz, Ab- albite, Zrn- zircon, Ser- sericite

Alteration

Thin section observations show that the TS1 rock sample experienced several alteration styles which include sericitisation, chloritisation, radiation alteration and metamictisation. Throughout the rock sample, feldspar is highly sericitised, and it is evidenced by the development of sericite and muscovite associating the feldspar, in particular the albite. Biotite in the TS1 section 4 (Figure 4.15A) shows that it is highly chloritised. Uranium radiation alteration effects on quartz and plagioclase occur throughout the sample, with TS1 section 4 (TS1-5) (Figure 4.16) showing the highest effects of uranium radiation. TS1 section 4 also indicates well-developed radiating fractures around zircon crystals (Figure 4.16B), which formed as a result of the metamictisation process occurring in zircon.

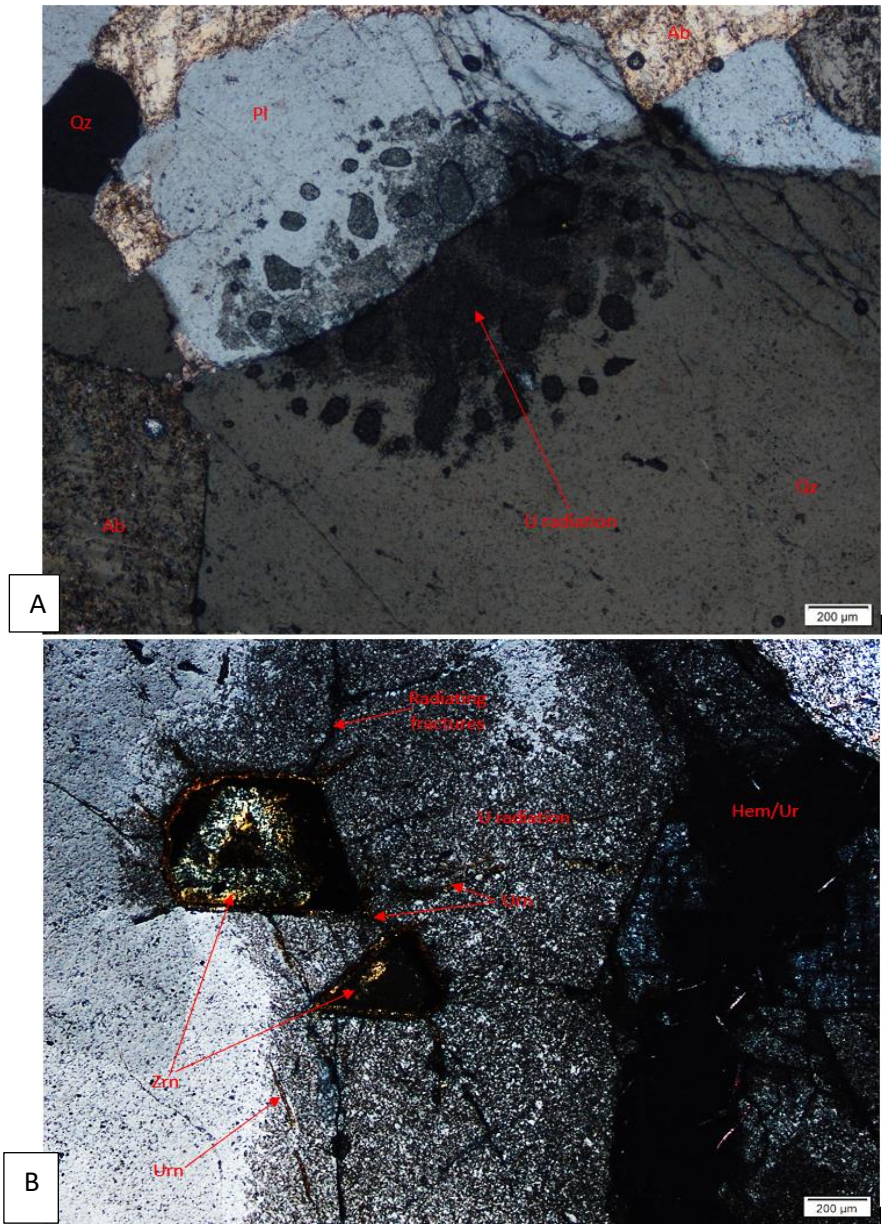


Figure 4.16: Photomicrograph domains of TS1 section 4 showing uranium radiation and metamictisation alterations. **(A)** TS1-5.1 (XPL) domain of TS1 section showing uranium radiation alteration (dark colouration) of quartz-feldspar contact boundary. **(B)** TS1-5 (XPL) domain of TS1 section 4 showing metamictisation process forming radiating fractures around zircon filled with uranophane. Note: Qz- quartz, Zrn- zircon, Hem/Ur- haematite/uraninite, Ab- albite, Pl- plagioclase, U- uranium

Texture and structures

Appendix 8 presents mineral grain sizes for TS1-1, TS1-2, TS1-5, and TS1-7 measured using full thin section images. TS1 section 3 grain size measurements also represent the grain sizes for TS1 sections 1, 3, and 6 (Figure 4.1), as these sections show similar mineralogical and textural features. Using the mineral grain size measurements (Appendix 8); average grain size, modal grain size range and grain size range for each rock sample section were determined (Appendix 9). Figure 4.17 below shows the distribution of average mineral grain sizes across the D-type SLG rock sample.

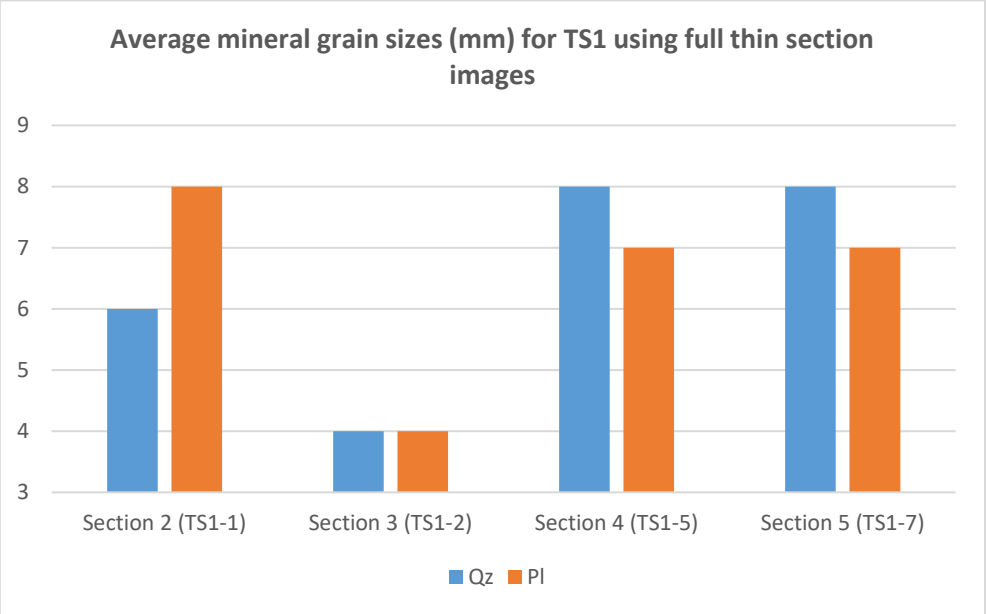


Figure 4.17: Graphical presentation of the mean grain sizes for TS1 determined using full thin section images. Note: Qz- quartz, Pl- plagioclase

Figure 4.17 results show that most of the TS1 sections are dominated by coarse-grained minerals except for TS1 section 3, which have medium-grained textured minerals. The mineral grain size measurement results (Appendices 8; 9) also show that TS1 sections 2 and 6 are dominated by 5-10 mm mineral grain sizes range with a significant amount of large > 10 mm mineral grains . TS1 section 3 is dominated by 2-5 mm mineral grain sizes ranges, and also it contains more <2 mm mineral grain sizes. For TS1 section 4, the results show that 5-10 mm mineral grain sizes range dominates the section. Structurally, quartz chains and clusters are observed in all TS1 sample sections, with prominent chain structures in the TS1 section 5 (TS1-7) (Appendix 1).

4.4.2 TS2 petrography

Eleven thin sections prepared from the TS2 rock sample (Table 3.2) were analysed for mineralogy, alteration and textural features using a petrographic microscope. Mineral grain size measurement using full thin section images was determined using GIMP software.

Mineralogy

Thin sections observations show that K-feldspar, quartz and plagioclase (Table 4.3) are the principal rock-forming minerals for the E-type SLG rock sample. Accessory minerals occurring in the TS2 include biotite, muscovite and U-bearing minerals such as uranophane and zircon. Throughout the

rock sample, quartz exhibits two forms: older quartz (Q1) and younger quartz (Q2). The Q1 is overprinted by the Q2 (Appendix 2).

Microcline visibility in most of the TS2 sample sections is obscured by the albite overgrowth exsolution yellow structures (Figure 4.18), and the obscuring effects are so intense in the transition zone between the D-type and the oxidation halo core zone.

Table 4.3: Thin section petrographic analysis results for TS2 sample, the oxidation halo sample (E-type SLG).

Section #	Rock-forming minerals	Accessory minerals	Shape/boundary	Texture/structures	Alteration	Remarks
TS2 section 1 (TS2-1)	Feldspar (~63%) quartz (~35%), biotite (~2%)	Zircon, uranophane	Anhedral, intergrowth, and embayment contact between quartz and feldspars. Euhedral (feldspar)	Pegmatitic (quartz: <2 mm - > 10 mm and feldspar: ~4 mm- > 15 mm. Quartz chains and clusters, and myrmekite in feldspar (albite)	Feldspar sericitisation, biotite chloritisation, uranium radiation alteration of quartz-feldspar edges	Biotite content and iron oxides staining of feldspar increase towards oxidation halo outer zone. Quartz and feldspar are highly altered where biotite exhibits a high association of U-bearing minerals.
TS2 section 2 (TS2-4 and TS2-10)	Quartz (~38%), feldspar (~60%), biotite (~2%),	Zircon, uranophane and iron oxide (haematite)	Same as above	Pegmatitic (Quartz: <1 mm - >10 mm and feldspar: ~3 mm - >10 mm). Myrmekite in feldspar (plagioclase). Quartz chains	Same as TS2 section 1	TS2 section 2 contain less uranium-bearing and iron oxide compared to TS2 sections 4 and 5 but is relatively higher than TS sections 1 and 3.
TS2 section 3 (TS2-6 and TS-12)	Quartz (~44%), feldspar (~53%), biotite (~3%)	Less zircon, haematite and uranophane	Same as above	Coarse-grained (Quartz: <1 mm - <10 mm and K-feldspars: ~ 2 mm - <10 mm). Less quartz chains and clusters	Same as TS2 section 1	Microperthite dominates TS2 section 3 and it has fewer U-bearing minerals. Less uranium radiation alteration of quartz-feldspar boundaries is observed in the section.
TS2 section 4 (TS2-5 and TS2-11)	Quartz (~43%), feldspar (~52%), biotite (~5%)	Same as TS2 section 2	Same as above	Medium- to coarse-grained (quartz: <1 mm-<8 mm and feldspar: ~2 mm - < 10 mm). Quartz chains and clusters. Albite exsolution structures over microcline. Myrmekite in albite	Same as TS2 section 1	The section contains a greater number of U-bearing minerals associated with biotite. High staining of feldspars with iron oxides. Feldspar-quartz contact boundaries are highly altered with uranium radiation alteration.
TS2 section 5 (TS2-2, TS2-3, and TS2-9)	Quartz (~40%), feldspar (~53%), biotite (2%)	Same as TS2 section 2	Same as above	Pegmatitic (quartz: <1 mm - <12 mm, K-feldspar: ~1 mm - >16 mm Quartz chains and clusters. Myrmekite in albite. Quartz chains and clusters	Same as TS2 section 1	Microcline highly stained with light yellow feldspar exsolution structures. Albite within microperthite is highly stained with iron oxides compared to microcline. More uranophane observed quartz-feldspar contact zones

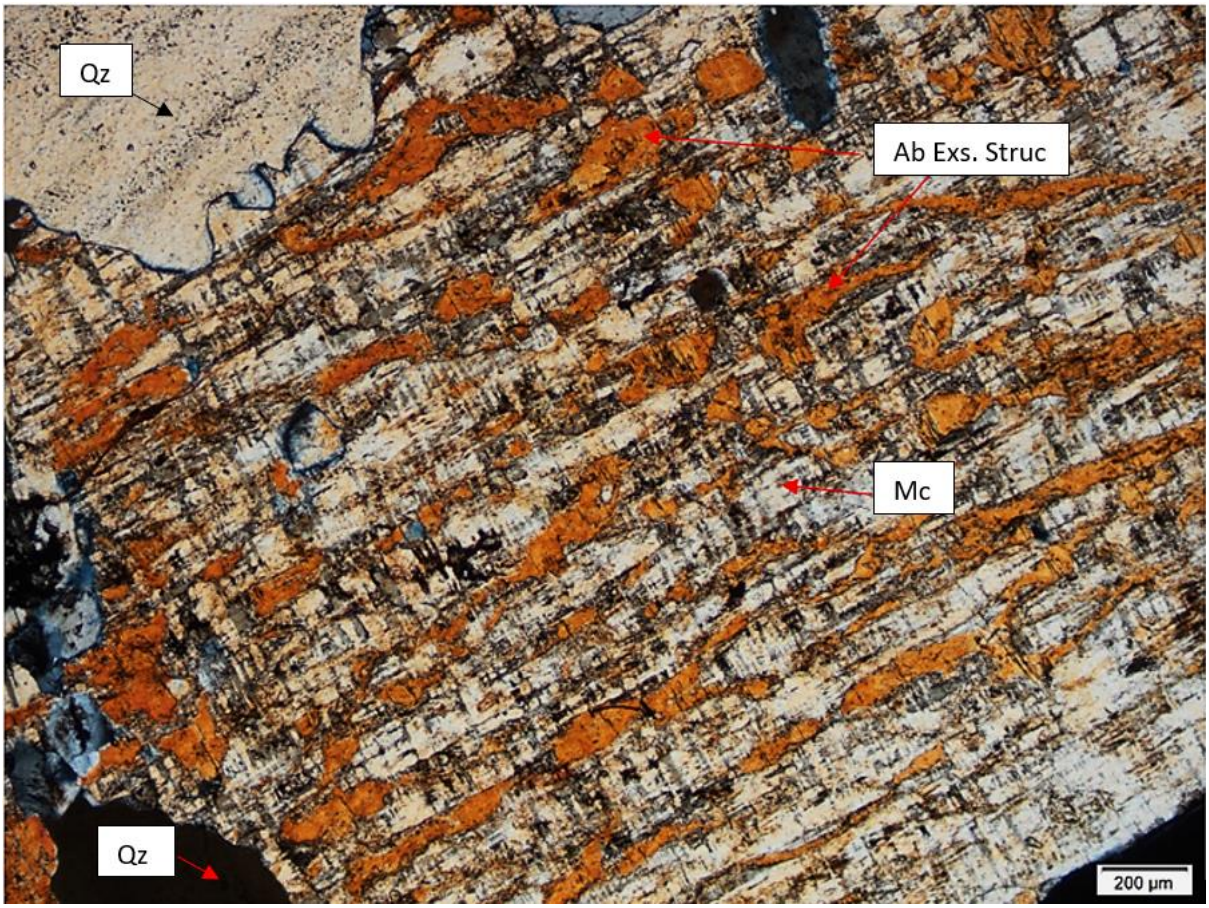


Figure 4.18: Photomicrograph domain of TS2 section 2 (TS2-3) (XPL) showing the growth of albite exsolution yellow structures after microcline. Note: TS2-3 represents the thin section number prepared from TS2 section 2. NB: Mc- microcline, Qz- quartz, Exos- exsolution

Throughout the E-type SLG sample, microcline is not associated with accessory U-bearing minerals, except when the sample section exhibits highly sericitised albite. The oxidation halo core zone has a relatively high microcline abundance compared to other rock-forming minerals. Biotite content increases from both the D- type and E-type sections towards the oxidation halo transitional zones (Appendix 3). Accessory U-bearing minerals such as zircon are abundant in the oxidation halo transitional zones, which have a high occurrence of biotite (Figure 4.19). Plagioclase occurs throughout the sample, but its abundance is also high in the oxidation halo transitional zones. U-bearing minerals are abundant in the altered feldspar, and their abundance is even higher when feldspar occurs in association with biotite. Iron oxide (haematite) staining of feldspar occurs throughout the oxidation halo, with the oxidation halo transitional zones being highly stained, especially the TS2 section 4 (Figure 4.16). Figure 4.20 also shows that the TS2 section 5 contains poorly ordered perthite suggesting that it is transforming into clay minerals.

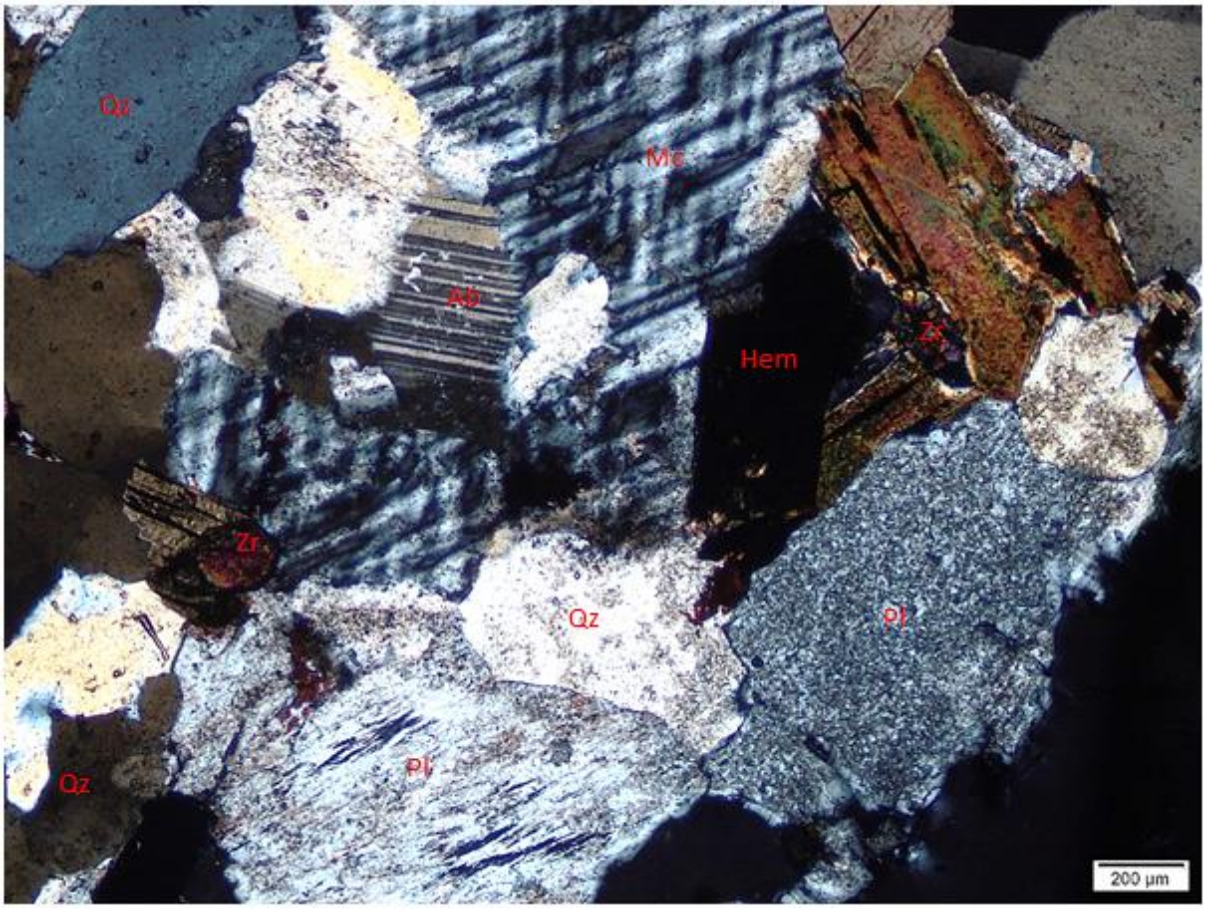


Figure 4.19: Photomicrograph domain of TS2 section 4 (TS2-5) XPL image showing high association of accessory U-bearing minerals such zircon with biotite. Note: Ab- albite, Bt- biotite, Qz- quartz, Pl- plagioclase

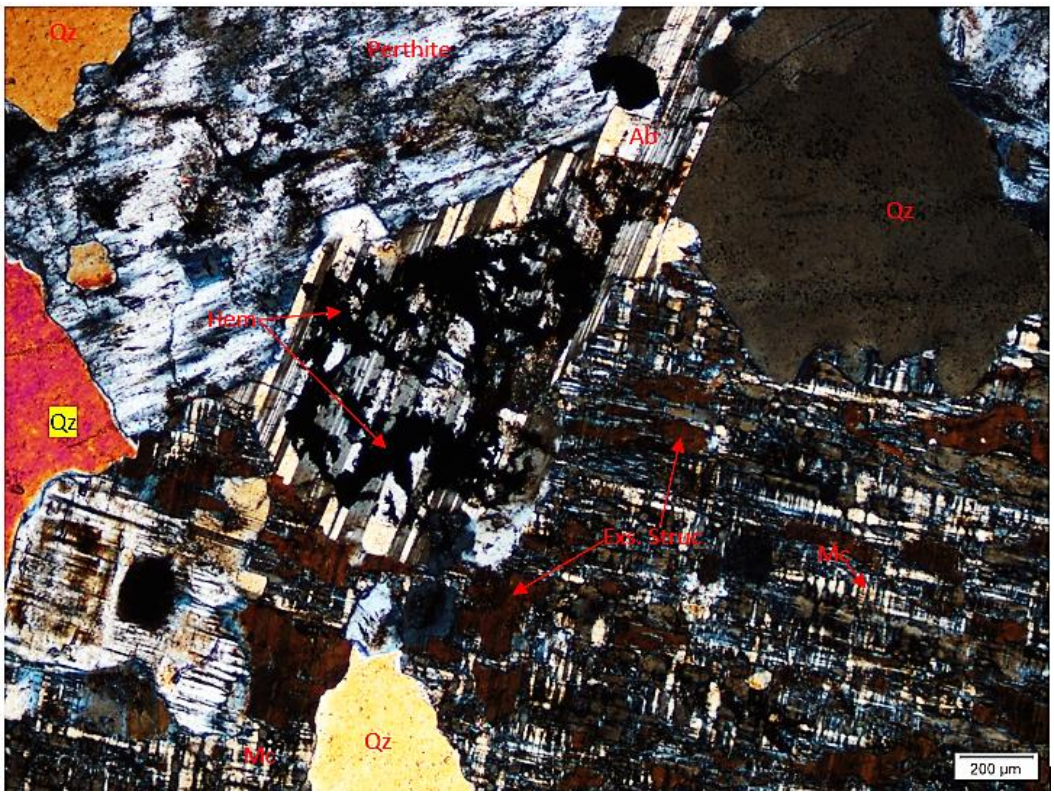
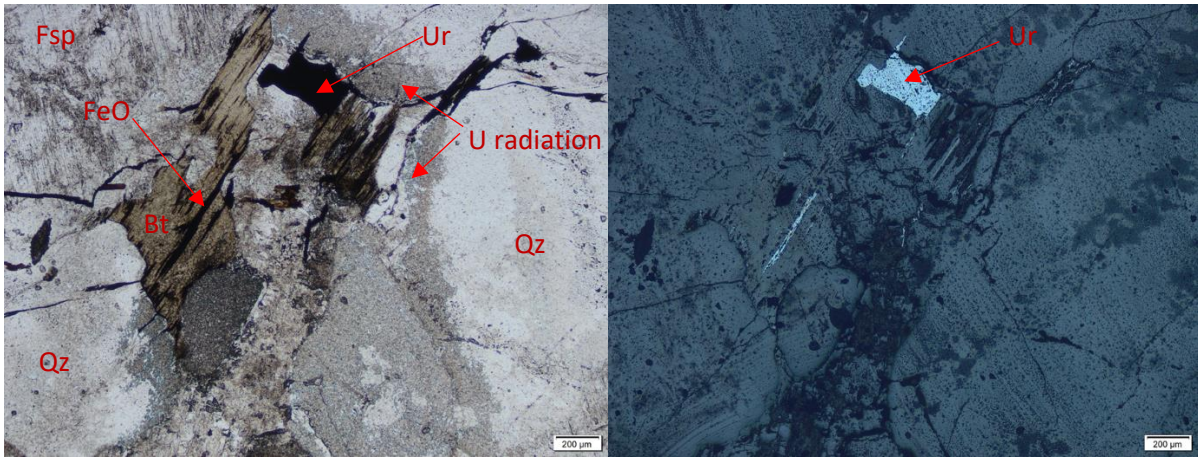


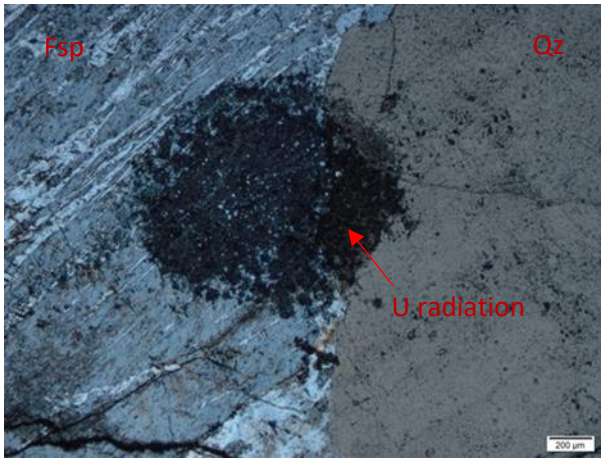
Figure 4.20: Photomicrograph domain of TS2 section 5 (TS2-3) XPL image showing iron oxide staining of albite as well as overgrowth of albite exsolution structures over microcline (tartan twining). Albite is strongly coated with iron oxides followed by perthite, and the microcline is least coated feldspar with iron oxides. Note: Qz-quartz, Fsp- feldspar, FeO/Ur- iron oxide/uranium, Ab-albite, Mc- microcline, Exs- exsolution, Struc- structure

Alteration

Thin section observations show that sericitisation, chloritisation, uranium radiation, metamictisation and haematisation are some of the alteration events the TS2 rock sample was subjected to. Feldspar in the TS2 rock sample is also sericitised but not to the same extent compared to alteration in TS1. Uranium radiation effects are commonly observed in the quartz-plagioclase contact zones and less common in the individual feldspar and quartz crystals (Figure 4.21).



A B



C

Figure 4.21: Photomicrographs domains of TS2 section 4 (PPL) (A) and (B) is the same domain A but under rfl showing uraninite and (C) (XPL) domain of (B) showing the effects of uranium radiation alteration. Note: (A) also shows haematite/titanite (iron oxides) filling the biotite blades and cleavages, and uraninite occurring in association with biotite

Within the oxidation halo, TS2 sections 4 and 5 exhibit high uranium radiation alteration effects compared to TS2 section 2. Biotite throughout the rock sample shows that it is highly chloritised, with prominent chloritisation observed in TS2 sections 4 and 5. Weak zones and edges of altered biotite show that they are being filled with iron oxides such as haematite and titanite. Accessory U-bearing minerals such as uraninite (Figure 4.21B), zircon and uranophane are common in highly altered biotite (Figure 4.22). In many cases, radiating fractures filled with uranophane are observed developing around uraninite and zircon crystals (Figure 4.22). The development of radiating fractures around the zircon is a result of the metamictisation process.

Haematisation is one of the major alterations events the oxidation halo sample (TS2) was subjected to. This type of alteration is evidenced by the iron oxide (haematite) staining of feldspar minerals in the oxidation halo, and haematisation defines the boundary of the oxidation halo showing red colouration. Thin section observations show that albite is strongly stained with iron oxides compared to other feldspar minerals such as perthite and microcline. Within the oxidation halo, albite in the oxidation transition zones is highly stained with iron oxides resulting in these sections having a deep red colouration unlike the oxidation halo core zone (Figures 4.20; 24)

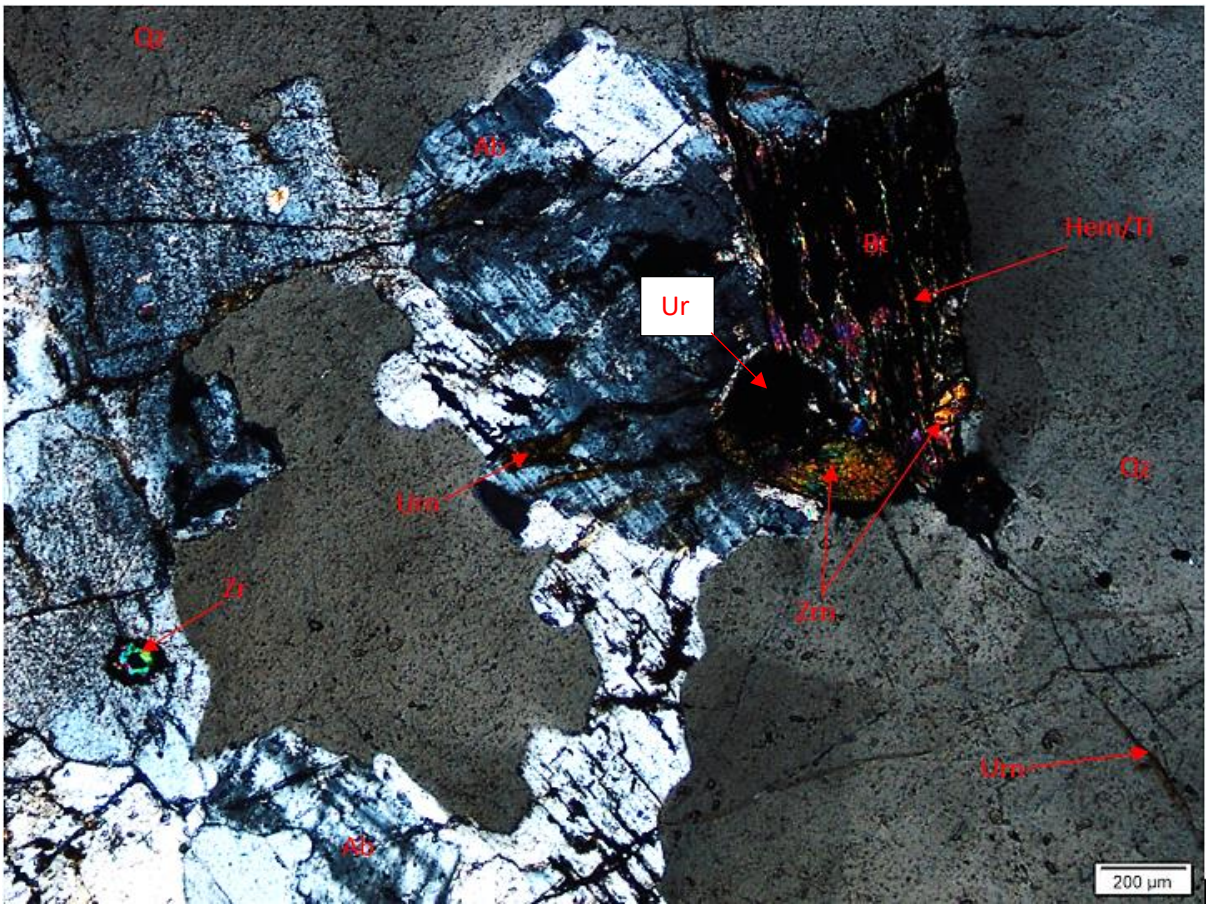


Figure 4.22: Photomicrograph domain of TS2 section 5 (TS2-2) XPL image showing chloritised biotite being replaced by U-bearing minerals. Radiating fractures around uraninite and zircon in both plagioclase and quartz are filled with uranophane. NB: Zr- zircon, Ab- albite, Bt- biotite, Qz- quartz, Urn- uranophane, Ur-uraninite

Textural and structural features

Mineral grain sizes were measured using TS2 full thin section images, and Appendix 10 presents the results. Appendix 10 results were then analysed for mineral grain size average, modal mineral grain sizes and mineral grain sizes range as presented in Appendix 11. Figure 4.23 shows the distribution of average mineral grain sizes across the rock sample. Results show that TS2 sections 1 (D-type) and 2 (mainly the core zone of the oxidation halo) are dominated by > 10 mm mineral grain sizes. For the oxidation halo transition zones (TS2 sections 4 and 5) the 2-5 mm mineral grain size range dominates the sections. In the E-type section TS2 section 3), 5-10 mm mineral grain sizes dominate the section. TS2 section 3 has also a relatively high number of more than 10 mm grain sizes for both quartz and K-feldspar.

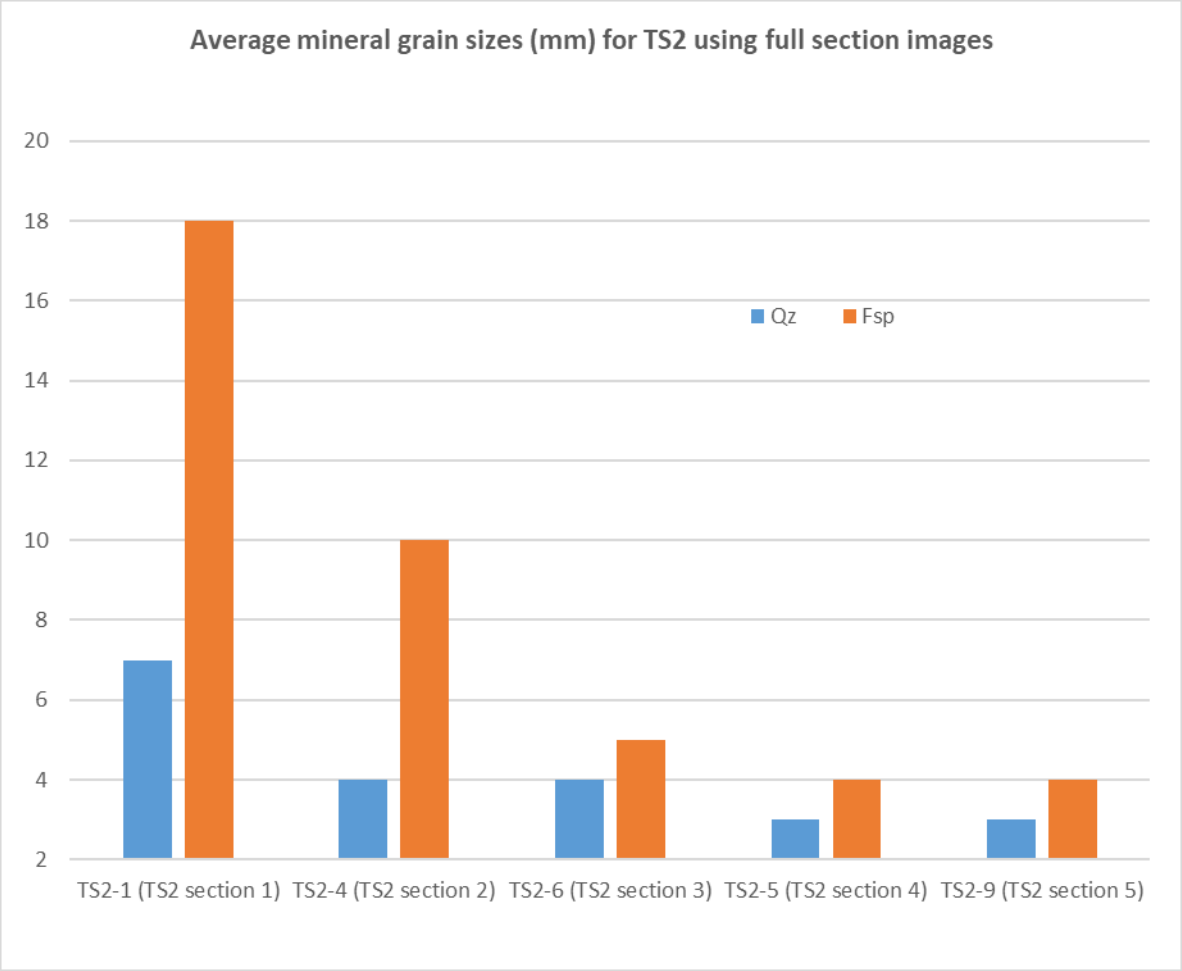


Figure 4.23: Graphical presentation of the mean mineral grain sizes for TS2 determined using full thin section images.

As the case with TS1, large crystals of quartz in TS2 also form quartz chains and cluster structures. Within the oxidation halo zone, especially the transitional zones, plagioclase shows the development of myrmekite structures with quartz (Figure 4.24).

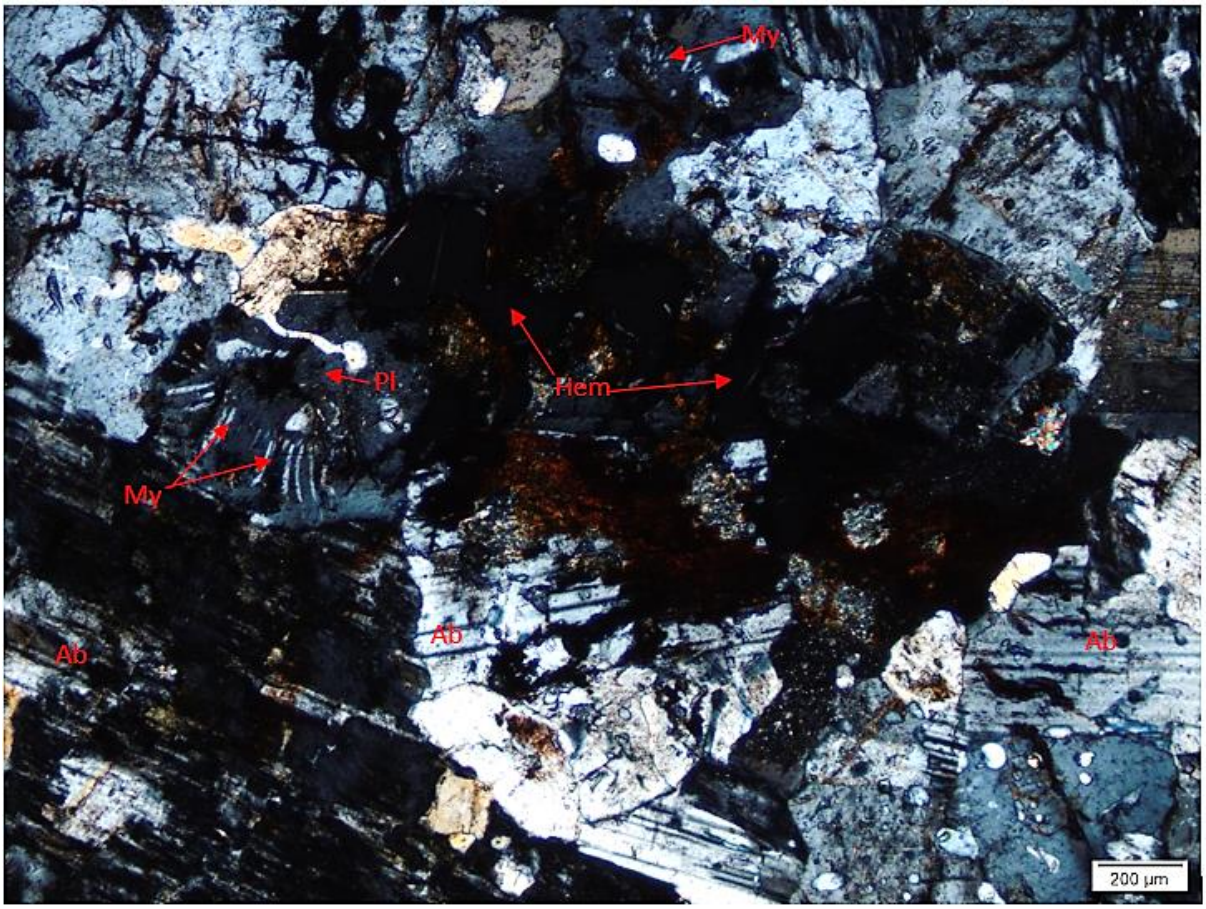


Figure 4.24: Photomicrograph domain of TS2 section 5 (TS2-3) XPL image showing the development of myrmekite structures in plagioclase and iron oxide staining of plagioclase (haematisation). Note: My- Myrmekite, Hem- haematite, Ab- albite, Pl- plagioclase. Myrmekites are observed in all sections of the oxidation halo, but most of these structures are common in the oxidation halo transitional zones.

4.4.3 Petrography summary

Mineralogy and rock colour variation

The petrography results show that the major rock-forming minerals dominating TS1 are plagioclase (albite) and quartz. Muscovite, biotite, haematite and U-bearing minerals (uraninite, uranophane and zircon) are some of the accessory minerals found in the TS1 sample. The colour for TS1 varies from light to dark, which is due to the unequal distribution of the smoky quartz in various rock sample sections. The dominant rock-forming minerals for TS2 are K-feldspars (microcline, orthoclase and perthite), albite and quartz. The TS2 also has similar types of accessory minerals occurring in the TS1 except that haematite, biotite and U-bearing minerals are common in TS2 sections 4 and 5. The colouration of the TS2 varies from light-red-pink, and colouration is a result of differences in iron oxides (haematite) distribution. In both TS1 and TS2, accessory U-bearing minerals are commonly observed in the feldspar-quartz contact zones, and their abundance is higher when they occur in association with biotite as observed in the TS1 sections 3 and 4, and TS2 sections 4 and 5.

Textural and structural features

In terms of the mineral grain sizes distribution, both TS1 and TS2 rock samples have mineral grain sizes ranging from medium-grained to pegmatitic. The TS1 sections 1, 3 and 6 (TS1) and TS2 sections 4 and 5 (TS2) are dominated by the medium-grained textured minerals; the TS1 sections 2 and 5 (TS1) and TS2 sections 1 and 2 are dominated by the pegmatitic mineral grain sizes and the TS1 section 4 (TS1) and TS2 section 3 are dominated by coarse-grained textured minerals.

The common textural features observed in both TS1 and TS2 rock samples are quartz chains and quartz clusters. Albite exsolution develops over microcline and myrmekites in the oxidation halo transitional zones in TS2.

Alteration styles

The common types of alteration observed in both TS1 and TS2 rock samples are sericitisation, uranium radiation cracks and metamictisation. Sericitisation is shown by the development of sericite and muscovite, which are common in the albite of TS1. The metamictisation process is characterised by the formation of radiating fractures around U-bearing minerals such as zircon. Uranium radiation is known for its effects of altering the quartz-feldspar contact zones with dark colouration (Figure 4.21C) resulting in quartz appearing dark in the hand specimen. The other types of alteration being prominent in the TS2 are albitisation and haematisation. Albitisation is characterised by the overgrowth of albite exsolution structures on microcline, whereas haematisation is known by the distribution of haematite that results in the red colouration of the oxidation halo.

4.5 TIMA results

TIMA analysis of the rock samples was done to determine mineral phases, mineral phase proportions, alteration styles and mineral composition of the rock samples. TIMA lends a qualitative and semi-quantitative quality to the analysis of the thin sections that is more consistent than traditional petrography. TIMA results include BSE images, mineral phase identification, elemental maps and mineral phase association.

Six thin sections, two from TS1 and four from TS2 (Table 4.4), were considered for TIMA studies. The choice of these thin sections was based on the results from petrographic analysis, both texturally and mineralogically. Then, specific domain(s) from the chosen thin sections for TIMA studies were mainly based on mineralogy, which represented the minerals found in a particular thin section. The choice of some specific domains for TIMA studies was also based on the fact that some areas within the thin sections were observed to have certain types of accessory minerals which could not be determined using thin section petrography only, but also through other techniques such as TIMA as the case with domain TS1-2 of the TS1 section 3. The thin section observation for the TS1-2 domain of TS1 section 3 showed the occurrence of a dark phase suggested to be haematite or uraninite. But, through TIMA studies the mineral phase in question was determined to be haematite (Figure 4.26E). Figures A-E in Appendix 13 shows the specific areas selected for TIMA analysis.

Table 4.4: Description of the rock sample sections and domains selected for TIMA analysis

Sample section	Domain (thin section number)	Remarks
TS1 Section 3 (Figure 3.1)	TS1-2 (Figure 3.2)	The targeted area of the thin section represented the overall mineralogy and unknown deep dark brown minerals under both XPL and PPL.
TS1 section 4 (Figure 3.1)	TS1-5 (Figure 3.2)	The specific area targeted represented overall mineralogy, which was observed to have more U-bearing minerals associated with biotite. Note: the targeted area was missed during TIMA analysis.
TS2 section 2 (Figure 3.3)	TS2-4 (Figure 3.4)	Represented the overall mineralogy of the oxidation halo core zone, but also albite exsolution structures developing over K-feldspar, microcline.
TS2 section 3 (Figure 3.3)	TS2-6 (Figure 3.4)	The chosen domain represented the overall mineralogy for the E-type section.
TS2 section 4 (Figure 3.3)	TS2-5 (Figure 3.4)	The domain chosen showed more U-bearing minerals associated with biotite
TS2 section 5 (Figure 3.3)	TS2-9 (Figure 3.4)	Same as above but also the chosen specific area showed a high concentration of iron oxides.

4.5.1 BSE image result

U-bearing minerals are high-density mineral phases and they look bright in BSE images, whereas, silicate minerals such quartz and feldspar are light mineral phases and they look dark in BSE images. The BSE images showed that the oxidation halo transition zones, especially TS2 section 4 (Figure 4.25), contains more high-density mineral phases compared to other sections of both TS1 and TS2 rock samples. After comparing the BSE images with mineral phase maps; the black phase represents unclassified mineral phases, the deep dark grey phase represents albite and quartz phases, the grey phase represents orthoclase and biotite phases, the bright phase represents haematite/magnetite and zircon phases and the very bright phase represents uraninite (Figure 4.25).

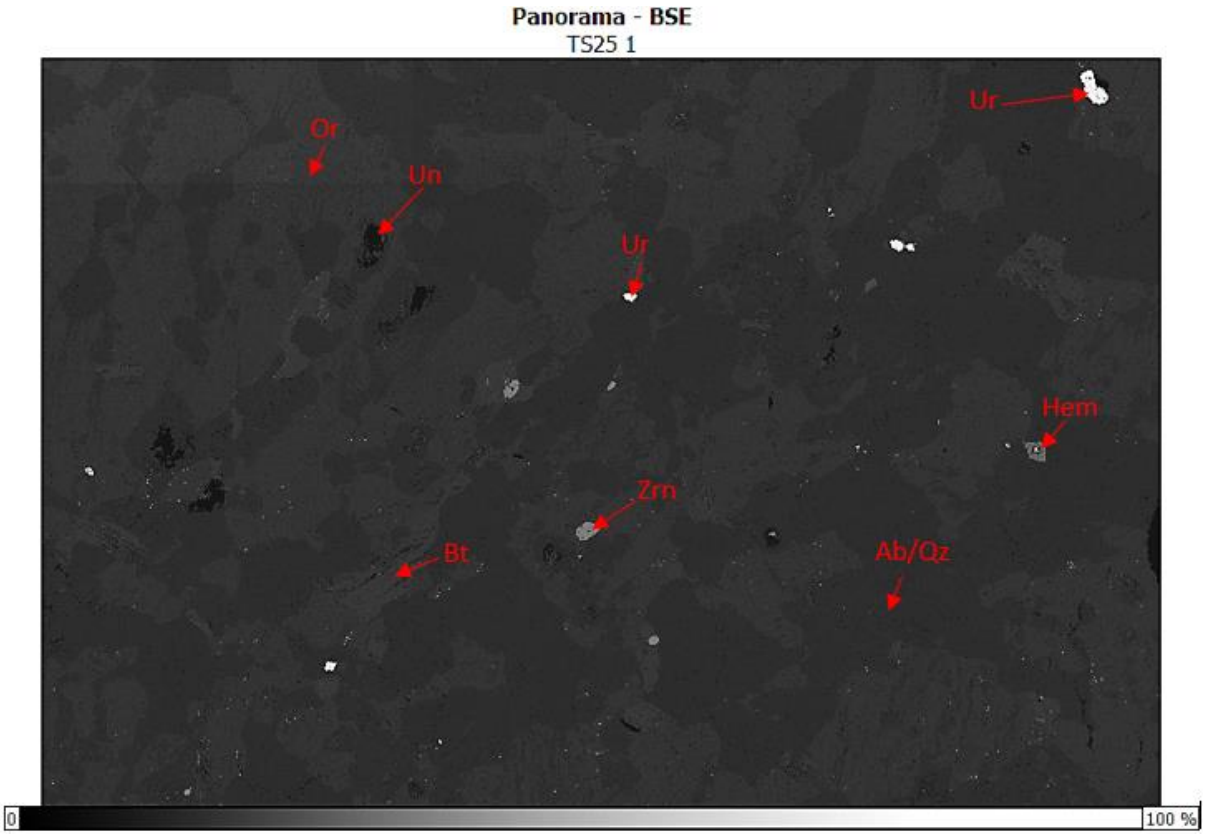
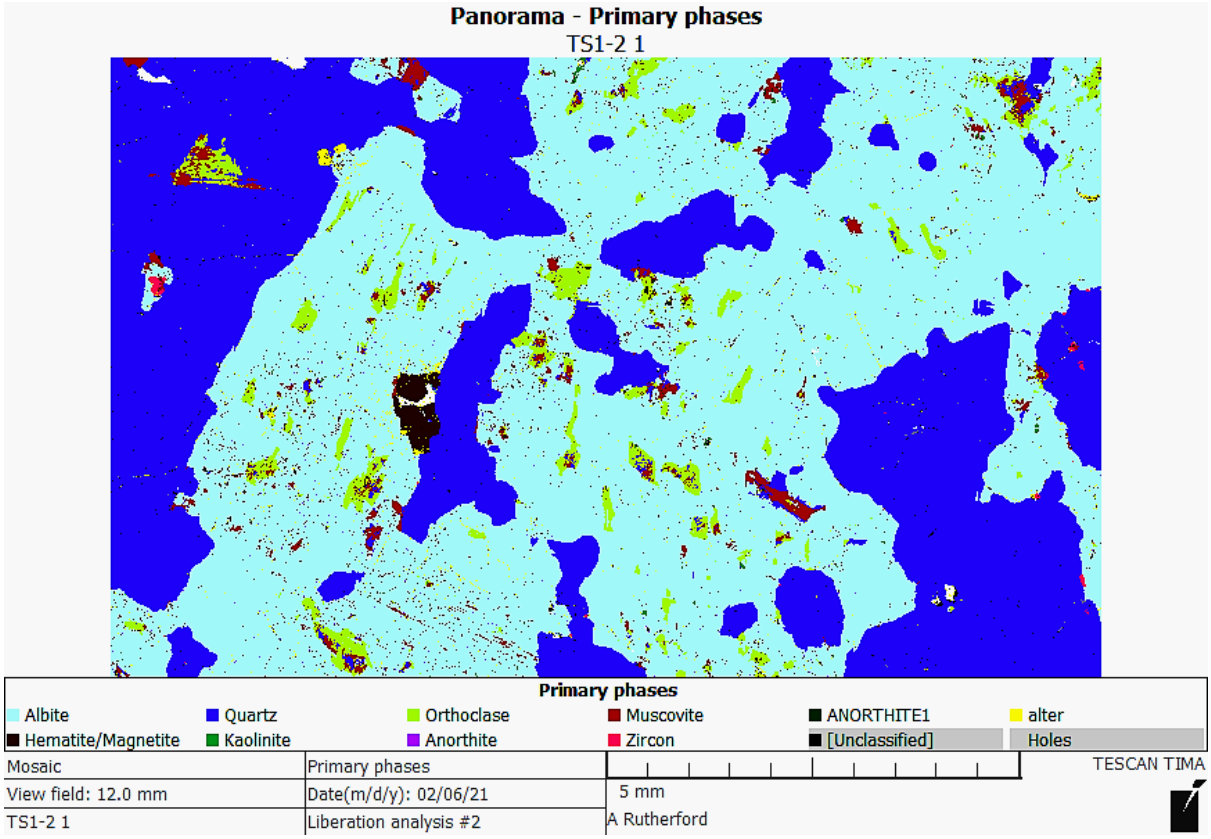


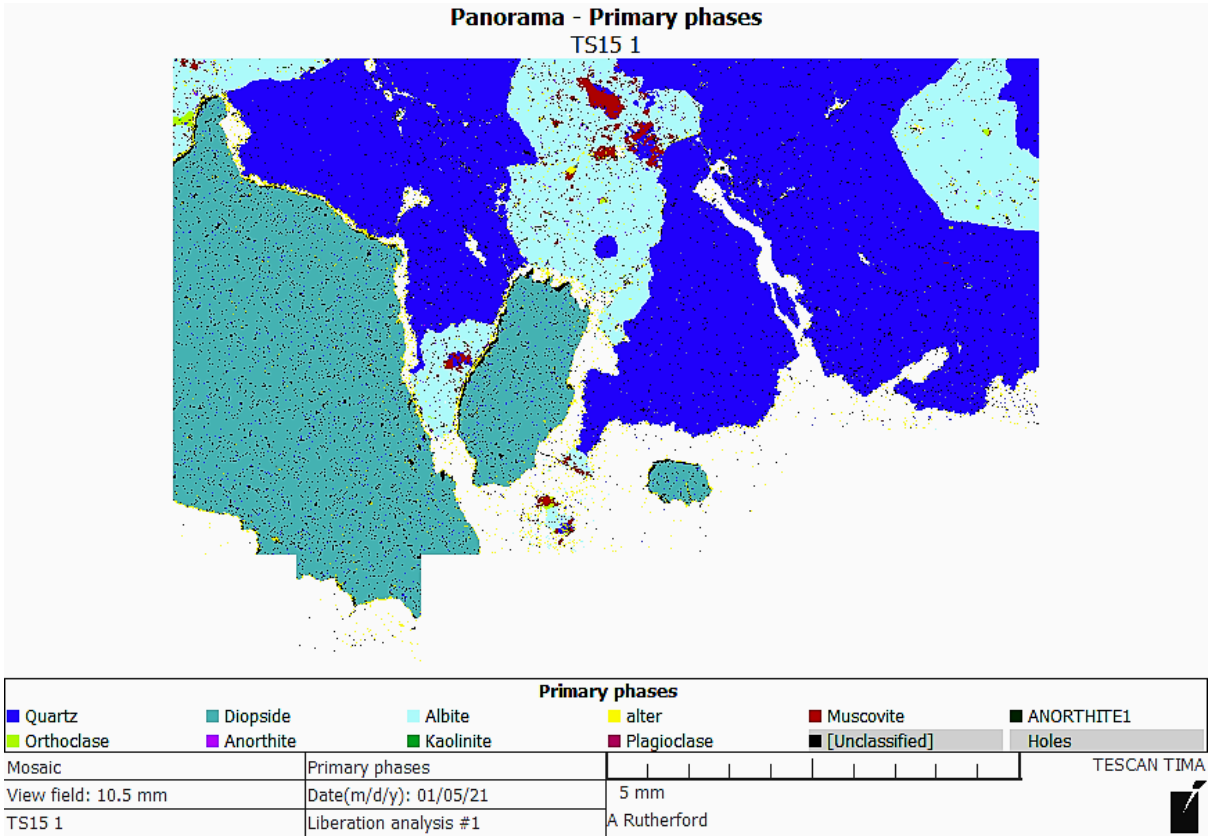
Figure 4.25: BSE image domain for TS2 section 4 (TS2-5) representing various mineral phases found in both TS1 and TS2. Black phase- unclassified phases (Un), which could also represent holes in slide filled with epoxy or cavities within minerals; dark grey phase- albite/quartz (Ab)/Qz) phase; grey phase- orthoclase (Or) and biotite (Bt); bright phase- haematite/magnetite (Hem) and zircon (Zrn) and very bright phase- uraninite Ur). Haematite contains inclusions of uraninite.

4.5.2 Mineral phase maps results

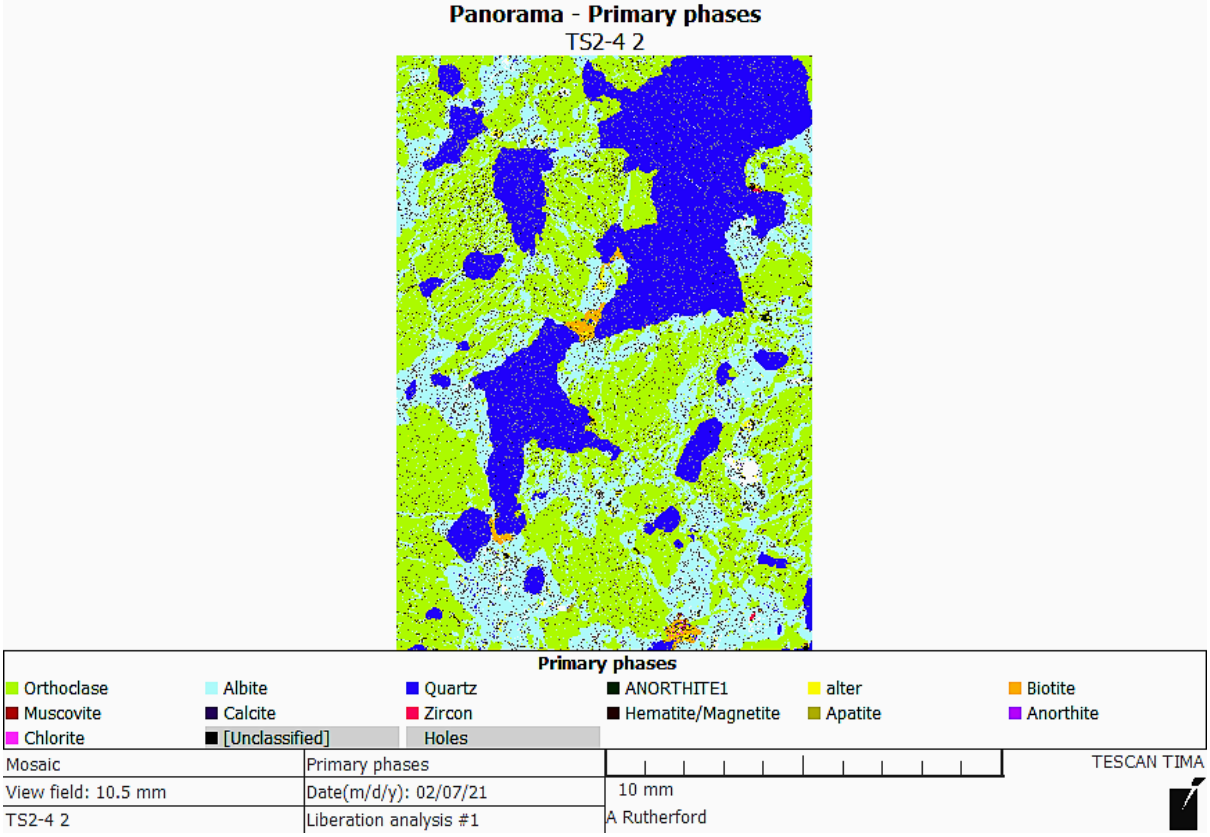
Mineral phase maps studies were done to understand the distribution and proportions of both rock-forming and accessory U-bearing minerals across the sections of both rock samples. TS1 rock sample is dominated by albite, quartz, orthoclase as well as diopside (Figures 4.26 A-B). Whereas, the TS2 rock sample is dominated by orthoclase, albite and quartz (Figures 4.26 C-F). Some of accessory U-bearing minerals observed through these mineral phases include zircon (almost in each and every phase map) and uraninite (Figure 4.26 E). The mineral phase maps (Figures 4.26 A-F) also helped to establish how mineral phases are associated with each other and the types of alteration which include albitisation, chloritisation, kaolinitisation and sericitisation occurring in various rock sample sections. In TS2, all the mineral phase maps show that albite is later than orthoclase. Furthermore, the mineral phase association and alteration analyses also helped to establish the relationship between the rock textural change and the distribution of accessory U-bearing minerals in the sections of both TS1 and TS2 samples.


Panorama - Primary phases
TS1-2 1
Primary phases
Albite
Quartz
Orthoclase
Muscovite
ANORTHITE1
alter
Hematite/Magnetite
Kaolinite
Anorthite
Zircon
[Unclassified]
Holes
Mosaic
Primary phases
TESCAN TIMA
View field: 12.0 mm
Date(m/d/y): 02/06/21
5 mm
TS1-2 1
Liberation analysis #2
A Rutherford

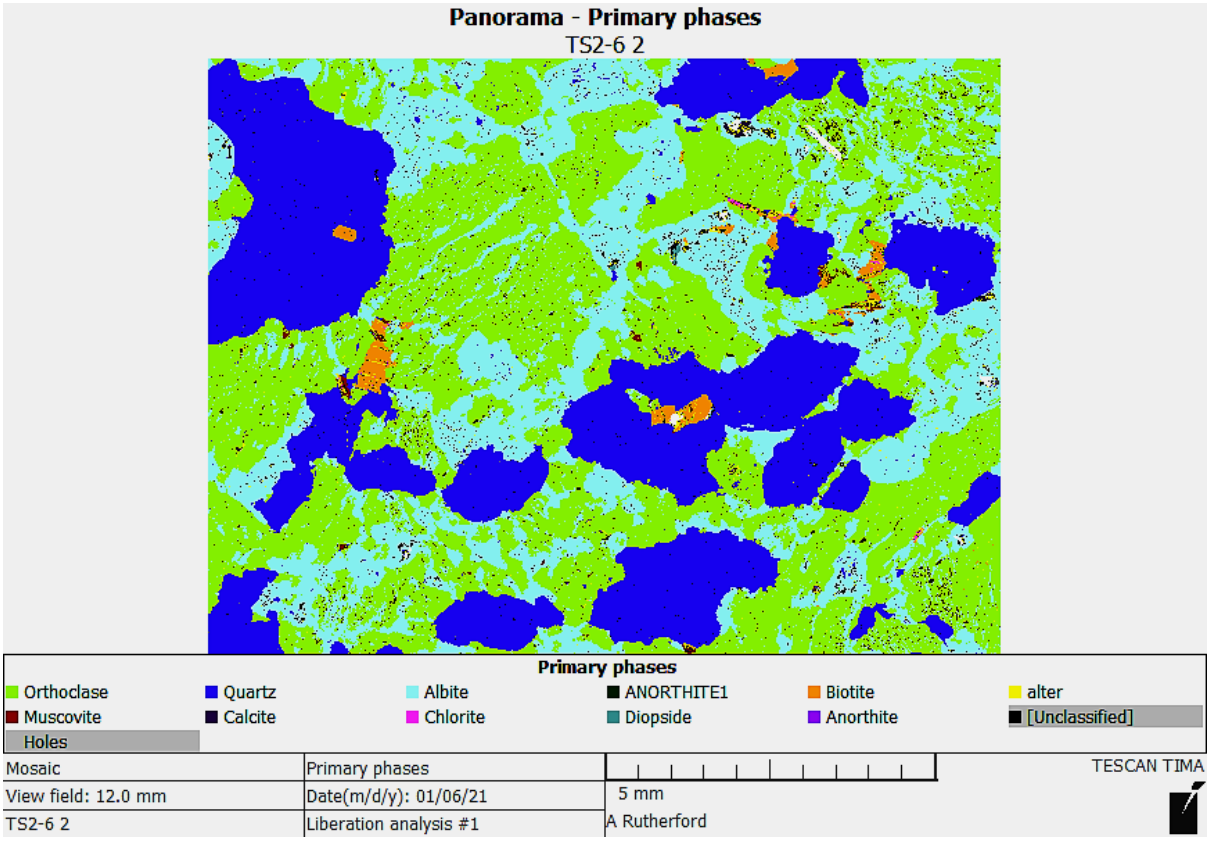
A


Panorama - Primary phases
TS15 1
Primary phases
Quartz
Diopside
Albite
alter
Muscovite
ANORTHITE1
Orthoclase
Anorthite
Kaolinite
Plagioclase
[Unclassified]
Holes
Mosaic
Primary phases
TESCAN TIMA
View field: 10.5 mm
Date(m/d/y): 01/05/21
5 mm
TS15 1
Liberation analysis #1
A Rutherford

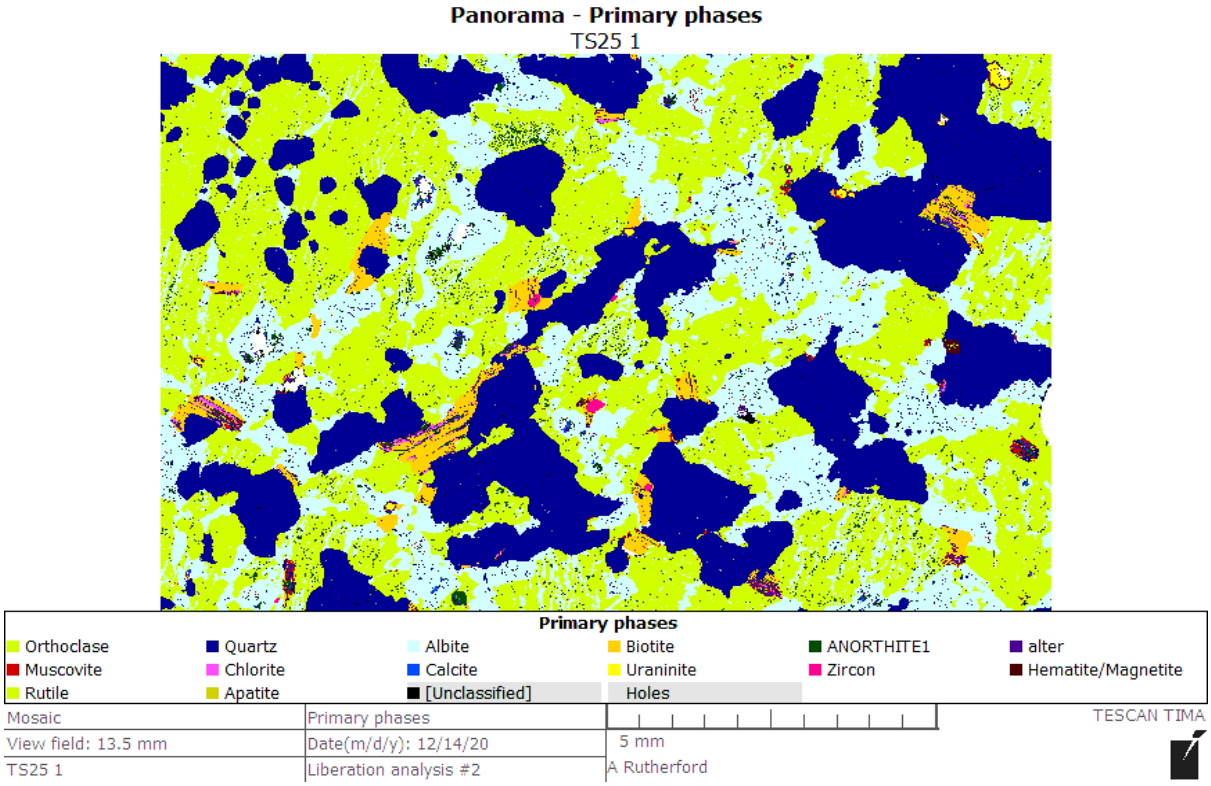
B


Panorama - Primary phases
TS2-4 2
Primary phases
Orthoclase
Albite
Quartz
ANORTHITE1
alter
Biotite
Muscovite
Calcite
Zircon
Hematite/Magnetite
Apatite
Anorthite
Chlorite
[Unclassified]
Holes
Mosaic
Primary phases
TESCAN TIMA
View field: 10.5 mm
Date(m/d/y): 02/07/21
10 mm
TS2-4 2
Liberation analysis #1
A Rutherford

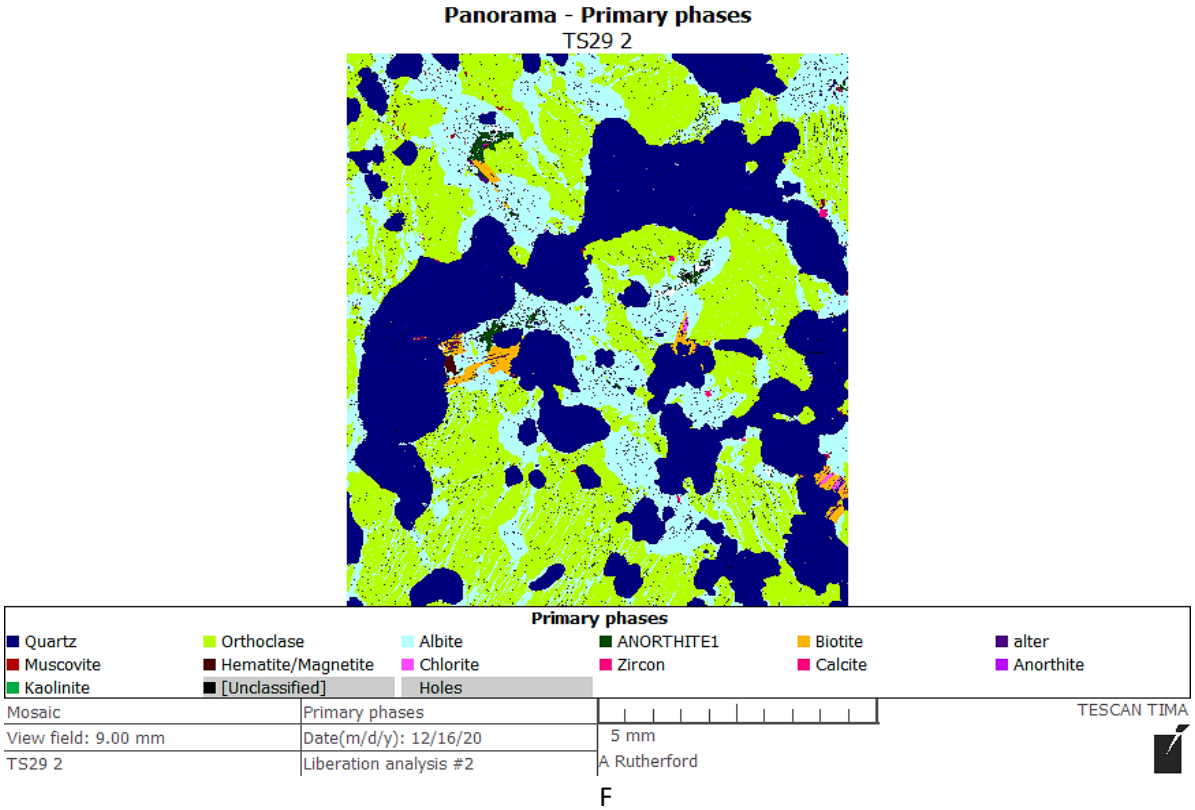
C


Panorama - Primary phases
TS2-6 2
Primary phases
Orthoclase
Quartz
Albite
ANORTHITE1
Biotite
alter
Muscovite
Calcite
Chlorite
Diopside
Anorthite
[Unclassified]
Holes
Mosaic
Primary phases
TESCAN TIMA
View field: 12.0 mm
Date(m/d/y): 01/06/21
5 mm
TS2-6 2
Liberation analysis #1
A Rutherford

D



E



F

Figure 4.26: Mineral phase maps show the distribution of minerals in various thin section domains of various rock sample sections. **(A)** Mineral phase map for TS1 section 3 (TS1-2), **(B)** Mineral phase map for TS1 section 4 (TS1-5), **(C)** Mineral phase map for TS2 section 2 (TS2-4)- the oxidation halo core zone section, **(D)** Mineral phase map for TS2 section 3 (TS2-6)- E-type SLG, **(E)** Mineral phase for TS2 section 4 (TS2-5) and **(F)** Mineral map for TS2 section 5 (TS2-9). Note: More U-bearing minerals are observed in mineral phase map E. In E phase map, uraninite occurs as inclusion in haematite, in mineral grains boundaries and in association with biotite.

4.5.3 Mineral phase proportion results

Mineral phase abundances were determined to show mineral phase proportions occurring in various rock sample sections as presented in Figure 4.27 and Appendix 12. Figure 4.27 shows that TS1 is dominated by albite, quartz and diopside. The accessory minerals found in the D-type SLG sample (TS1) are haematite/magnetite, anorthite, kaolinite, zircon and plagioclase (Appendix 12). Anorthite, albite, quartz and orthoclase are the major rock-forming minerals for the oxidation halo rock sample (TS2) (Appendix 12; Figure 4.27). Accessory minerals found in TS2 are biotite, kaolinite, muscovite, haematite/magnetite, calcite and U-bearing minerals such as zircon, apatite, rutile and uraninite (Appendix 12).

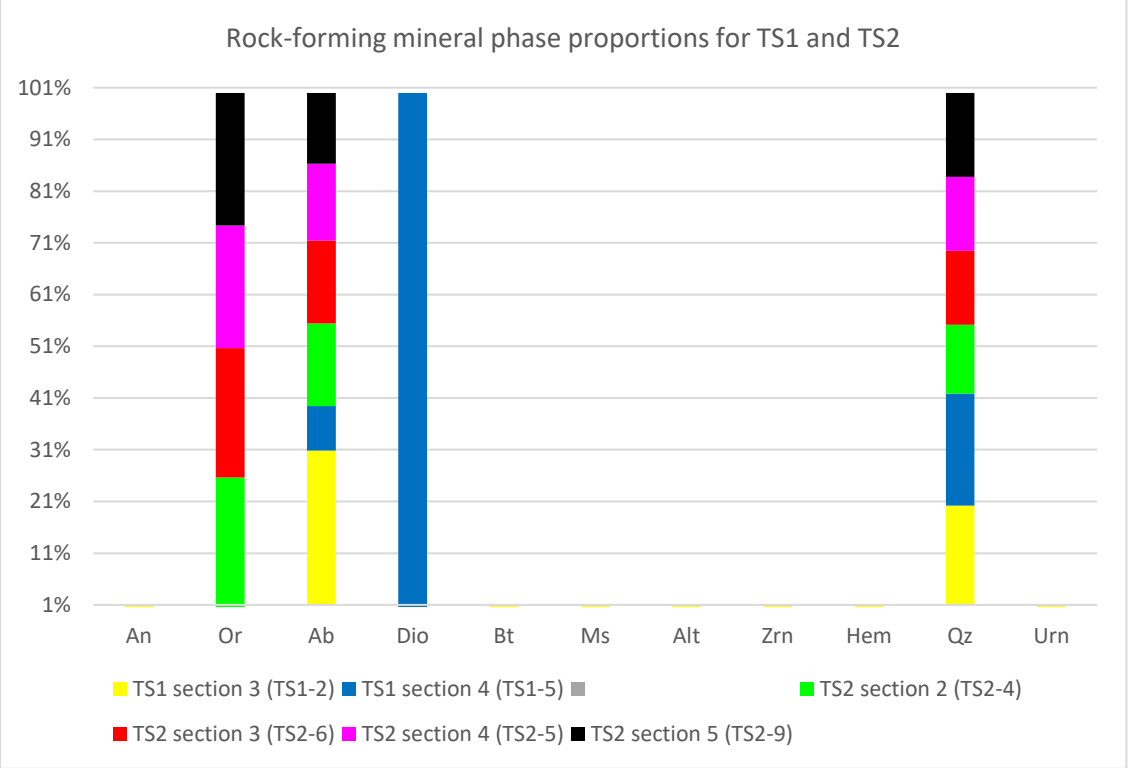


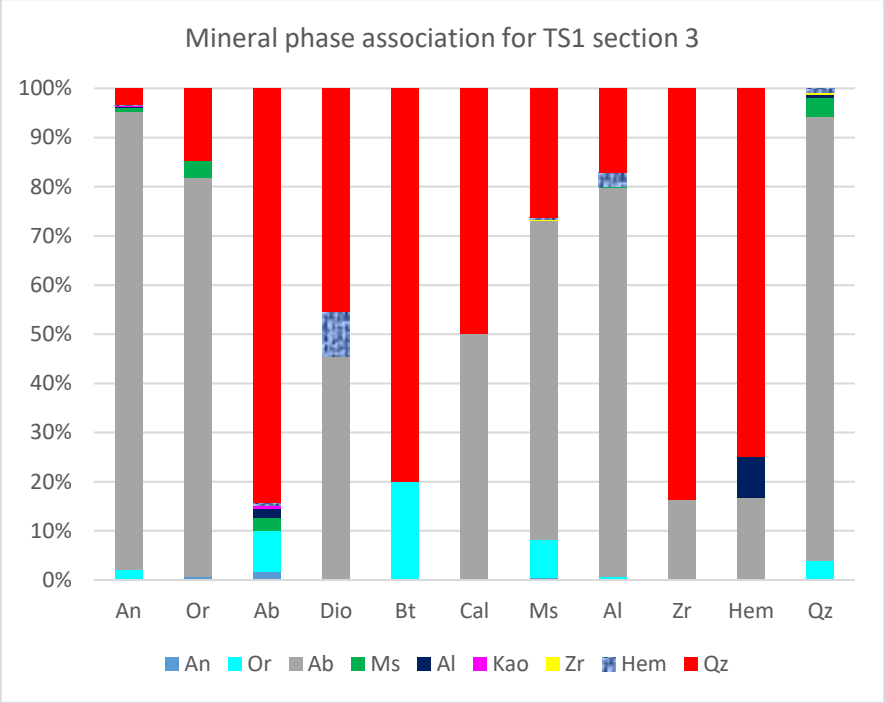
Figure 4.27: A stacked bar graph showing the distribution of major rock-forming mineral phase proportions for both TS1 and TS2 rock samples. Note: An- anorthite, Or- orthoclase, Dio- diopside, Bt- biotite, Ms- muscovite, Alt- alteration, Zrn- zircon, Hem- haematite/magnetite, Qz- quartz, Urn- uraninite. Other accessory minerals detected in low concentration include apatite and rutile in TS2 sections 2 and 5; and calcite, kaolinite and plagioclase in all sections of both TS1 and TS2.

The mineral phase proportion results also show that the proportions of various mineral phases vary with variations in rock texture. For example, quartz proportions (~33%) in TS2 section 5 are highly concentrated compared to TS2 sections 2, 3 and 4 whose proportions are similar (Appendix 12).

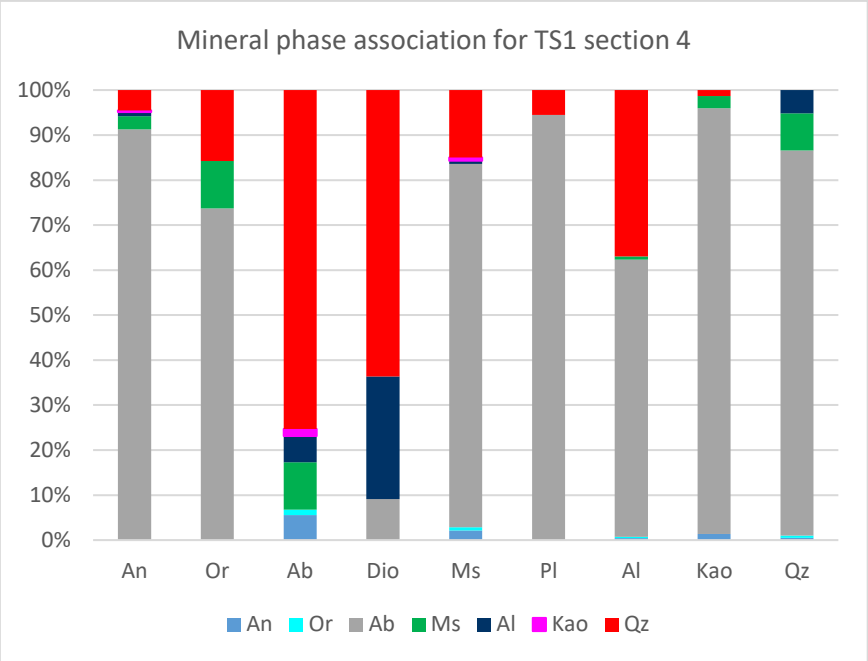
4.5.4 Mineral and alteration phase association

Mineral and alteration phase association analysis was aimed at looking at the effects of textural change on the extent and types of alterations, and how these are related to the distribution of U-bearing minerals in the oxidation halo and their hosting rocks. The analysis was done using TIMA

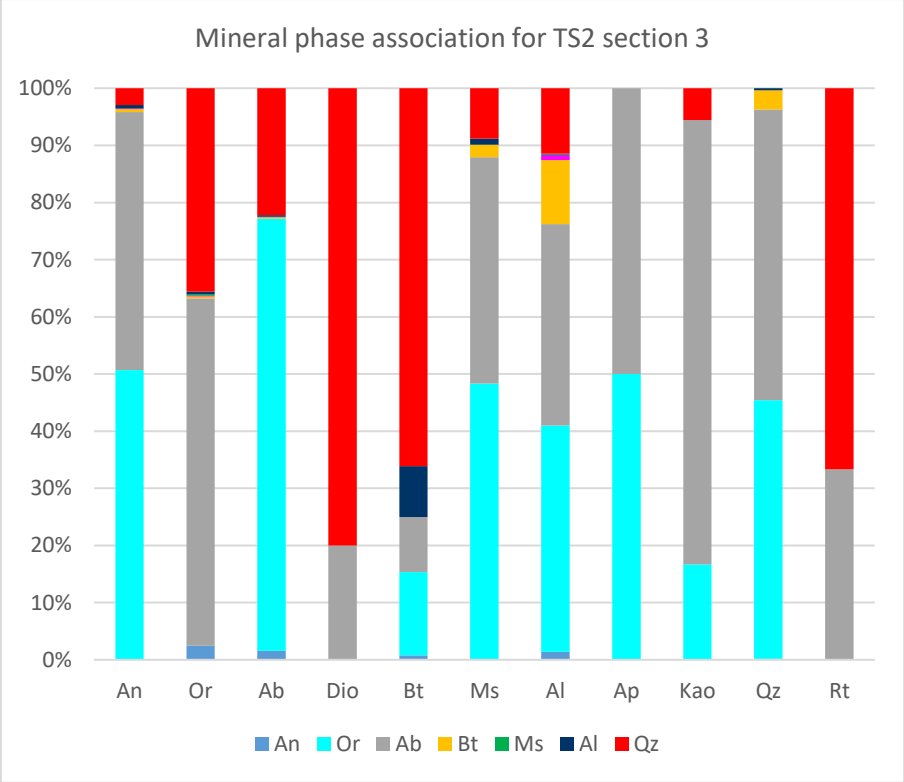
software through the liberation analysis tool (mineral phase association), which enabled the production of the results presented in Figure 4.28.



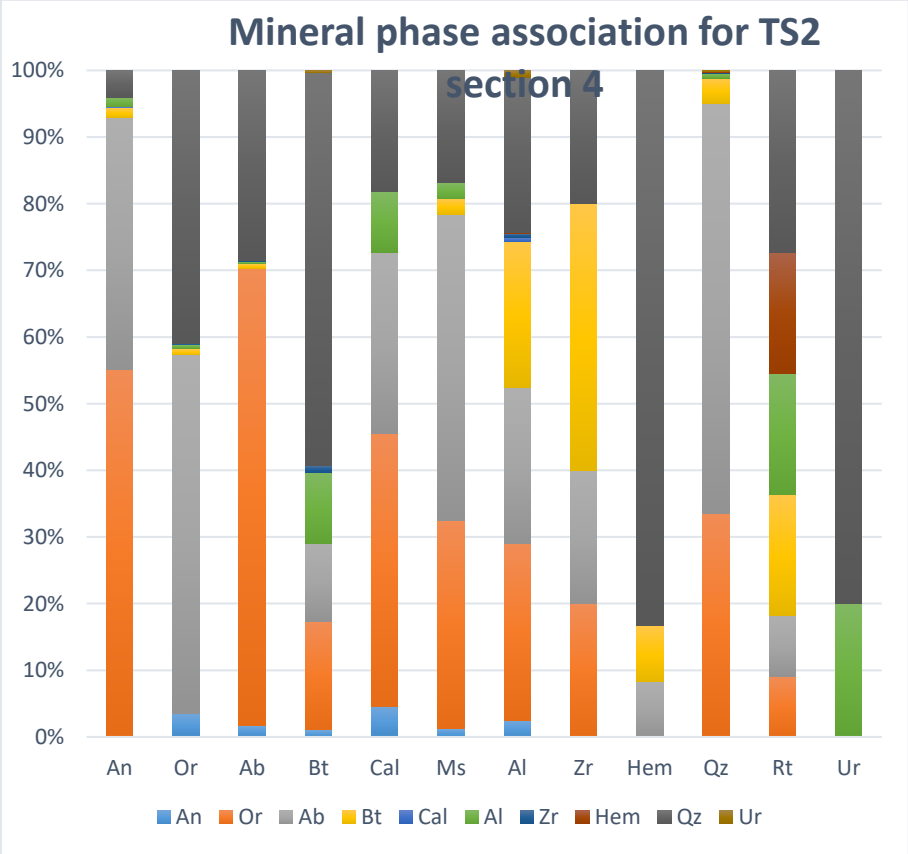
A



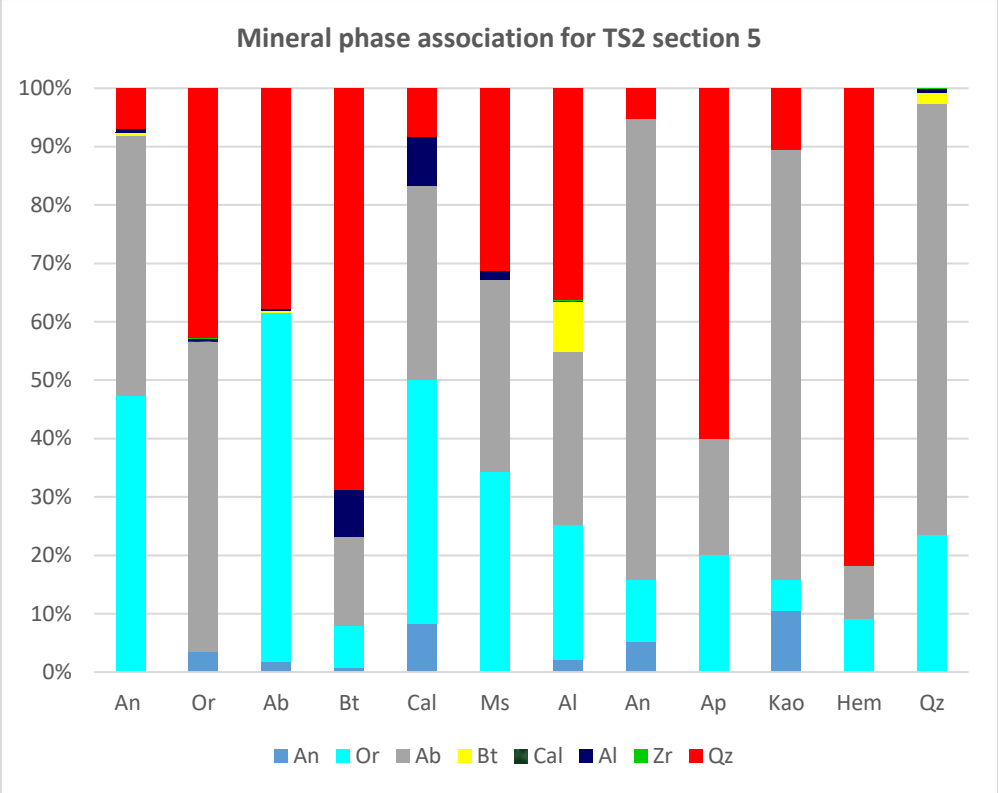
B


Mineral phase association for TS2 section 3
100%
90%
80%
70%
60%
50%
40%
30%
20%
10%
0%
An
Or
Ab
Dio
Bt
Ms
Al
Ap
Kao
Qz
Rt
An
Or
Ab
Bt
Ms
Al
Qz

C


Mineral phase association for TS2 section 4
100%
90%
80%
70%
60%
50%
40%
30%
20%
10%
0%
An
Or
Ab
Bt
Cal
Ms
Al
Zr
Hem
Qz
Rt
Ur
An
Or
Ab
Bt
Cal
Al
Zr
Hem
Qz
Ur

D



E

Figure 4.28: A-B are mineral phase association graphs for TS1 sections 3 and 4, and C-E are mineral phase association graphs for TS2 sections 3, 4 and 5. Note: Ab- Albite, Qz- Quartz, Or- Orthoclase, Ms- Muscovite, Alt- Alteration, An- Anorthite, Hem- Haematite/Magnetite, Zrn- Zircon, Bt- Biotite, Ap- Apatite, Cal- Calcite, Chl- Chlorite, Kao- Kaolinite, Rt- Rutile, Urn- Uraninite, Dio- Diopside.

The mineral phase association results (Figure 4.28) show that mineral and alteration phases vary with textural variation observed across the rock samples. For instance, albite is strongly associated with quartz, orthoclase, alteration and mica in both rock samples. However, in TS1, albite has a strong association with quartz and muscovite, while in TS2; it has a strong association with orthoclase and biotite. Albite in TS2 also shows a high association with zircon compared to TS1. While within the TS2, albite has a high association with zircon in TS2-5 compared to other sections of the oxidation halo

The results further show that the total number of accessory uranium-bearing mineral phases varies from section to section in the oxidation halo. For example, TS2 section 4 has abundant U-bearing minerals such as uraninite and zircon, which are strongly associated with albite, biotite and quartz compared to the TS2 sections 3 and 5. Through the mineral phase association results, some alteration styles occurring in various mineral phases were determined. For example, a high muscovite-albite association observed in TS1 sections 3 and 4 (Figure 4.28 A; B) suggests that albite phases in these sections were subjected to a long period of the sericitisation process, and the albite-kaolinite association indicates that albite also underwent the kaolinitisation process. The strong association between quartz and alteration phases indicates that quartz phases were affected by the effects of the uranium radiation process.

4.5.5 Alteration of mineral phases

Through mineral phase maps and mineral phase segmentation analysis, the following alteration types were determined: albitisation, chloritisation, kaolinitisation and sericitisation. Albitisation is particularly dominant in TS2 compared to TS1. Within TS2, the TS2-5 section is highly albitised compared to other sections, resulting in albite exsolution structures developing over orthoclase (Figure 4.26E; Figure 4.29).

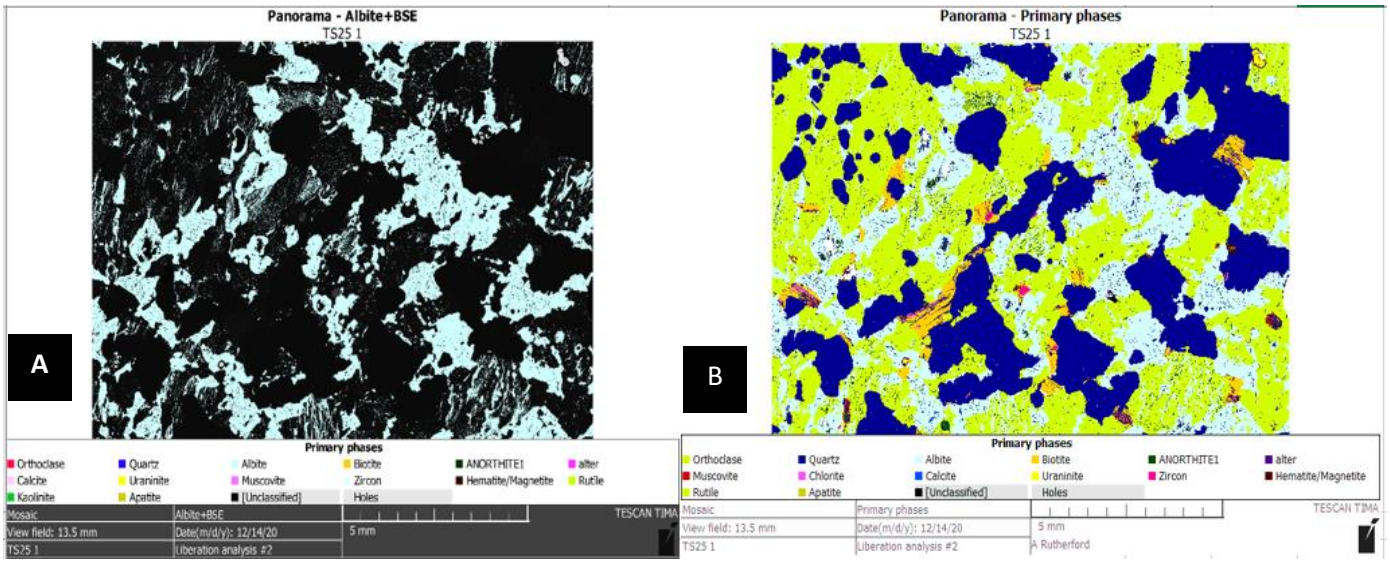
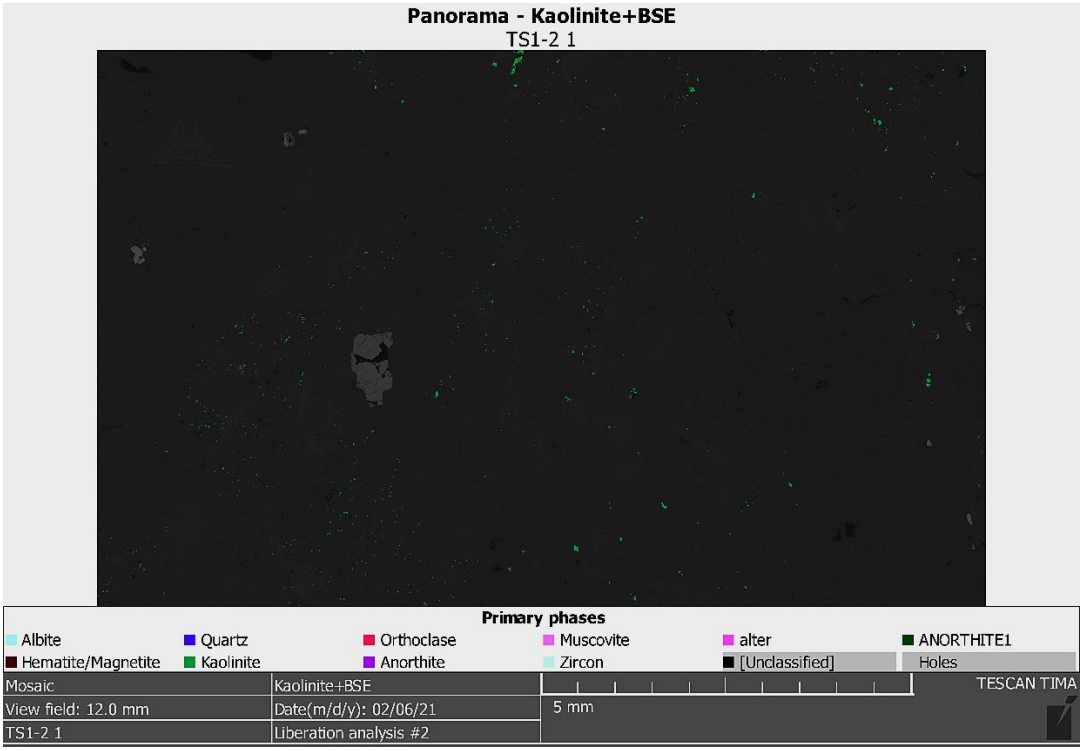


Figure 4.29: Albite segment mineral phase map showing albite exsolution structures. A) Albite phase only and B) Original phase map from which A was derived. Note: Dark mineral phases represent orthoclase and quartz, and orthoclase is being dissolved and replaced by albite.

Chloritisation, mineral phase maps show that chloritisation mainly occurs in the biotite of the TS2-5 section (Figure 4.26E), where biotite is being replaced by chlorite.

Kaolinitisation alteration is characterised by the occurrence of kaolinite in albite. More kaolinite occurs in the albite of the TS1 than TS2. In TS1, kaolinisation is high in the TS1 section 3 (TS1-2), which resulted in the formation of a higher concentration of kaolinite in the section (Figure 4.30A) than the other sections of the same rock sample. The presence of less kaolinite in TS2 section 5 (Figure 4.30B) which is also the case with other rock sample sections indicates that TS2 is less kaolinised.



A

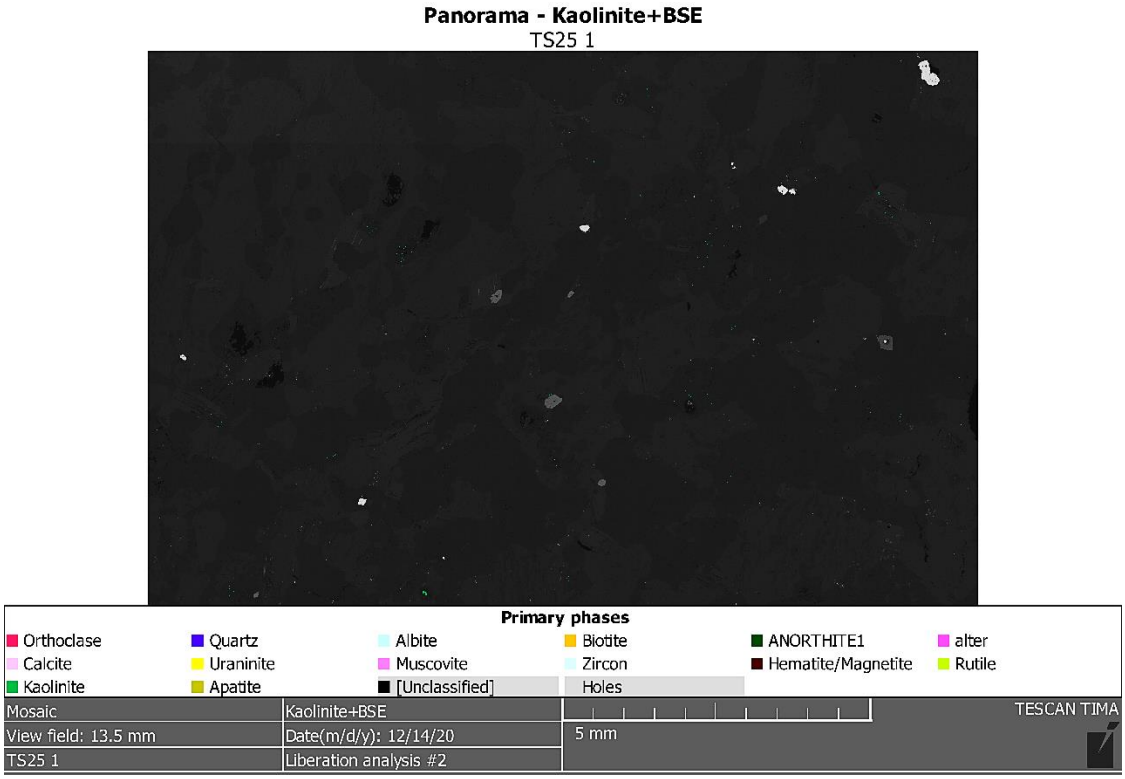
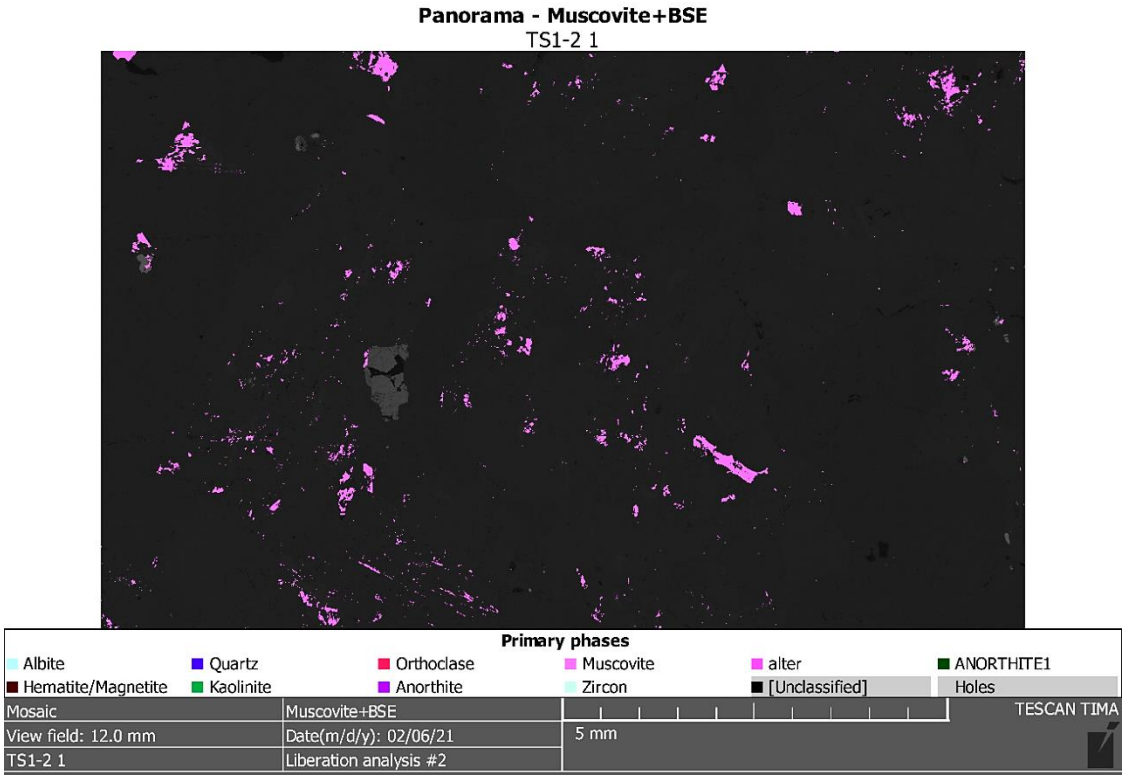
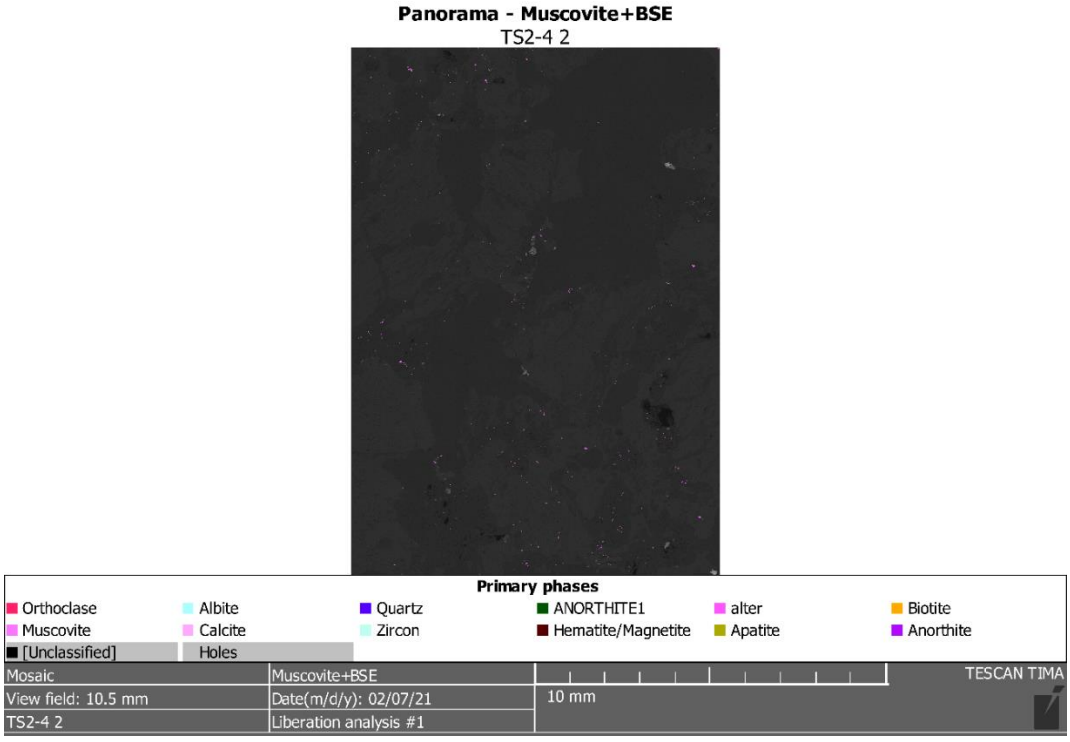


Figure 4.30: Mineral segment phase map for kaolinite showing high kaolinite distribution in TS1 section 3 (TS1-2) (A) and low kaolinite distribution in TS2 section 4 (TS2-5) (B).

The other type of alteration is sericitisation, which is characterised by the development of muscovite associating with albite in both TS1 and TS2 rock samples. The effects of sericitisation alteration are very high in the TS1 compared to TS2. Within TS1, there is a high concentration of muscovite in albite of TS1-2 than TS1-5 (Figure 4.31). In TS2, muscovite is relatively high in sections TS2-4 and TS2-6 compared to TS2-5 and TS2-9.



A



B

Figure 4.31: High muscovite distribution in TS1-2 (A) and low muscovite in low muscovite in TS2-6, indicating high sericitisation of TS1 compared to TS2.

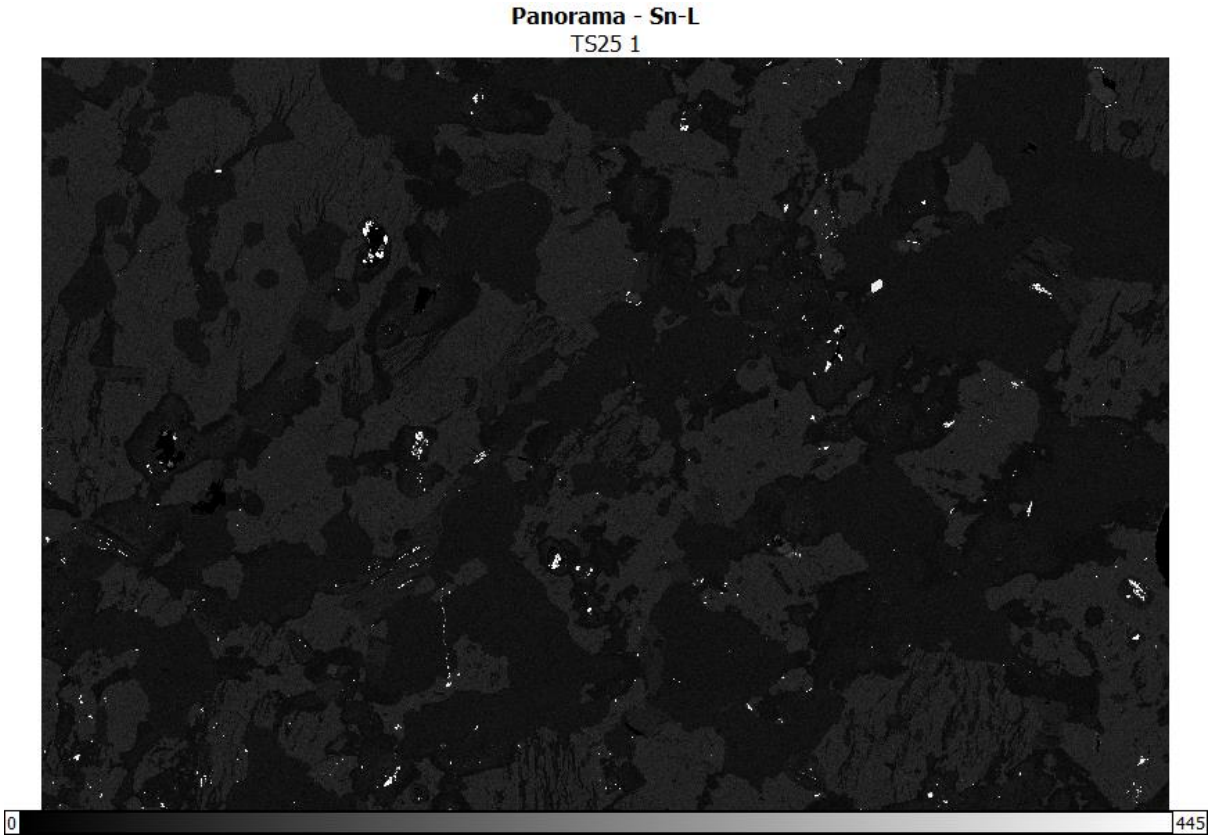
4.5.6 TIMA Element Mapping

Lithophile elements are the major components for granitic rock-forming minerals and associated ore deposits such as uranium, tin and tungsten. TS1 and TS2 rock samples are granitic rocks known for hosting uranium. Many lithophile elements were analysed using elemental maps and mass proportion of the elements (Table 4.5) to understand the chemical composition and distribution of various mineral phases associated with uranium in the rock samples.

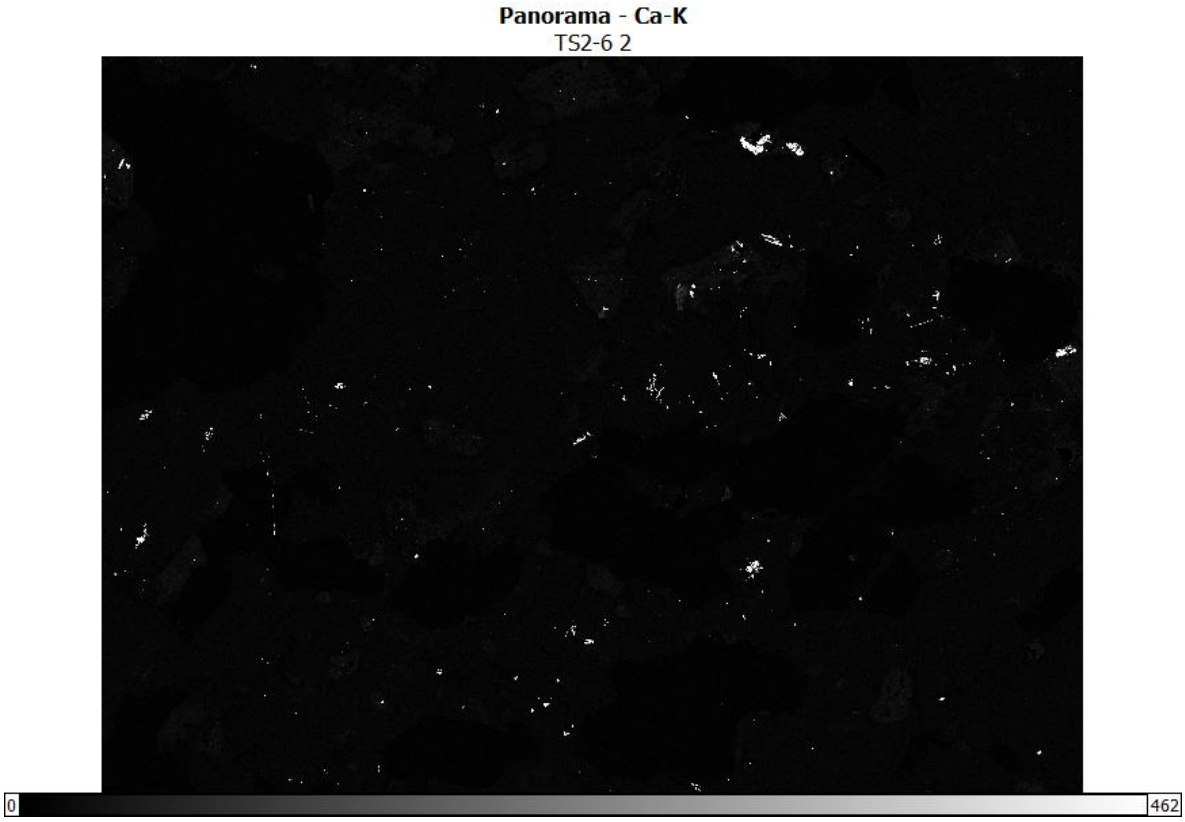
Table 4.5: Proportion of elements in sections of TS1 and TS2 rock samples

Elements	TS1 section 3 (TS1-2)	TS1 section 4 (TS1-5)	TS2 section 2 (TS2-4)	TS2 section 3 (TS2-6)	TS2 section 4 (TS2-5)	TS2 section 5 (TS2-9)
Sodium	9.0	2.4	4.7	4.6	4.4	4.0
Magnesium	0.0	7.3	0.1	0.3	0.8	0.1
Aluminium	12.8	3.6	14.2	13.8	13.4	13.3
Silicon	74.0	65.8	67.1	67.6	67.3	69.1
Potassium	0.8	0.2	11.5	11.1	11.0	11.5
Calcium	0.9	12.4	0.6	0.6	0.6	0.5
Iron	0.6	0.0	0.3	0.2	0.6	0.3
Zirconium	0.1	0.0	0.0	0.0	0.1	0.0
Uranium	0.0	0.0	0.0	0.0	0.2	0.0
Unspecified	1.7	8.1	1.3	1.6	1.3	0.9
Total	100.0	100.0	100.0	100.0	100.0	100.0

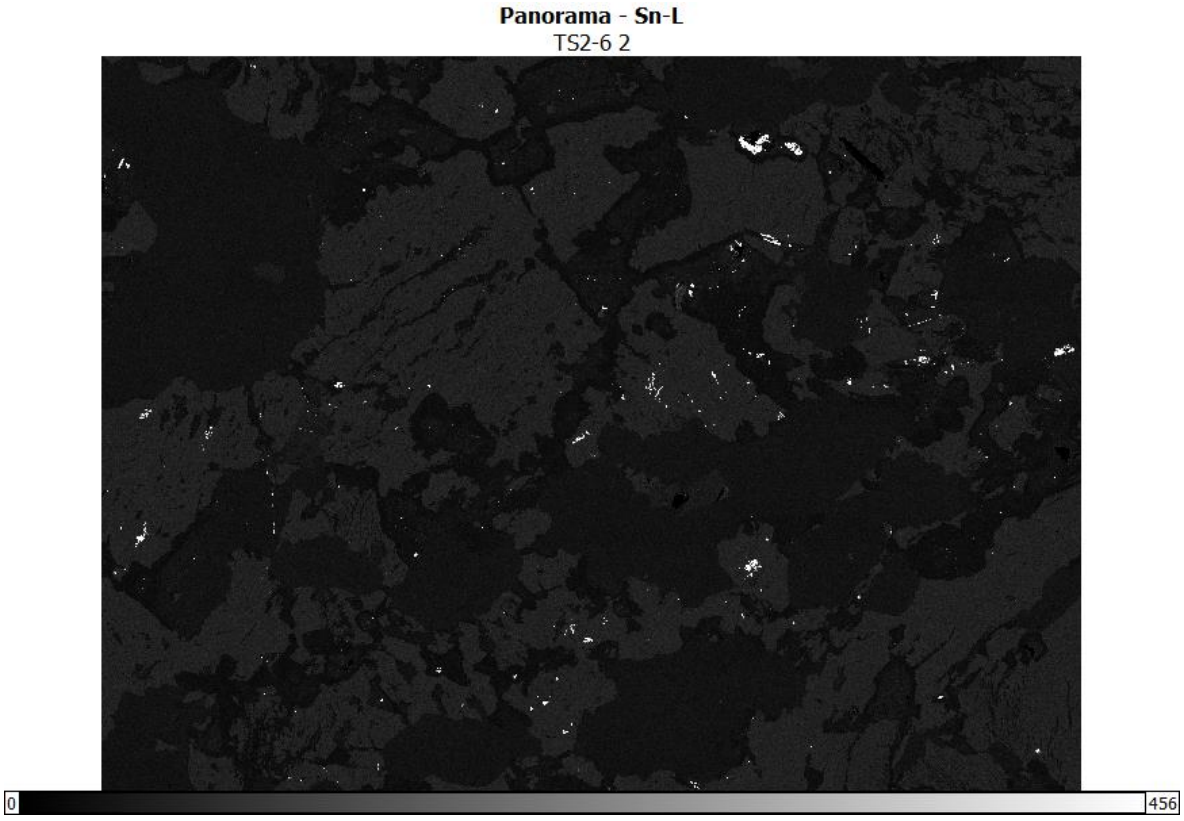
Apart from having a high concentration of major elements for the granite rock-forming minerals, silicon, aluminium, potassium and sodium (Table 4.5), both rock samples also contain iron, calcium, magnesium and uranium-bearing trace minerals (uranium, zirconium, titanium, thorium), yttrium and tin (Sn) which are more concentrated in TS2 compared to TS1. Within the TS2, Sn is highly distributed in TS2 sections 4 (TS2-5) and 5 (TS2-6) (Figures 4.32A), and it is closely associated with calcium (Figure 4.32B; C). The presence of abundant Sn in TS2 rock suggests that oxidation halo sample might be associated with cassiterite that formed through the geochemical evolution of Na-Ta-Sn oxides (Fuchsloch et al., 2019).



A



B

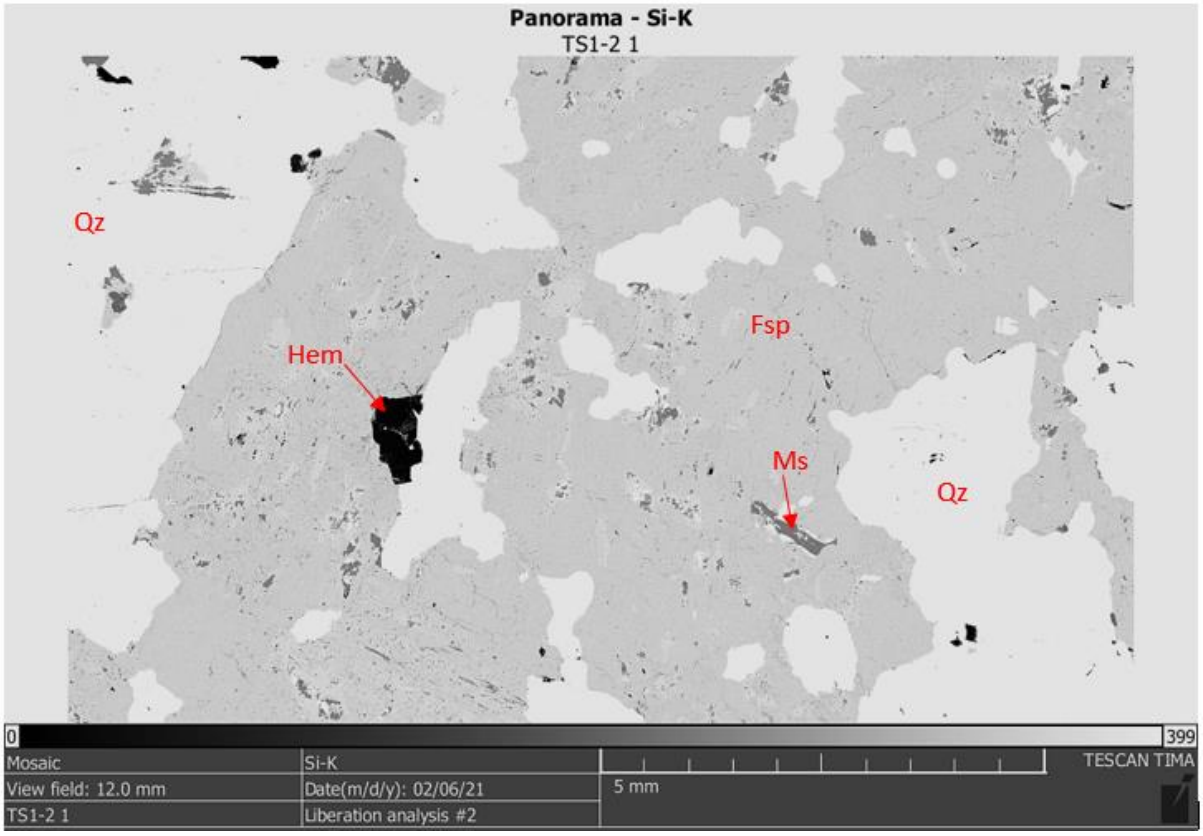


C

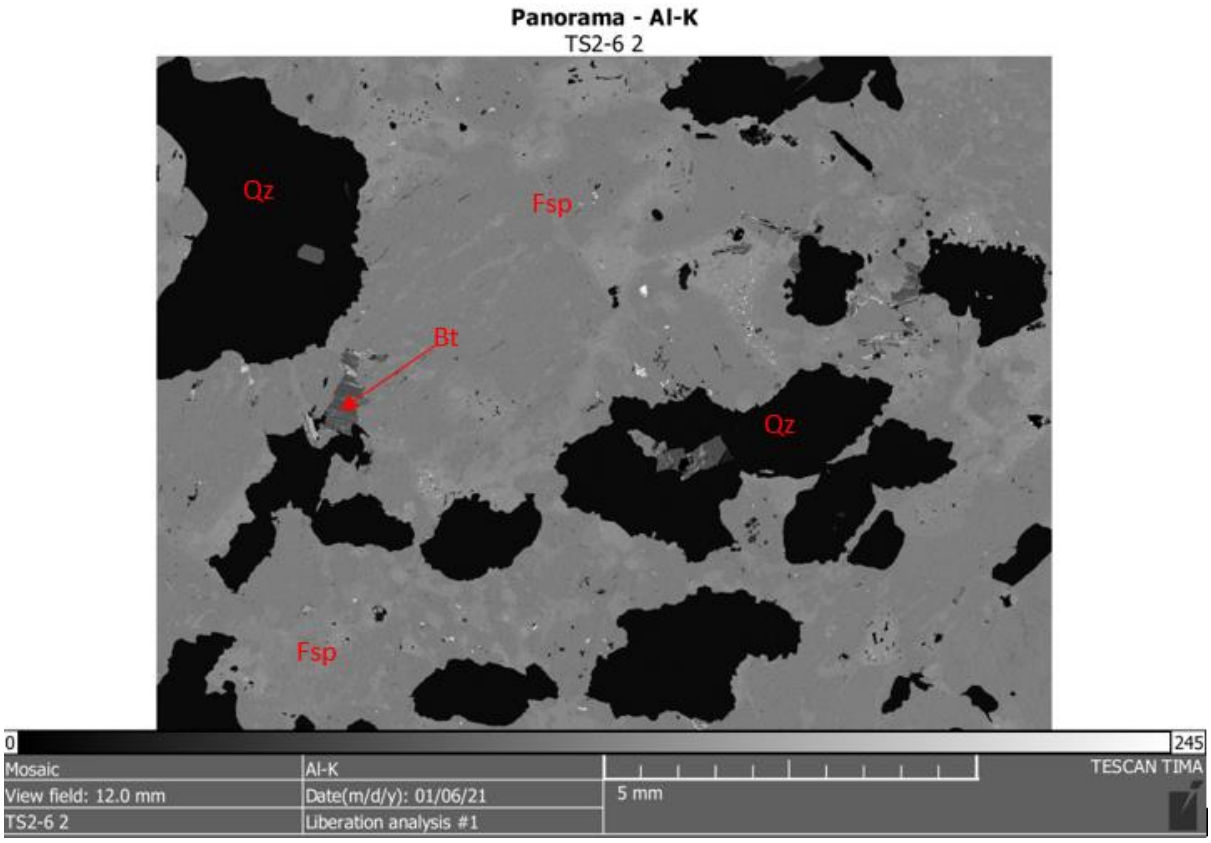
Figure 4.32: Elemental maps showing tin distribution in a TS2 rock sample. A) TS2-5 shows a high occurrence of tin TS2 section 4, while B and C show that tin is high in domains of the thin section having high concentration calcium. Note: Bright phases represent calcium and tin.

High levels of silicon, aluminium, potassium, and sodium signify the occurrence of quartz (SiO_4), plagioclase (Na, Ca) (Si, Al)$_4O_8$), and alkali feldspar ((K, Na) $AlSi_3O_8$) in granites such as the SLGs (Table 4.5). Based on the elemental and mineral phases maps, silicon represents quartz occurrences (Figure 4.33A), aluminium for feldspar (Figure 4.21B), sodium for albite ($NaAlSi_3O_8$) (Figure 4.33C), potassium for orthoclase (**KA**lSi_3O_8) (Figure 4.33D), potassium, iron, and magnesium for biotite (K (**Mg**, **Fe**) $_3(AlSi_3O_{10})$ (F, $OH)_2$,) iron for haematite/magnetite (**Fe**$_2O_3$/**Fe**$_3H_2O_4$) (Figures 3A) and magnesium and calcium for diopside (**MgCa**Si_2O_6). The high concentration of magnesium and calcium in TS1-5 (Table 4.5) is due to the presence of a high diopside found in the section (Figure 4.27), which according to Freemantle (2015) formed through de-carbonisation reaction ($CaCO_3$ + SiO2= $CaSiO_3$ (diopside, skarns) + CO_2). Fe (haematite/magnetite) distribution in TS2 is high within the oxidation halo than the E-type section (Table 4.5).

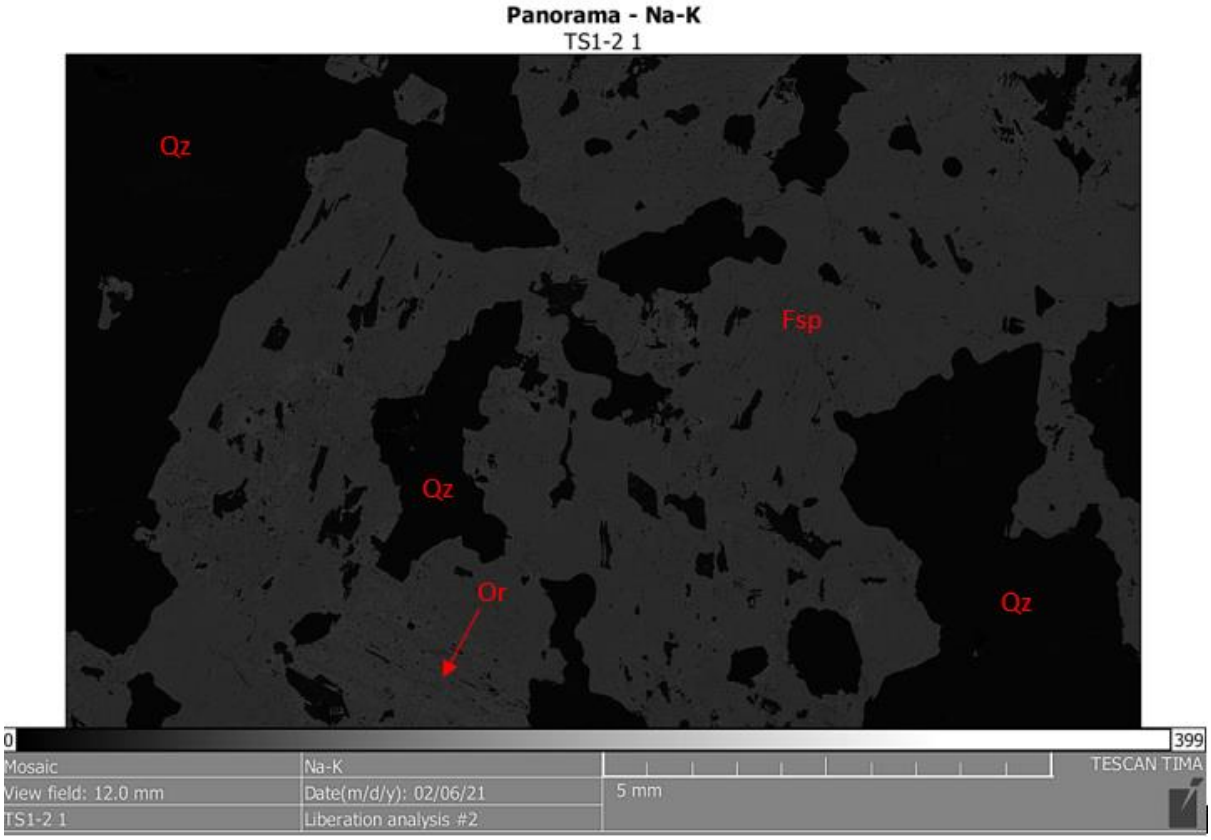
In terms of the distribution of uranium-bearing trace elements such as uranium, zircon and titanium in the TS2, the elemental maps show that these elements are highly distributed in the oxidation halo transition zones (Figure 4.25, Figure 4.33E and Table 4.5).


Panorama - Si-K
TS1-2 1
Qz
Hem
Fsp
Ms
Qz
0
399
Mosaic
Si-K
TESCAN TIMA
View field: 12.0 mm
Date(m/d/y): 02/06/21
5 mm
TS1-2 1
Liberation analysis #2

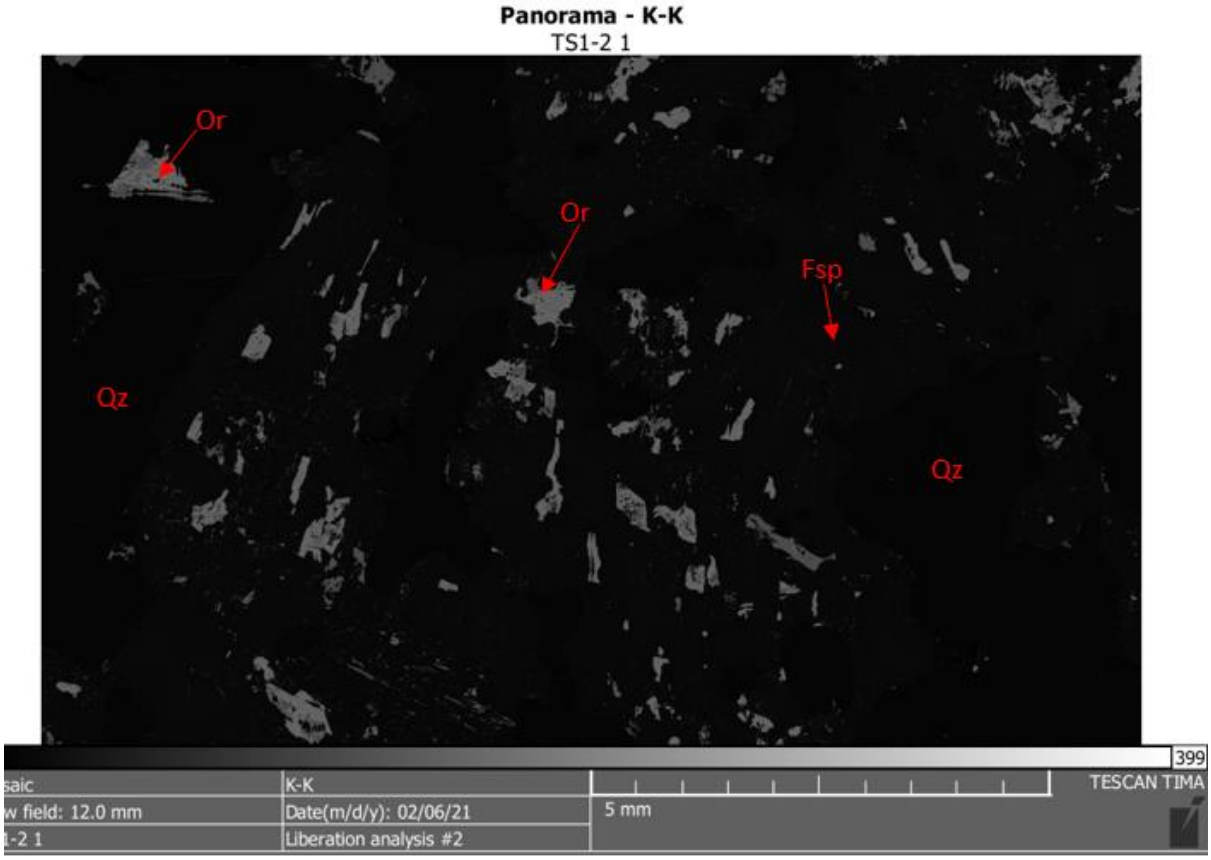
A


Panorama - Al-K
TS2-6 2
Qz
Fsp
Bt
Qz
Fsp
0
245
Mosaic
Al-K
TESCAN TIMA
View field: 12.0 mm
Date(m/d/y): 01/06/21
5 mm
TS2-6 2
Liberation analysis #1

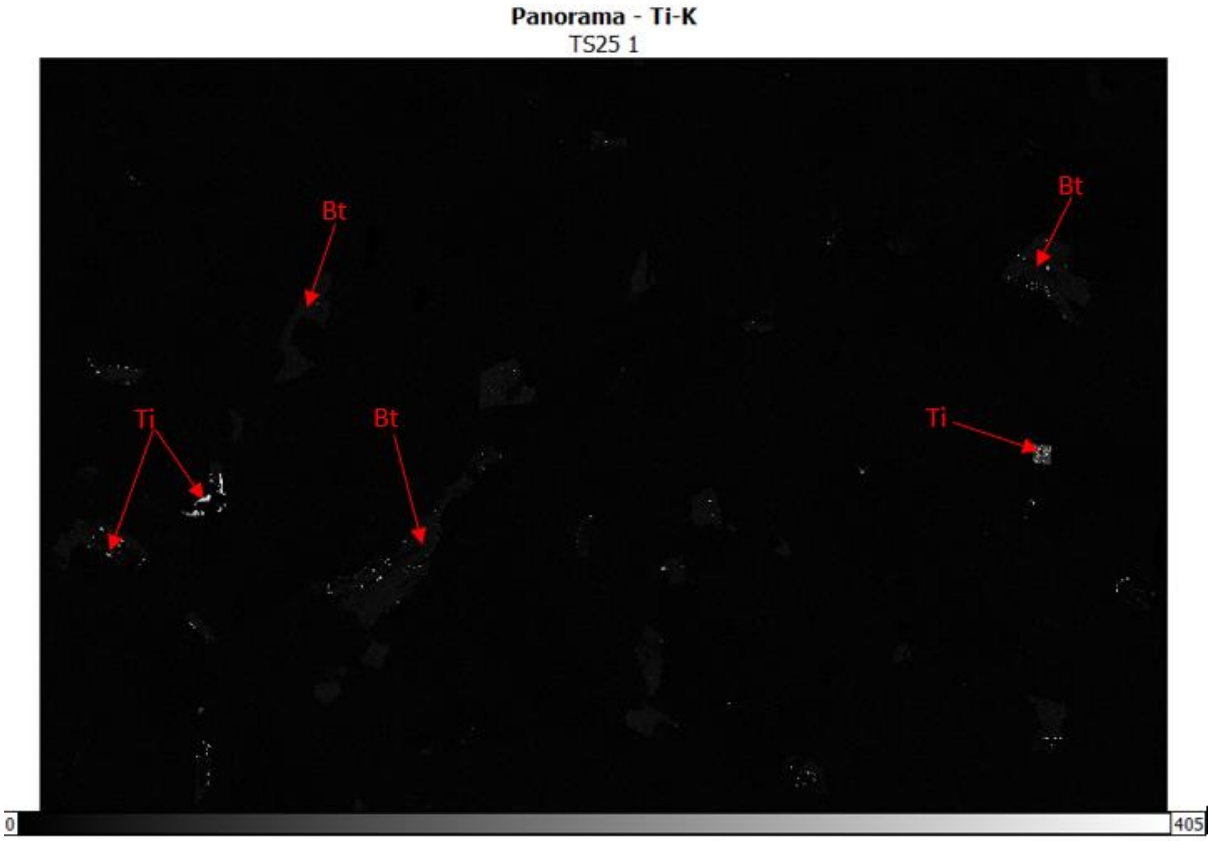
B


Panorama - Na-K
TS1-2 1
Qz
Fsp
Qz
Or
Qz
0
399
Mosaic
Na-K
TESCAN TIMA
View field: 12.0 mm
Date(m/d/y): 02/06/21
5 mm
TS1-2 1
Liberation analysis #2

C


Panorama - K-K
TS1-2 1
Or
Or
Fsp
Qz
Qz
399
K-K
TESCAN TIMA
Date(m/d/y): 02/06/21
5 mm
Liberation analysis #2

D



E

Figure 4.33: Elemental maps for Si (quartz), Al (feldspar), K (orthoclase), Na (albite), Fe (haematite/magnetite) and Ti (titanite). A) Silicon (bright phase) and iron (dark phase) elemental map from TS1 section (TS1-2), B) Aluminium elemental map from TS2 section 3 (TS2-6), C) Sodium elemental map from TS1 section 3 (TS1-2), D) Potassium elemental map from TS1 section 3, E) Ti elemental map from TS2 section 4 (TS2-5). Note: Elements in various thin section domains are represented by bright phases.

4.6 Summary of the results

The results discussed above include mineralogy, rock colour variation and alterations and textural features.

4.6.1 Mineralogy

Mineralogically, hand specimen observations, micro-RXF, thin section petrography and TIMA results show that the TS1 rock sample is dominated by albite, smoky quartz, orthoclase and diopside. Muscovite, biotite, anorthite, haematite, kaolinite and U-bearing minerals (uranophane and zircon) are some of the major accessory minerals observed in the D-type SLG sample (TS1). For the TS2 rock sample, the results show that the rock-forming minerals dominating the sample are albite, anorthite, orthoclase and quartz. TS2 has similar types of accessory minerals observed in TS1, but it also has apatite, rutile and titanite accessory minerals mainly occurring in the TS2 section 4.

Through BSE images, five mineral phases were determined for both rock samples which include the black phases representing unclassified mineral phases, the deep-dark grey phase for albite and quartz, the grey phase for orthoclase and biotite, the bright phase for haematite/magnetite and zircon and the very bright phases for uraninite.

4.6.2 Rock colour change and alterations

TS1 rock sample dominantly looks light, but its appearance varies from light to dark across the rock sample. The light-dark variation is a result of the differences in albite and smoky quartz abundances. TS1 sections 1,3, 4, and 6 with high smoky quartz abundances are darker than TS1 sections 2 and 5 which have lesser smoky quartz. The colour for TS2 varies from light to red to pink when moving from the D-type (light) to E-type (pink) granite through the oxidation halo (red) which is determined by the high occurrence of haematite/magnetite. In the oxidation halo transition zones with a high concentration of haematite/magnetite, a deep red colouration is observed. This colouration becomes less intense away from the alteration contact zone.

In terms of alteration, both TS1 and TS2 rock samples experienced uranium radiation, metamictisation, sericitisation, chloritisation, kaolinisation and albitisation. Uranium radiation and metamictisation alterations are common in albite-quartz contact zones, while sericitisation and kaolinitisation are dominant in albite of TS1. Chloritisation and albitisation are very prominent in the oxidation halo transitional zones.

4.6.3 Mineral grain size distribution and structures

In TS2, the >10 mm grain sizes dominate TS2 sections 1 and 2, while the 5-10 mm and the 2-5 mm grain sizes are the dominant mineral grains sizes for TS2 section 3, TS2 sections 4 and 5, respectively. While in TS1, TS1 sections 1, 3, and 6 are dominated by 2-5 mm mineral grain sizes, TS1 sections 2 and 5 with >10 mm, and TS1 section 4 contains 5-10 mm modal mineral grain sizes.

Quartz chains and clusters, intergrowth relationship between minerals, and embayment contact boundaries between albite and quartz are the primary structures observed in both TS1 and TS2 rock samples. TS2 also has myrmekite structures observed in plagioclase only and albite exsolution lamellae structures developing over microcline.

CHAPTER FIVE

DISCUSSION OF RESULTS

5.1 Introduction

The principal aim of this research is to interpret the petrological characteristics of the mineralised oxidation halo, as compared to the host rocks, of granite-hosted, uranium-bearing rocks from Rössing Mine and Goanikontes uranium deposit. The research objectives are to describe and document the texture and mineralogy, and the distribution of uranium minerals in relation to the oxidation halos and their hosting rocks. This chapter discusses the results presented in chapter four to address the research objectives. It also highlights the correctness, validity and importance of the research findings.

5.2 Textural and structural features of the D-type SLG (TS1) and E-type SLG (TS2)

Previous studies by Nex (1997) and Kinnaird and Nex (2007) reported textural variations across the oxidation halos. Freemantle (2015) noted the same by pointing out that large feldspar spans the oxidation halo, where only part of the feldspar contains the characteristic Fe-staining. Though past researchers reported about the textural change of the oxidation halos, less detailed information was provided on the texture types and how the texture varies across the oxidation halo. The current research results also show that indeed there is a textural change in the oxidation halos and their hosting rocks, but the texture changes include grain size variations from fine to pegmatitic.

For the D-type SLG (TS1) sample, the hand specimen (Appendix 5; Figure 4.1) and thin section (Appendix 9; Figure 4.17) mineral grain sizes results show that the TS1 sections 1,3 and 6 have a fine texture for they are dominated by the medium-grained textured minerals. TS1 sections 2 and 5 have pegmatitic texture since their modal mineral grain sizes are pegmatitic, whereas, TS1 section 4 has a coarse texture for it is dominated by the coarse-grained minerals. In the E-type SLG (TS2) sample, the mineral grain size results determined through hand specimen observations (Appendix 5; Figure 4.2), the µ-XRF (Appendix 7; Figure 4.12) and the thin section (Appendix 11; Figure 4.23) show that the D-type section and oxidation halo core zone have a pegmatitic texture for they are dominated by pegmatitic mineral grain sizes. TS2 section 3 (E-type) has a coarse texture as it is dominated by the coarse-grained textured minerals, whereas, the oxidation halo transitional zones have a fine texture for they have medium-grained textured as their modal mineral grain sizes.

In terms of structural features, the results show that both the D-type SLG and E-type SLG samples have quartz chains and quartz clusters as common structural features. Other types of structural features dominating the E-type SLG sample are albite exsolution textures developing over microcline phases and the myrmekites occurring within the plagioclase. Myrmekites occur in all sections of the oxidation halo, and they are commonly observed in the oxidation halo transitional zones. According to Freemantle (2015), one of the common features for the majority of the mineralised SLGs is the development of myrmekites within plagioclase. On the other hand, myrmekite growth at the plagioclase rim is a common feature for unmineralised SLGs. The occurrence of myrmekites within the plagioclase in the oxidation halo is an indication that the oxidation halos at the Rössing Mine have high uranium mineralisation. This explanation agrees with what Nex (1997) and Kinnaird and Nex (2007) reported that the oxidation halos at the Rössing Mine have high uranium mineralisation, which have been being mined for uranium since the opening of the Rössing Mine in 1976. The

current results also show that in the TS2 rock sample, a high distribution of accessory U-bearing minerals occurs in the oxidation halo, with the transitional zones having the highest uranium distribution.

5.3 Mineral composition, U-bearing minerals distribution and colour variation

The mineralogy results established through the hand specimen observations (Table 4.1), the thin section observations (Table 4.2) and the TIMA studies (Appendix 12; Figure 4.26 A-B; Figure 4.27) show that the major rock-forming minerals for the TS2 are albite, diopside and quartz. TS1 has also accessory minerals which include anorthite, biotite, haematite/magnetite, muscovite, kaolinite and U-bearing minerals (uranophane, uraninite and zircon). For the TS2, the hand specimen observations, the µ-XRF results (Figure 4.13), the thin sections observations (Table 4.3) and TIMA results (Appendix 12; Figures 4.25; 26C-F; 27; 32; 33) indicate that the major rock-forming minerals dominating the rock sample are anorthite, albite, quartz and orthoclase. Accessory minerals observed in the sample are diopside, muscovite, anorthite, haematite/magnetite, tin, biotite and U-bearing minerals (uraninite, uranophane, zircon, apatite, rutile and titanite). Uranophane and zircon are the most abundant U-bearing minerals observed in both rock samples.

According to Freemantle (2015), the mafic rock-forming mineral diopside in the SLGs formed due to the de-carbonisation process when the alaskites were intruding the boundary of the Khan-Rössing Formations and were forced to crystallise below the marbles of the Rössing Formations. Marbles acted as the reducing agent to reduce and precipitate the dissolved uranium metals from the melt. Therefore, the presence of diopside in the oxidation halos and hosting rocks is a good indicator that these granites have high uranium mineralisation, as they formed within the REDOX boundaries, the favourable environments for uranium mineralisation. Freemantle (2015) also noted that most of the mineralised SLGs in the Damaran southern Central Zone have a high concentration of anorthite. The µ-XRF and mineral phase proportions (TIMA) results show that all sections of the oxidation halo sample (Appendix 12; Ca elemental map distribution in Figure 4.12) have a high occurrence of anorthite phases. This also signifies that the oxidation halos have indeed high uranium mineralisation as noted by Freemantle (2015).

Hand specimen observations show that both rock samples exhibit colour variations, with the D-type SLG sample showing a light-dark appearance (Figure 4.3) and the light-red-pink colouration for the oxidation halo sample (Figure 4.6). The light-dark colouration of the TS1 is mainly caused by the unequal distribution of smoky quartz as well as biotite in the sample. The sections with a high concentration of smoky quartz such as the TS1 sections 3 and 4 have a dark appearance unlike the TS1 sections 2 and 5 with less concentration of smoky quartz (Figure 4.3). The occurrence of biotite in association with smoky quartz makes the TS1 section 4 having dark (biotite and smoky quartz) and light (plagioclase and colourless quartz) layers (Figure 4.4). The light-red-pink colouration in TS2 sample is a result of unequal distribution of iron oxide (haematite) across the rock sample, which also defines the boundary of the oxidation halo as shown by the hand specimen observations (Figure 4.9), the Fe elemental map (Figure 4.13) and the thin section results (Figures 4.20; 24). Within the oxidation halo, the TS2 section 4 has a deep red colouration compared to other sections. A deep red colouration in this section is a result of the high distribution of biotite, which through thin section petrography show that biotite is strongly altered and it is associated with abundant iron oxides such as haematite (Figures 4.19; 21A; 22).

In terms of the distribution and occurrence of U-bearing minerals in oxidation halos and their hosting rocks, the mineralogy results show that most of these minerals occur in the feldspar-quartz contact zones, radiating fractures, feldspar cleavages and fractures, less in quartz fractures, and also in association with the highly chloritised biotite. The distribution of accessory U-bearing minerals varies with the textural variations as observed in both rock samples. Most of these minerals occur abundantly in the fine-textured sections compared to the pegmatitic sections. In the D-type SLG (TS1), abundant U-bearing minerals occur in the fine-textured TS1 sections 1, 3 and 6, but also in the coarse-textured TS1 section 4. For the oxidation halo sample (TS2), more U-bearing minerals are observed in the finely textured oxidation halo transitional zones, with TS2 section 4 having the highest occurrence of these minerals compared to the pegmatitic textured TS2 section 1 (D-type) and TS2 section 2 (oxidation halo core zone) and the coarse-textured TS2 section 3 (E-type). In both rock samples, the sections with a high occurrence of U-bearing minerals have also a high concentration of smoky quartz as observed in the hand specimen. This observation is in line with Nex (1997) and Kinnaird and Nex (2007) reported about the high concentration of smoky quartz in the D-type and E-type SLGs signifies that these granites have high uranium mineralisation.

This research has further established that U-bearing minerals in the oxidation halos and their hosting rocks are unevenly distributed depending on textural variations.

5.4 Oxidation halo formation and uranium mineralisation, alteration styles and distribution of U-bearing minerals

Oxidation halos are interpreted to have formed as a result of late magmatic-hydrothermal alteration (Nex, 1997; Corner and Henthorn, 1978; Freemantle; 2015). These alteration events formed the oxidation fronts as Fe-enriched minerals were altered forming the Fe-oxides minerals characterising the oxidation halo by defining its boundary (Figures 4.9; elemental maps for Fe, Mn, Ti in Figure 4.13; Figure 4.20; Figure 4.24). The thin section observation, micro-XRF and TIMA results show that within the oxidation halo transitional zones; there is high occurrence of uranium-bearing and iron oxide minerals occurring in association with altered biotite. Since sulphide minerals have not been identified in the oxidation halo and their hosting rocks in this study, this implies that uranium mineralisation in the oxidation halo was accompanied by iron oxide minerals, which provided an important source of Fe^{2+} to the REDOX system to reduce the dissolved uranium metals. In the process of oxidising Fe^{2+} to reduce and deposit dissolved uranium metals, more iron oxide minerals formed in the oxidation halos as by-products. Based on the results, the source of Fe^{2+} to the REDOX system were the biotite phases, which occur abundantly in the oxidation halo transitional zones. This observation agrees with Freemantle's (2015) suggestion on uranium mineralisation that biotite was in variable equilibrium with the melt, and it might have provided an important source of Fe to the REDOX system as a result of alteration. Biotite is also high in the country rocks the mineralised SLGs intruded, the pyroxene-hornblende gneiss and biotite-amphibole schist units and biotite-amphibole schist and biotite-cordierite gneiss (Basson and Greenway, 2004). The inclusion of uraninite in magnetite (Figures 4.25; 26E) also indicates that magnetite was one of the minerals which provided Fe^{2+} to the REDOX system for uranium mineralisation.

The alteration results show that both rock samples were affected by several alteration events, including albitisation, haematisation, chloritisation, kaolinisation, sericitisation, metamictisation and uranium radiation. These alteration styles were a result of the formation of the oxidation halos (albitisation and haematisation), further alteration of the oxidation halos (sericitisation, kaolinisation and chloritisation), and the effects of the radioactive processes associated with U-bearing minerals

(metamictisation and uranium radiation). When observed in hand specimen, both TS1 and TS2 rock samples appear to be similarly oxidised, but the thin section and TIMA results show that these rock samples have different proportions of the altered minerals with the TS2 having high proportion of altered minerals compared to the TS1.

Albitisation alteration formed during the late-stage magmatic fluids alteration event that formed the oxidation halos in the E-type SLGs. According to Freemantle (2015), the common features characterising the late-stage magmatic-hydrothermal fluid alteration event are the development of myrmekite structures in plagioclase and albite (albitisation) over microcline. The petrography and mineral phase results for the TS2 rock sample show albite exsolution structures developing over microcline (Figures 4.18; 20; 29), and the development of myrmekite structures in plagioclase occurring throughout the oxidation halo but very prominent in the oxidation halo transitional zones (Figure 4.24). Haematisation is another type of alteration style that formed during the late-stage of magmatic-hydrothermal fluid alteration event. Oxidation halos formed when the Fe-enriched minerals were altered forming iron oxides, and their uneven distribution in the sample demarcates the oxidation halos boundaries identified by red colouration (Figure 4.6).

Chloritisation formed during the second alteration event that took place after the crystallisation of SLGs. Freemantle (2015) described the second alteration event as being characterised by the oxidation of uraninite forming uranophane phases, redistribution of the oxidised uranium minerals along fractures and the existing grain boundaries and intensive alteration of biotite to chlorite (Figure 4.26E). The mineralogy results show that in both TS1 and TS2 samples abundant uranophane phases occur in the feldspar-quartz contact zones, feldspar weak zones, radiating fractures and fractures of feldspar and quartz (Figures 4.14A-C; 22; 4.22.). Alteration results show that biotite phases are strongly chloritised in the oxidation halo transitional zones, and they have abundant inclusions of zircon, opaque phases and Iron oxides minerals such as haematite and titanite (Figures 4.19; 21A; 22; 33). All these features show that chloritisation alteration took place during the second alteration event, which further oxidised the oxidation halos.

Kaolinisation and sericitisation alteration styles observed in both TS1 and TS2 samples occurred during the later-stage hydrothermal alteration event, which according to Freemantle (2015) is characterised by the development of new mica, sericite and coarse muscovite in feldspar cleavages. The petrography, mineral phase maps and mineral phase association results show that TS1 was strongly sericitised and kaolinised compared to the TS2 as evidenced by the high occurrence of sericite and muscovite (sericitisation) (Figures 4.14B-C; 15A; 31) and kaolinite (kaolinitisation) (Figure 4.30) occurring in albite phases.

Metamictisation and uranium radiation alteration are common in both rock samples and formed due to the effects of radioactive processes associated with the U-bearing minerals. Metamictisation is characterised by the development of radiating fractures around U-bearing minerals such as zircon (Figures 4.16B; 22). The hand specimen observation of smoky quartz, the feldspar-quartz contact zones dark colouration in thin section (Figures 4.16A; 21A, C) and association between quartz and alteration phases characterises uranium radiation alteration, which transformed quartz into smoky quartz.

According to Corner and Henthorn (1978), the formation of oxidation halos also affected the distribution of U-bearing minerals. This observation is in line with the current research results which show that U-bearing minerals are unevenly distributed in the oxidation halo sections. Abundant U-bearing minerals are observed in the oxidation halo transition zones compared to other sections of the rock sample.

5.5 Texture relationship with alteration, colour variation and U-bearing minerals distribution

The results show that the distribution of U-bearing minerals, the rock colour variations and the intensity of various alteration styles are related to the textural change observed in both rock samples as discussed in sections 5.3 and 5.4. For instance, abundant U-bearing minerals and altered minerals phases are commonly observed in fine-textured sections of the samples. These observations mean that textural variation was one of the major petrographic features that controlled the movement of the hydrothermal fluids in various sections of the rock samples. Hydrothermal fluid movements directly influenced the extent of mineral alteration, which in turn affected the rock colour variations and the unequal distribution of U-bearing minerals observed in various sections of the rock samples. The change in rock texture from pegmatitic to fine texture resulted in the formation of the pegmatitic-fine grained textured interfaces. These interfaces acted as hydrothermal fluid traps, where more fluids were trapped and retained for a long period causing high alteration of the mineral phases characterising the fine-textured sections. One of the major effects of various alteration styles such as albitisation, chloritisation, sericitisation and metamictisation commonly observed in fine-textured sections of both TS1 and TS2 samples, is to promote the permeability of the rock through weakening the structure of the affected mineral phases (Alexandre, 2010; Kouske et al., 2012; Wilde, 2013; Wu et al., 2019) and also developing radial fractures (metamictisation) around some accessory U-bearing minerals. This also means that the fine-textured sections were further modified through alteration processes to become more permeable to the hydrothermal fluids' ingress for the mineral phases to be intensively altered.

5.6 Correctness, validity and importance of the research results

The results presented in this research are valid and correct. At least two methods were used in analysing the rock samples to produce valid and correct results. This helped to provide comparable results as well as complementing the results produced by one method with the other.

For textural features, mineral grain size measurements were determined through three techniques: The hand-specimen grain size measurement, the μ-XRF elemental maps and the full thin section images. Mineral grain size measurements from hand specimen and μ-XRF elemental maps provided mineral grain size distribution of the whole rock samples. Though hand specimen measurements provided a whole rock sample picture of mineral grain size distribution, mineral grain size measurements were not exact as those determined by the μ-XRF elemental maps and full thin section images because the exact mineral grain boundaries could not be easily traced. Therefore, the results from the three techniques complemented each other to give a better understanding of the rock samples' textural variations as discussed in section 5.2. Mineralogically, the rock samples were analysed through four techniques: The hand-specimen and thin section petrographic observations, the μ-XRF and TIMA analyses. All four techniques produced similar mineralogical results as discussed in the mineralogy section above. All this shows that the results presented in this research were valid and correct.

The petrological results presented in this research project are very important in understanding the origin, formation and distribution of the U-bearing minerals in the oxidation halos and their host rocks. The current research has documented detailed information on the types of rock texture occurring across the oxidation halos and their hosting rocks. It has also brought to light how textural variation relates to the distribution of U-bearing minerals, rock colour variations and the extent of

mineral phases alteration in various sections of the rock samples. Textural variations mainly controlled the movement of the hydrothermal fluids, which directly influenced the extent of alteration. Until this research, it was not well known that U-bearing minerals in the oxidation halos are unevenly distributed depending on rock texture as discussed in section 5.3 that abundant accessory uranium-bearing phases occur in the fine-textured oxidation halo transitional zones. The current research findings also have established that the occurring of the myrmekite structures within the plagioclase in the oxidation halos and diopside in both the oxidation halos and their hosting rocks can also be regarded as diagnostic features for uranium mineralisation in addition to the presence of smoky quartz noted by Nex (1997) and Kinnaird and Nex (2007).

5.7 Summary

The texture of oxidation halo and hosting rocks varies from fine to pegmatitic. The TS1 sections 2 and 5 (D-type) and TS2 sections 1 and 2 all are pegmatitic; the TS1 section 4 (D-type) and TS2 section 3 have coarse texture; and TS1 sections 1, 3, and 6 (D-type) and TS2 sections 4 and 5 have a fine texture.

The dominant rock-forming minerals for the TS2 sample are albite, orthoclase and quartz, whereas, for the TS1 sample are albite, diopside and quartz. Accessory minerals observed in both rock samples are anorthite, biotite, haematite/magnetite, muscovite, kaolinite, diopside (TS2), tin (TS2), and U-bearing minerals such as uraninite, uranophane, zircon, apatite (TS2), rutile (TS2) and titanite (TS2). High occurrence of U-bearing minerals is observed in highly altered fine-textured sections of both rock samples. In terms of colour variations, the light-dark variation observed in the D-type sample is mainly controlled by unequal distribution of smoky quartz in the sample sections, while in TS2, the light-red-pink colouration is controlled by uneven distribution of iron oxides such as hematite/magnetite, which also defines the oxidation halos boundaries. The results further show that there is a texture relationship with alteration of the mineral phases, the rock colour changes and the distribution of U-bearing minerals in the oxidation halos and their hosting rocks. The major role the texture of the rock played was to control hydrothermal fluid movements. The pegmatitic sections were more like fluid conduits compared with finer-grained portions which acted as acted as fluid traps, promoting a high rate of hydrothermal fluid alterations in the fine-textured sections as fluids were retained for a long period in these sections.

Several techniques were employed in analysing the rock samples to determine correct and valid results presented in this research. The results of this research are very important in understanding the textural variations, and how these textural changes are related to alteration of the mineral phases, the rock colour variations and the distribution of U-bearing minerals in the oxidation halos and their hosting rocks.

CHAPTER SIX

CONCLUSIONS AND RECOMMENDATIONS

6.1 Introduction

The aim of this research project is to document and interpret petrological features of the oxidation halos and their host rocks. Specific objectives of the research project are to describe and document the texture and mineralogy of the oxidation halos and their host granitic material and describe and document the distribution of U-bearing minerals in relation to the oxidation halos. Rock samples were analysed through hand specimen observations, petrographic analysis of thin sections, elemental mapping of major elements for TS2 using the Micro-XRF and TIMA for analysing mineral phases distribution in the rock samples.

6.2 Summary of the research findings

This section summarises the research findings, which address the research objectives to document the relationship between textural change and uranium mineralisation and distribution in the oxidation halos.

6.2.1 Mineralogy and rock colour variation

Mineralogically, the D-type SLG (TS1) is dominated by the following minerals: albite, diopside and quartz. Accessory minerals found in D-type are anorthite, biotite, muscovite, hematite/magnetite, kaolinite, tin and U-bearing minerals such as uraninite, uranophane and zircon. The common rock-forming minerals dominating the E-type SLG (TS2) are anorthite, orthoclase, albite and quartz. Biotite, muscovite, haematite/magnetite, diopside, calcite, tin and U-bearing minerals including apatite, titanite, uraninite, uranophane, rutile and zircon occur as accessory minerals in the TS2 sample. In terms of U-bearing minerals distribution, abundant U-bearing minerals occur in the highly altered fine-textured sections of both rock samples. In D-type SLG (TS1), abundant U-bearing minerals are observed in the fine-coarse textured TS1 sections 3 and TS1 section 4 (coarse textured) compared to the pegmatitic TS1 sections 2 and 5. In E-type SLG (TS2), the finely textured oxidation halo transitional zones have a higher occurrence of U-bearing minerals than the pegmatitic TS2 sections 1 and 2, and coarse-textured TS2 section 3. Within the oxidation halo transitional zones, abundant U-bearing minerals are observed in the TS2 section 4. Formation of uranium-bearing minerals in the oxidation halos and their hosting rocks was influenced by the oxidation of Fe rich minerals such biotite and magnetite, which provided Fe^{2+} to the REDOX system.

Both rock samples show colour variations, which are controlled by the distribution of uranium-bearing and iron oxide minerals such as hematite/magnetite. The appearance of D-type SLG (TS1) varies from light to dark. The dark appearance of TS1 sections 1, 3, and 4 is due to the high occurrence of U-bearing minerals in these sections, which altered more quartz into smoky quartz through the uranium radiation process. Whereas, the light appearance of TS1 sections 2 and 5 is due to low concentration of smoky quartz as these sections exhibit low occurrence of U-bearing minerals which resulted into transforming less quartz into smoky quartz as there was a low rate of uranium radiation. The light-red-pink appearance of E-type SLG (TS2) is a result of the uneven distribution of hematite/magnetite. The oxidation halo transitional zones with a high concentration of haematite/magnetite have a deep red appearance compared to the oxidation halo core zone which

has a relatively low concentration of haematite/magnetite. The deep red colouration in the oxidation halo transitional zones is also attributed to the alteration of the haematite/magnetite inclusions that commonly occur between the biotite sheets. Biotite in these sections is highly altered and associated with more iron oxides, which contributed to the deep red colouration observed in the oxidation halo transition zones.

6.2.2 Rock texture and structures

In both rock samples, the texture changes from fine to pegmatitic when moving across both rock samples. In the D-type SLG sample; TS1 sections 1, 3, and 6 have a fine texture, TS1 sections 2 and 5 have a pegmatitic texture and TS1 section 4 is coarse-textured. For the oxidation halo sample, the D-type section and oxidation halo core zone are all pegmatitic, the E-type section has a coarse texture, and the oxidation halo transitional zones have a fine texture. In terms of structural features, quartz chains and quartz clusters are common in both rock samples. Other common structural features found in the TS2 rock sample are the myrmekite structures observed within plagioclase and albite exsolution structures developing over microcline.

6.2.3 Alteration

The research results show that both rock samples were affected by a number hydrothermal of alteration events, including albitisation, chloritisation, haematisation, kaolinitisation, sericitisation, uranium radiation and metamictisation. Albitisation and haematisation formed during the first event of late-stage magmatic fluid alteration. Features characterising these alterations are red colouration (haematisation) and the presence of albite exsolution structures developing over the microcline. Chloritisation formed during the second event of hydrothermal alteration that took place after the crystallisation of the SLGs, and it is known by intensive biotite chloritisation to chlorite. Kaolinitisation and sericitisation took place during the later-stage hydrothermal alteration event, and they are characterised by sericite, muscovite (sericitisation) and kaolinite (kaolinitisation) occurring in association with albite. Metamictisation and uranium radiation formed due to the effects of radioactivity associated with U-bearing minerals. Metamictisation is characterised by the development of radial fractures around U-bearing minerals, whereas, uranium radiation is known by the occurrence of smoky quartz in hand specimen and feldspar-quartz contact boundaries dark colouration under thin section. All these alteration styles (albitisation, haematisation, chloritisation, kaolinitisation, sericitisation, metamictisation and uranium radiation) caused three major effects on the rock samples. Firstly, alteration led to the oxidisation of primary uranium minerals such as uraninite forming secondary uranium phases like uranophane, and Fe rich minerals to form iron oxides. Secondary, they further promoted the rock permeability by disturbing the structure of the affected mineral phases, which in turn helped to redistribute the U-bearing minerals for them to be unevenly distributed across the rock samples as established through this study. The last effect was that they influenced rock colour variations, with oxidation halos having red colouration because of haematisation and the light-dark appearance of the D-type SLG sample because of uranium radiation forming smoky quartz.

6.3 Conclusion remarks

Based on the results presented in this study, the following are the general concluding remarks about the petrographic features of the oxidation halos and their hosting rocks. In terms of mineralogy, the

major rocking forming minerals dominating the oxidation halos and their hosting rocks are anorthite and orthoclase (mainly the oxidation halo), albite and quartz. Dominant accessory minerals found in both rock samples are muscovite, biotite, haematite/magnetite, titanite, apatite, rutile and U-bearing minerals such as uraninite, uranophane and zircon. Most U-bearing minerals are found in the fine-textured sections occurring in the plagioclase (albite)-quartz contact boundaries, weak zones and fractures of albite and quartz, radial fractures and highly altered biotite. High abundance of uranium-bearing minerals in the oxidation halo transitional zones is a result of biotite, whose alteration helped to provide Fe^{2+} to the REDOX system to reduce and precipitate more uranium minerals. The structural features commonly observed in the oxidation halos are quartz chains and clusters, myrmekites in plagioclase and albite exsolution structures developing over microcline. The light-dark colouration of the D-type SLG sample is controlled by the unequal distribution of smoky quartz, whereas, the light-red-pink colouration observed in the oxidation halo sample is caused by the unequal distribution of the iron oxide minerals such as haematite and magnetite across the sample. The deep red colouration of oxidation halo transitional zones is influenced by the occurrence of abundant iron oxide phases, which are strongly associated with altered biotite. The presence of smoky quartz, diopside, anorthite, highly altered biotite and myrmekites are the diagnostic features for uranium mineralisation in the oxidation halos.

There is a textural change in the oxidation halos and their host rocks varying from fine to pegmatitic. In the oxidation halo sample, the D-type section and oxidation halo core zone are pegmatitic; the E-type section has a coarse texture and the oxidation halo transitional zones have a fine texture. Textural change played a very significant role in controlling movements of the hydrothermal fluids, which determined the extent of alteration in various sections of the rock samples. The pegmatitic-fine textured interfaces were fluid traps, retaining more fluids for a long period causing intensive alteration of mineral phases characterising the finely-textured sections. In the pegmatitic sections, hydrothermal fluids were not retained for a long period, hence their low alteration status. The various alteration styles both the rock samples were subjected to had three major effects: Iron rich and primary U-bearing minerals were oxidised to form iron oxides and secondary U-bearing minerals, respectively; promoted the rock permeability which in turn helped to redistribute the U-bearing minerals for them to be unevenly distributed across the rock samples and controlled the colour variations observed in both rock samples.

6.4 Recommendations

This study concentrated on establishing the petrological features of the oxidation halos and their hosting rocks. It has established how textural change is related to the distribution of U-bearing minerals, alteration of mineral phases and rock colour variations. But, less has been done on geochemical studies to establish how textural change affected the geochemistry of U-bearing minerals in the oxidation halos. Therefore, there is a need to undertake a similar study on the oxidation halo paying more attention to whole-rock geochemistry. The geochemical analytical techniques to be used in analysing the rock samples should be of high resolution and detection limits to determine the unclassified mineral phases as well as quantify the concentrations of U-bearing minerals across the rock samples, which have not been fully established through this study. A similar study should also consider having detailed local samples to produce more comparable results, and the rock samples should be collected from the same area because different locations might have different local geological settings resulting in the same rock sample having different petrological features.

REFERENCES

Abraham, I.M. 2009. *Geology and Spatial Distribution of Uranium Mineralization in the SK Anomaly Area, Rössing area, Namibia.* MSc. Thesis, the University of the Witwatersrand, pp8-30.

Alexandre, P. 2010. Mineralogy and geochemistry of the sodium metasomatism-related uranium occurrence of Aricheng South, Guyan. *Mineralium Deposita,* **45**, 351-376.

Anderson, H. and Nash, C. 1997. Integrated lithostructural mapping of the Rössing area, Namibia using high resolution aeromagnetic, radiometric Landsat data and aerial photographs. *Exploration Geophysics,* **28**, 185-191.

Ashworth, L. 2014. *Mineralised pegmatites of the Damara Belt, Namibia: Fluid inclusion and geochemical characteristics with implications for post-collisional mineralisation*. PhD. Thesis, the University of the Witwatersrand, pp1-34.

Ashworth, L., Kinnaird, K.A., Nex, P.A.M., Harris, C. and Müller, A.B. 2020. Origin of rare element-mineralized Damara Belt pegmatites: A geochemical and light stable isotope study. *Lithos,* **372-373**, 1-15.

Badenhorst, F.P. 1992. *The lithostratigraphy of areas 2115B and D in the Central Zone of the Damara Orogen, Namibia: with emphasis on facies changes and regional correlation*. Unpublished M.Sc. Thesis, University of Port Elizabeth, 124pp.

Barnes, J.F.H. 1981. *Some aspects of the Tectonic History of the Khan-Swakop region of the Damara Belt, Namibia*. PhD. Thesis, University of Leeds.

Barnes, J. and Hambleton-Jones, B. 1978. *A review of the geological and geochemical setting of uraniferous granites in the Damara Orogen.* Paper presented at the Unpublished Lecture to the International Atomic Energy Agency Working Group Meeting, Nancy, France.

Basson, I.J. and Greenway, G. 2004. The Rössing uranium deposit: a product of late-kinematic localisation of uraniferous granites in the Central Zone of the Damara Orogen, Namibia. *Journal of African Earth Sciences,* **38**, 413-435.

Berning, J. 1986. The Rössing Uranium Deposit, South West Africa/Namibia. In: Annhausser, C.R., Maske, S. (Eds.), Mineral Deposits of Southern Africa. Geological Society of South Africa, **Volume II**, 1819- 1832.

Berning, J., Cooke, R., Heimstra, S.A. and Hoffman, U. 1976. The Rössing Uranium Deposit, South West Africa. *Economic Geology*, **71**, 351-368.

Brandt, R. 1987. A revised stratigraphy for the Abbabis Complex in the Abbabis Inlier, Namibia. *South African Journal of Geology,* **90**, 314-323.

Bowden, P., Herd, D. and Kinnaird, J.A. 1995. The significance of Uranium and Thorium concentrations in pegmatitic leucogranites (alaskites), Rössing Mine, Swakopmund, Namibia. *Communications of Geological Survey of Namibia,* **10**, 43-49.

Briqueue, L., Lancelot, J.R., Valois, J. P. and Walgenwitz, F. 1980. Géochronologie U - Pb et genèse d'un type de minéralisation uranifère: les alaskites de Goanikontès (Namibie) et leur encaissant, *Bulletin Centre Research Exploration et Production. Elf. Aquitaine*, **4**, 759-811.

Collins, L.G. and Collins, B.J. 1998. The microcline-orthoclase controversy- can microcline be primary? Retrieved from. *http://www.csun.edu/~vcgeo005/Nr26Controversy.pdf.* (Accessed 23 December 2020). Accessed.

Corner, B. 1982. *An interpretation of the aeromagnetic data covering a portion of the Damara orogenic belt, with special reference to the occurrence of uraniferous granite*. PhD. Thesis, University of the Witwatersrand.

Corner, B. 1983. An interpretation of the aeromagnetic data covering the western portion of the Damara Orogen in South West Africa/Namibia. In: Miller, R.M0cG. (Ed.), *Evolution of the Damara Orogen of South West Africa*. Special Publication of the Geological Society of South Africa, **11**, 339-354.

Corner, B. 2000. Crustal framework of Namibia derived from magnetic and gravity data. *Henno Martin Commemorative Volume of the Communications of the Geological Survey of Namibia*, **12**, 13-20.

Corner, B. and Henthorn, D.I. 1978. Results of a palaeomagnetic survey undertaken in the Damara mobile belt, South West Africa, with special reference to the magnetization of the uraniferous pegmatitic gneisses. Report PEL-260 Pelindaba, Atomic Energy Board, South Africa.

Corvino, A.F. and Pretorius, L. E. 2013. Uraniferous leucogranites south of Ida Dome, central Damara Belt, Namibia: Morphology, distribution and mineralisation. *Journal of African Earth Sciences,* **80**, 60-73.

Cuney, M. and Kyser K. 2008. Recent and not-so-recent developments in uranium deposits and implications for exploration: Mineralogical Association of Canada Short Course Series, **39**, 258pp.

Cuney, M. 1980. Preliminary results on the petrology and fluid inclusions of the Rössing uraniferous alaskites. *Transactions of the Geological Society of South Africa*, **83**, 39-46.

Cuney, M. 1979. Preliminary results on the petrology and fluid inclusions of the Rössing uraniferous alaskites. *Transactions of the Geological Society of South Africa*, **83**, 39-46.

De Kock, G.S. and Botha, B.J.V. 1988. Komontwikkeling in die Damara-orogeen gedurende die afsetting van die Okomis-en Omusemaformasies aan die basis van die Swakopgroep, in die gebied suid-oos van Karibib, Namibia. *South African Journal of Geology,* **91**, 83-96.

Echlin, P. 2009. *Handbook of Sample Preparation for Scanning Electron Microscopy and X-Ray Microanalysis*. Cambridge Analytical Microscopy, United Kingdom.

Freemantle, G.G. 2015. *Primary Uranium Mineralisation of the Central Damara Orogen:* A *petrographic, geochemical and mineralogical account of the granite - hosted uranium deposits situated along the Swakop- and Khan River valleys.* PhD. Thesis, the University of the Witwatersrand, pp1-165.

Gray, T. 2015. The Geological Setting of Uranium Mineralisation in the Rössing Area, Namibia PhD Thesis, University of the Witwatersrand, Johannesburg, South Africa, unpublished. Herd, D.A. 1997 *Geochemistry and mineralisation of alaskite in selected areas of the Rössing Uranium Mine, Namibia*. M.Sc. Thesis, University of St. Andrews.

Henry, G. 1992. *The sedimentary evolution of the Damara Sequence in the lower Khan River valley, Namibia*. Unpublished Ph.D. Thesis, University of the Witwatersrand, Johannesburg.

Hoffmann, K.H. 1987a. Application of tectonostratigraphic terrane analysis in the Damara Province of central and northern Namibia. In: Hartnady, C.J.H. (Ed.). *Proceedings and Abstracts of the Alex L. du Toit Golden Jubilee Conference on Tectonostratigraphic Terrane Analysis*, 17 October, Cape Town, Precambrian Research Unit, University of Cape Town, 25-27.

Hoffmann, K.H. and Prave, A.R. 1996. A preliminary note on a revised subdivision and regional correlation of the Otavi Group based on glaciogenic diamictites and associated cap dolostones. *Communications of the Geological Survey of Namibia,* **11**, 77-82.

Hoffmann, K.H., Condon, D.J., Bowring, S.A. and Crowley, J.L. 2004. A U-Pb zircon date from the Neoproterozoic Ghaub Formation, Namibia: Constraints on Marinoan glaciation: Geology, 32, p. 817–820. Hoffman, P. F. 2005 On Cryogenian (Neoproterozoic) ice-sheet dynamics and the limitations of the glacial sedimentary record. *South African Journal of Geology,* **108**, 557-577.

Hrstka, T., Gottlieb, P., Skála, R., Breiter, K. and Motl, D. 2018. Automated mineralogy and petrology – applications of TESCAN integrated mineral analyser (TIMA). *Journal of Geosciences (Czech Republic)*, **63(1)**, 47-63.

Jacob, R.E., Corner, B. and Brynard, H.J. 1986. The regional geological and structural setting of the uraniferous granitic provinces of southern Africa. In: Annhausser, C.R., Maske, S. (Eds.), *Mineral Deposits of Southern Africa*. Geological Society of South Africa, **Volume II**, 1807-1818.

Kaur, P., Chaudhri, N., Hofmann, A.W., Raczek, I., Okrusch, M., Skora, S. and Baumgartner, L.P. 2012. Two-Stage, Extreme Albitisation of A-type granites from Rajasthan, NW India. *Journal of Petrology,* **5(5)**, 919-948.

Kerr, A. 1990. *The geochemistry of the Rössing leucogranites and several associated metasediments, Rössing, Namibia.* BSc Hons. Thesis, University of St. Andrews.

Kinnaird, J.A. and Nex, P.A.M. 2007. A review of geological controls on uranium mineralisation in sheeted leucogranites within the Damara Orogen, Namibia. *Applied Earth Science,* 116, 68-85.

Kinnaird, J.A. and Nex, P.A.M. 2016. Uranium in Africa. Episodes*,* **39**, 338-344.

Kouske, A.P., Suh, C.E., Ghogomu, R.T. and Ngako, V. 2012. Na-metasomatism and Uranium Mineralisation during a Two-Stage Albitisation at Kitongo, Northern Cameroon: Structural and Geochemichal Evidence. *International Journal of Geosciences,* **3**, 258-279*.*

Kruger, T. and Kisters, A. 2016. Magma accumulation and segregation during regional-scale folding: The Holland's dome granite injection complex, Damara belt, Namibia. *Journal of Structural Geology,* **89**, 1-18.

Manganese from Wikipedia, the free encyclopaedia. Retrieved from. *https://en.wikipedia.org/wiki/manganese#Physical_Properties.* (Accessed 31 March 2021). Accessed.

Marlow, A.G. 1983. Geology and Rb-Sr geochronology of mineralised and radioactive granites and alaskites, Namibia. 289 - 298. In Miller, R. McG. (Ed.) *Evolution of the Damara Orogen of South West Africa/Namibia*. Special Publication of the Geological Society of South Africa, **11**, 515pp.

Marlow, A.G.M. 1981. *Remobilisation and primary uranium genesis in the Damaran Orogenic belt.* PhD. Thesis, University of Leeds, 277pp.

Mathieu, L. 2018. Quantifying Hydrothermal Alteration- A review of methods. *Geosciences,* **8**, 245pp.

Mestres-Ridge, D. 1992. *An investigation into the controls on the distribution of betafite in the SH area, Rössing Uranium Mine, Namibia*. M.Sc. Thesis, University of St. Andrews.

Miller, R.McG. 1983a. Economic implications of plate tectonic models of the Damara Orogen. In: Miller, R. McG. (Ed.), Evolution of the Damara Orogen of South West Africa. Special Publication of the Geological Society of South Africa, **11**, 385-395.

Miller, R. McG. 2008. Neoproterozoic and early Palaeozoic rocks of the Damara Orogen. In Miller, R. McG. *The Geology of Namibia 2*, Ministry of Mines and Energy, Geological Survey, Windhoek, 13-1 - 13-410.

Moore, J. M. and McStay, J. H. 1990. The formation of allanite- (Ce) in calcic granofelses, Namaqualand, South Africa. *Canadian Mineralogist*, **28**, 77-86.

Mouillac, J.L., Valois, J.P. and Walgenwitz, F. 1986. The Goanikontes Uranium Occurence4in South West Africa/Namibia. In Anhaeusser, C.R. and Maske, S. (Eds.) 1986. *Mineral Deposits of Southern Africa*, **Volume II,** 1833-1843.

Munro, K., Inwood, N. and Turney, J. 2011. *National Instrument 43.101 Technical Document: GoanikonteUranium Project, Namibia* (Issue September 28).

Mc Dermott, P.F. 1987. *Granite petrogenesis and crustal evolution studies in the Damara Pan-African orogenic belt, Namibia.* PhD. Thesis, The Open University.

Longridge L., Gibson. R.L. and Kinnaird, J. A. 2009. Dome formation Mechanisms in the southwestern Central Zone of the Damara Orogen, Namibia. *Trabajos de Geología, Universidad de Oviedo,* **29**, 440-444.

Longridge, L. 2012. *Tectonothermal evolution of the southwestern Central Zone, Damara belt, Namibia. PhD Thesis*. University of the Witwatersrand, Johannesburg. 524pp.

Nex, P.A.M. and Kinnaird, J.A. 1995. Granites and their mineralisation in the Swakop River area around

Goanikontes, Namibia. *Communications of the Geological Survey of Namibia*, **10**, 51-56.

Nex, P.A.M. 1997. *Tectono-metamorphic setting and evolution of granitic sheets in the Goanikonte area, Namibia*. PhD. Thesis, University College Cork, National University of Ireland.

Nex, P.A.M., Kinnaird, J.A. and Herd, D.A. 2003. The occurrence, mineralogy and chemistry of betafite and pyrochlore from sheeted leucogranites of the Rössing area, Namibia:

implications for the composition of ceramics for radioactive waste disposal. *Economic Geology Research Institute Information Circular,* **374**, 1-34.

Nex, P.A.M., Kinnaird, J.A. and Oliver, G.J.H. 2001a. Petrology, geochemistry and uranium mineralisation of post-collisional magmatism around Goanikonte, southern Central, Damaran Orogen, Namibia. *Journal of African Earth Sciences,* **33**, 481-502.

Nex, P.A.M., Oliver, G.J.H. and Kinnaird, J.A. 2001b. Spinel-bearing assemblages and P-T-t evolution of the Central Zone of the Damara Orogen, Namibia. *Journal of African Earth Sciences,* **32**, 471-489.

Oliver, G.J.H. 1994. Mid-crustal detachment and domes in the central zone of the Damaran Orogen, Namibia. *Journal of African Earth Sciences,* **19**, 331-344.

Oliver, G.J.H. and Kinnaird, J.A. 1996. The Rössing-SJ Dome, central zone, Damara Belt, Namibia: an example of mid-crustal extensional ramping. *Communications of the Geological Survey of Namibia,* **11**, 53-64.

Reed, S.J.B. 2005. *Electron Microprobe Analysis and Scanning Electron Microscopy in Geology* (2nd Ed.). Cambridge University Press.

Rich, R.A., Holland, H.D. and Petersen, U. 1977. *Hydrothermal Uranium Deposits*. Elsevier, Amsterdam, 264pp.

Roesener, H. and Schreuder, C.P. 1994. Nuclear and Fossil Fuels-Uranium: Mineral Resources of Namibia. *Geological Survey of Namibia,* pp1-62.

Shanyengana, S.H., Fan, H., Xue, C., Shanyengana, E.S., Mapani, B., Shilongo, E. and Chen, J. 2020. An example of uraniferous leucogranites in the Rössing South-West deposit, Namibia. *Journal of African Earth Sciences,* **162**, 1-17.

Smith, D.A.M. 1965. The geology of the area around the Khan and Swakop Rivers in South West Africa. *Memoir of the Geological Survey of South Africa*, **1**, 113pp.

Spivey, M., Penkethman, A. and Culpan, N. 2010. Geology and Mineralisation of the Recently Discovered Husab Uranium Deposit, Namibia. Society of Economic Geologists, Inc. Special Publication, **15**, 729-746.

Tsuji, K., Nakano, K., Takahashi, Y., Hayashi, K. and Ro, C. 2012. X-ray Spectrometry. *Analytical Chemistry,* **84**, 636-668.

Valois, J.P. and Walgenwitz, F. 1979. Pétrographie des alaskites et de la série metamorphique de Goanikontes, Namibie. *Bull. Cent. Réch. Explor.-Prod., Elf Aquitaine DP,* **3**, 351-367.

Vincze, L., Vekemans, B., Brenker F.E., Falkenberg, G., Rickers, K., Somogyi, A., Kersten, M. and Adams, F. 2004. Three-Dimensional Trace Element Analysis by Confocal X-ray Microfluorescence Imaging. Analytical Chemistry, **76**, 6786-6791.

Walker, G.W. 1956. Host rocks and their alterations as related to uranium-bearing veins in the United States. United States Geological Survey. Retrieved from. *https://pubs.usgs.gov/tei/0638/report.pdf.* (Accessed 22 February 2021). Accessed.

Warwick, T. 2017. Micro-XRF in Geology. Retrieved from. *https://blue-scientific.com/micro-xrf-geology/.* (Accessed 2 November 2021). Accessed.

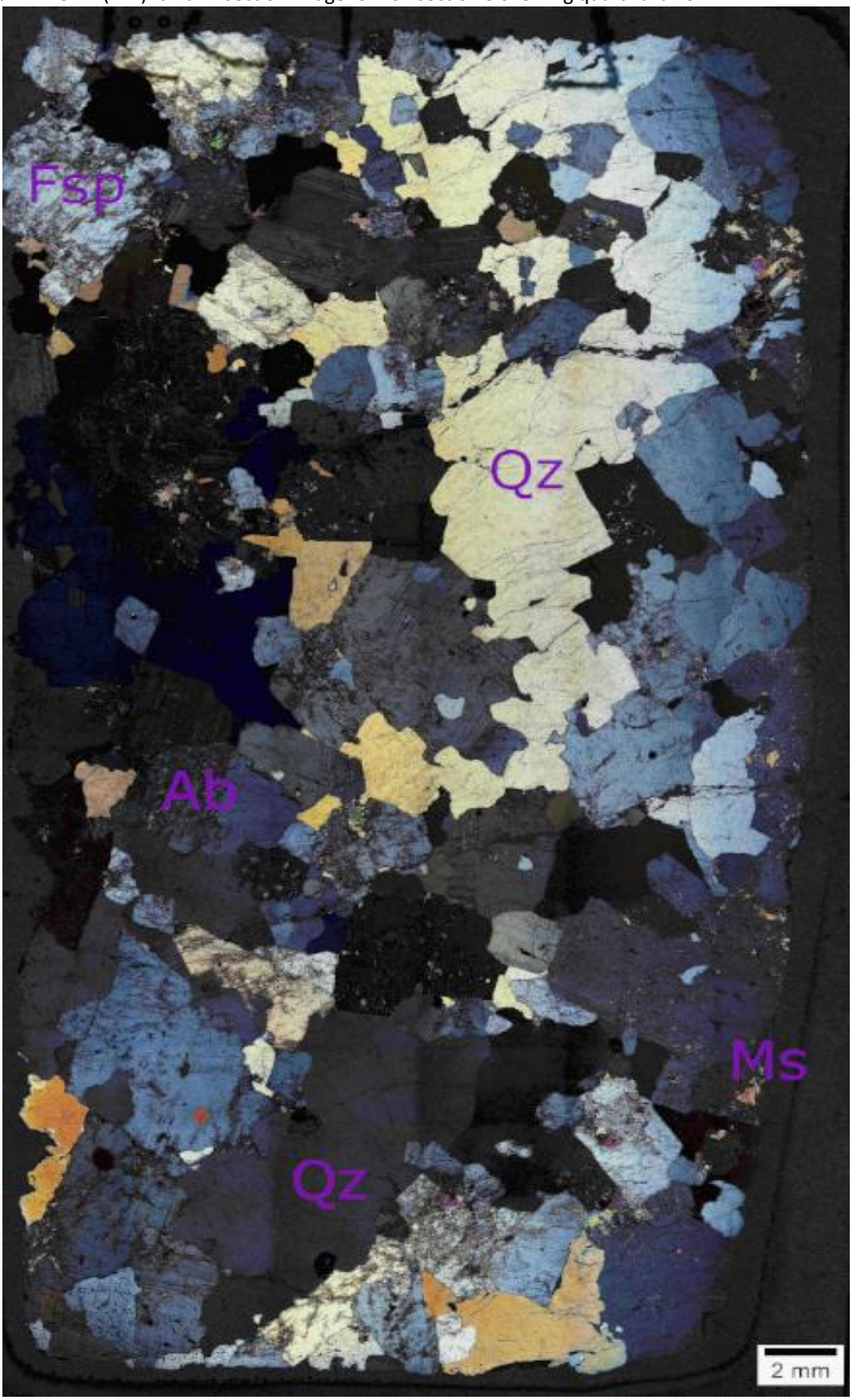
Waters, D. J. 1989. Metamorphic evidence for the heating and cooling path of granulites: Geological Society of London Special Publication, **43**, 357-363.

Wilde, A. 2013. Towards a Model for Albitite-Type Uranium. *Minerals,* **3**, 36-48.

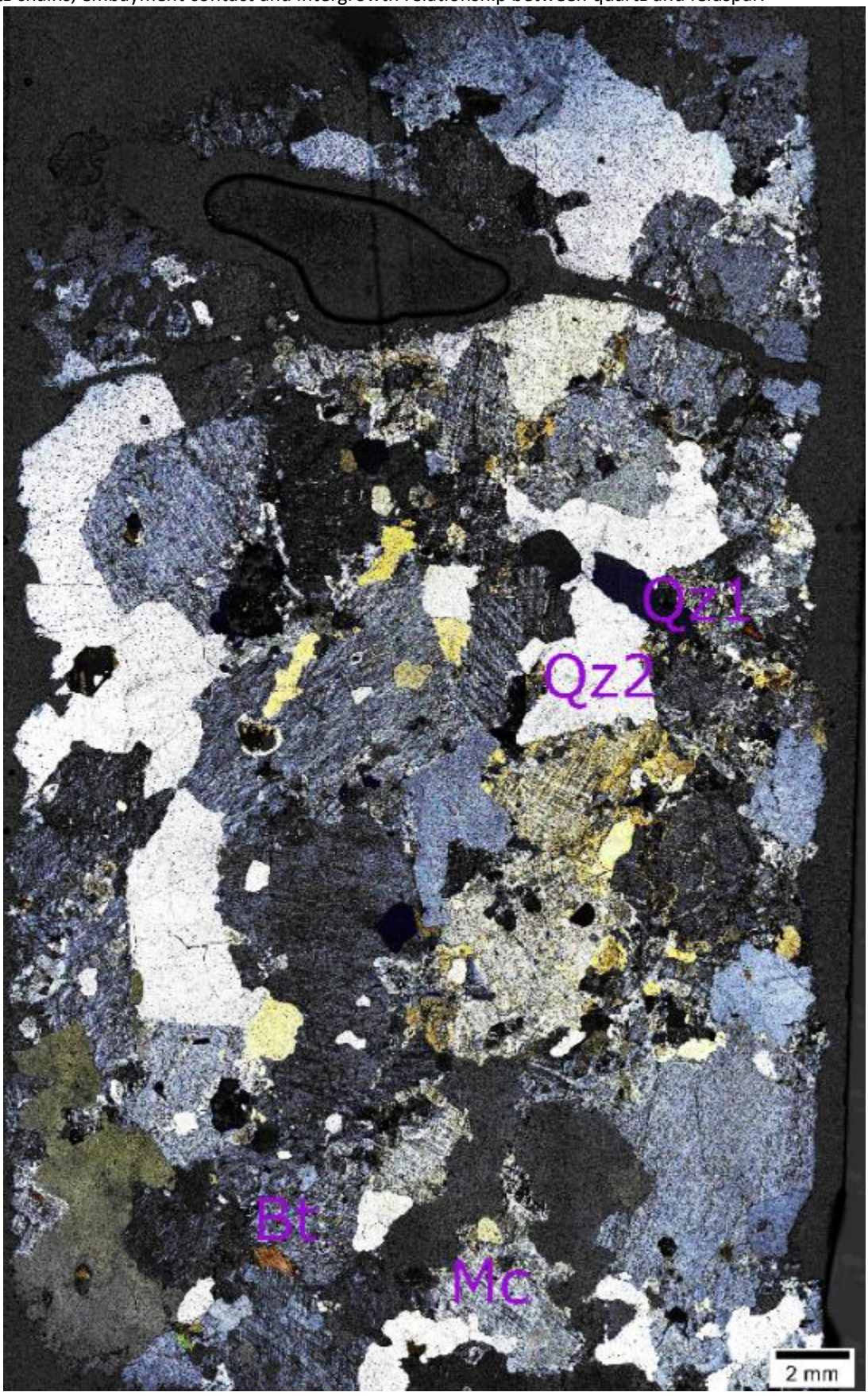
Wu, D., Pan, J., Xia, F., Huang, G. and Lai, J. 2019. The Mineral Chemistry of Chlorites and Its Relationship with Uranium Mineralization from Huangsha Uranium Mining Area in the Middle Nanling Range, SE China. Minerals, **9**, 199pp.

APPENDICES

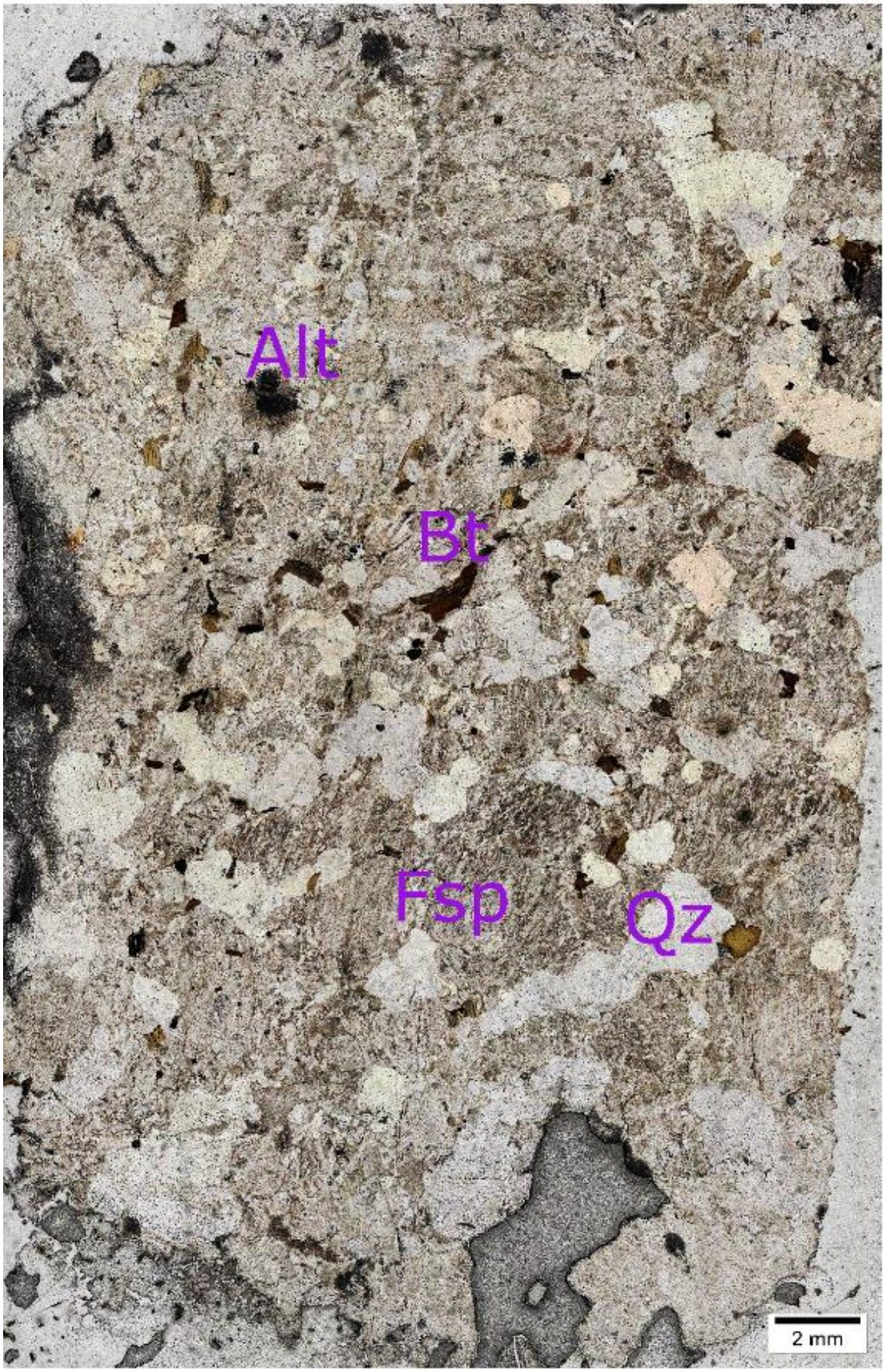
Appendix 1: TS1-7 (XPL) full thin section image for TS1 section 5 showing quartz chains



Appendix 2: TS2-4 (XPL) full thin section image for TS2 section 4 showing two forms of quartz (Q1 and Q2), quartz chains, embayment contact and intergrowth relationship between quartz and feldspar.



Appendix 3: TS2-5 PPL full thin section image for TS2 section 4 showing the distribution of biotite in section. Note: Alt- alteration, Alt- alteration, Fsp- feldspar, Qz- quartz.



Appendix 4: Hand-specimen mineral grain size measurements for TS1 and TS2

Hand specimen grain size measurements for TS1		
Rock sample section	Quartz (mm)	Feldspar (mm)
TS1 section 2	1, 2, 3, 4, 5, 5, 5, 5, 5, 6, 6, 6, 7, 7, 7, 8, 8, 8, 8, 10, 11, 11, 11, 12, 13, 18	3, 5, 5, 6, 7, 9, 9, 9, 10, 10, 11, 12, 12, 12, 13, 13, 13, 14, 15, 15, 16, 20, 23
TS1 section 3	1, 2, 2, 2, 2, 2, 2, 2, 2, 2, 2, 2, 2, 3, 3, 3, 3, 3, 3, 3, 3, 3, 4, 4, 4, 4, 4, 4, 4, 5, 5, 5, 6	2, 2, 3, 3, 3, 3, 3, 4, 4, 4, 4, 4, 4, 4, 4, 5, 5, 5, 5, 5, 5, 5, 5, 5, 5, 6, 6, 6, 7, 7, 8, 8
TS1 sections 4	2, 2, 3, 3, 4, 4, 5, 5, 5, 5, 5, 5, 5, 5, 6, 6, 6, 6, 7, 7, 7, 7, 8, 9, 10, 10, 10, 10	4, 4, 5, 5, 5, 5, 6, 6, 6, 6, 7, 7, 8, 8, 9, 9, 10, 10, 10, 10, 10, 10, 10, 11, 12, 14, 18
TS1 section 5	4, 5, 5, 5, 5, 5, 6, 6, 6, 7, 7, 8, 8, 8, 8, 9, 9, 9, 10, 10, 10, 10, 10, 10, 10, 10, 11, 11, 11, 11, 11, 11, 11, 11, 11, 12, 12, 12, 12, 13, 14, 15, 15, 15, 15, 15, 17, 18	5, 5, 6, 6, 7, 7, 8, 8, 8, 9, 9, 10, 10, 10, 10, 11, 11, 11, 11, 12, 13, 13, 13, 15, 15, 16, 18
Note: TS1 section 3 also represent TS1 sections 1 and 6		
Hand specimen grain size measurements for T2		
	Quartz (mm)	Feldspar (mm)
TS2 section 1	4, 5, 11, 12, 15, 25	1, 5, 7, 10, 10, 10, 10, 11, 15, 15, 18, 22, 25, 25, 30, 35
TS2 section 2 (oxidation halo core zone)	3, 5, 5, 5, 5, 5, 5, 5, 6, 6, 7, 7, 7, 8, 8, 8, 8, 8, 8, 9, 9, 9, 10, 10, 10, 10, 10, 10, 10, 10, 11, 11, 11, 11, 12, 12, 12, 14, 15, 15, 16, 16, 17, 18, 19, 20, 21	4, 5, 8, 10, 10, 10, 11, 12, 12, 14, 15, 16, 17, 19, 20, 21, 25, 28, 31
TS2 section 3	1, 2, 3, 4, 4, 4, 5, 5, 5, 5, 5, 5, 5, 5, 5, 5, 5, 5, 5, 5, 6, 6, 6, 6, 7, 7, 7, 7, 7, 7, 7, 8, 8, 8, 9, 9, 11, 11, 12, 14, 14	1, 2, 3, 5, 5, 5, 5, 6, 6, 6, 7, 7, 8, 9, 10, 10, 10, 10, 11, 11, 11, 12, 13, 14, 15, 15, 18

Appendix 5: Descriptive statistics summary for TS1 and TS2 mineral size measurement results.

	Average (mm)		Modal range (mm)		Range (mm)	
Rock sample section	Qz	Fsp	Qz	Fsp	Qz	Fsp
TS1 section 2	9	11	5-10	10-23	1-18	3-23
TS1 section 3	3	5	2-5	2-5	1-6	2-8
TS1 sections 4	6	8	5-10	5-10	2-10	4-18
TS1 section 5	10	13	10-18	10-18	4-18	5-18
TS2 section 1	12	16	10-25	10-35	4-25	1-35
TS2 section 2	14	16	10-21	10-31	3-21	4-31
TS2 section 3	6	8	5-10	5-10	1-14	1-18

Appendix 6: Mineral grain size measurements (mm) for TS2 sections using Micro-XRF elemental map

	Quartz (Si)	Orthoclase (K)	Anorthite (Ca)
TS2 section 1	3, 4, 5, 5, 6, 6, 6, 8, 8, 9, 9, 10, 11, 11, 11, 11, 35, 44	2, 5, 6, 8, 8, 9, 11, 11, 13, 15, 15, 23, 24, 32	3, 3, 4, 5, 8, 9, 11, 14, 15, 16, 18
TS2 section 2	2, 3, 3, 4, 4, 5, 6, 6, 8, 8, 8, 9, 9, 9, 10, 11, 12, 15, 15, 16, 24, 27, 27, 44, 47	6, 17, 22, 31, 37, 42, 55	3, 3, 3, 4, 5, 5, 5, 5, 6, 6, 7, 8, 11
TS2 section 3	3, 5, 5, 5, 6, 7, 7, 8, 8, 8, 8, 8, 9, 10, 11, 13, 15	5, 5, 5, 5, 5, 6, 6, 7, 7, 7, 8, 9, 9, 10, 10, 11, 12, 13, 20	4, 4, 4, 4, 4, 5, 5, 5, 5 6, 6, 7, 7, 7, 8, 8, 8, 9, 11
Ts2 section 4	2, 3, 3, 3, 4, 4, 4, 4, 4, 4, 4, 4 4, 4, 4, 4, 4, 4, 5, 5, 5, 5, 6, 6 6, 6, 7, 7, 7, 9, 9, 9, 9, 12, 12	3, 3, 4, 4, 4, 4, 4, 4, 4, 4, 4, 4, 5, 5, 5, 5, 5, 5, 5, 5, 5, 6, 6, 6, 7, 7, 7, 7, 7, 7, 8, 9, 9, 10	2, 2, 2, 2, 3, 3, 3, 3, 3, 3, 3, 3, 3, 3, 3, 4, 4, 4, 4, 5, 5, 6, 6, 6, 7, 7
TS2 section 5	2, 2, 2, 2, 2, 3, 3, 3, 3, 3, 3, 3, 4, 4, 4, 4, 4, 4, 4, 4, 4, 4, 5, 5, 6, 6, 6, 7, 7, 8, 9, 10, 17, 18, 22	2, 2, 2, 2, 3, 3, 3, 3, 4, 4, 4, 4, 5, 5, 5, 5, 5, 5, 6, 6, 6, 7, 8, 9 10, 11, 12, 15	2, 2 2, 3, 3, 4, 4, 4, 4, 4, 5, 6, 6, 6, 7, 8, 8

Appendix 7: TS2 descriptive statistic results for mineral grain sizes (mm)

	TS2 section 1			**TS2 section 2**			**TS2 section 3**			**TS2 section 4**			**TS2 section 5**		
	Qz	Or	An	Qz	Or	An	Qz	Or	An	Qz	Or	An	Qz	Or	An
Mean	12	14	10	14	34	5.8	8.4	8.7	6.3	4.9	5.0	4.1	5.9	6.0	4.8
Mode range	10-44	10-32	10-18	10-47	10-55	5-10	5-10	5-10	5-10	2-5	2-5	2-5	2-5	2-5	2-5
Range	3-44	2-32	3-18	2-47	2-55	3-11	3-15	5-20	4-11	2-12	3-10	2-7	2-22	2-14	2-8
Count	17	13	10	24	6	12	16	18	18	34	34	35	35	27	17

Note: Qz- quartz, Or-orthoclase, An- anorthite

Appendix 8: Mineral grain size measurements for TS1 using thin-section full images

Rock sample section	Grain size (mm)	
	Quartz	Feldspar
TS1 section 2 (TS1-1)	1, 1, 2, 3, 4, 4, 5, 5, 6, 6, 6, 7, 8, 9, 14	2, 3, 4, 6, 7, 7, 7, 8, 9, 9, 11, 15, 16
TS1 section 3 (TS1-2)	1, 1, 1, 1, 1, 1, 1, 1, 1, 2, 2, 2, 2, 2, 2, 2, 2, 3, 4, 4, 4, 4, 4, 5, 5, 5, 7, 7, 10, 12, 13	1, 1, 2, 2, 2, 2, 2, 2, 2, 2, 2, 2, 2, 2, 3, 3, 3, 4, 4, 4, 4, 4, 4, 4, 5, 5, 5, 5, 5, 5, 5, 5, 6, 6, 6, 6, 9, 11
TS1 section 4 (TS1-5)	1, 1, 1, 2, 2, 2, 2, 3, 3, 3, 5, 5, 5, 5, 7, 7, 8, 10, 10, 11, 12, 17	1, 1, 1, 1, 2, 2, 2, 2, 2, 2, 2, 3, 4, 4, 5, 5, 5, 5, 6, 6, 6, 6, 7, 7, 8, 10, 13
TS1 section 5 (TS1-7)	2, 3, 3, 3, 3, 5, 5, 5, 6, 6, 8, 10, 12, 13, 13, 14, 22	3, 4, 4, 4, 5, 5, 5, 6, 6, 8, 8, 8, 8, 8, 9, 10, 11, 13

Appendix 9: Descriptive statistics summary for TS1 mineral size measurement results

Sample section	Average grain size (mm)		Mode range (mm)		Range (mm)	
	Qz	Pl	Qz	Pl	Qz	Pl
TS1-1 (TS1 section 2)	6	8	5-10	5-10	1-14	2-16
TS1-2 (TS1 section 3)	4	4	2-5	2-5	1-13	1-11
TS1-5 (TS1 section 4)	8	7	5-10	5-10	1-17	1-13
TS1-7 (TS1 section 5)	8	7	10-22	5-10	2-22	3-13

Appendix 10: Mineral grain size measurements for TS2 using full thin section images

Rock sample section	Grain size (mm)	
	Quartz	Feldspar
TS2 section 1 (TS2-1)	1, 2, 2, 2, 3, 4, ,4, 5, 7, 11, 11, 12, ,13, `19	11, 12, 17, 20, 30
TS2 section 2 (TS2-4)	1, 1, 1, 1, 1, 1, 1, 1, 2, 2, 2, 2, 2, 2, 2, 2, 3, 3, 3, 4, 5, 5, 6, 6, 8, 8,9, 13, 14, 16	3, 6, 6, 7, 7, 9, 11, 11, 11, 16, 23
TS2 section 3 (TS2-6)	1, 1, 2, 2, 2, 2, 2, 2, 2, 3, 3, 3, 3, 3, 4, 5, 5, 6, 7, 7, 8, 8, 14, 14, 14	2, 2, 3, 3, 3, 3, 4, 4, 4, 5, 5, 5, 5, 6, 6, 6, 6, 6, 6, 6, 7, 8, 10, 13
TS2 section 4 (TS2-5)	1, 1, 1, 2, 2, 2, 2, 2, 2, 2, 3, 3, 3, 4, 4, 5, 5, 6, 7, 12	1, 2, 3, 3, 3, 3, 4, 4, 4, 5, 5, 5, 5, 7, 7, 9
TS2 section 5 (TS2-9)	1, 2, 2, 2, 2, 2, 2, 2, 3, 3, 3, 3, 3, 3, 3, 3, 3, 3, 3, 4, 4, 4, 5, 5, 5, 9, 9,	4, 4, 45, 5, 6, 10, 13, 22, 23

Appendix 11: Descriptive statistics summary for TS1 mineral size measurements using full thin section images

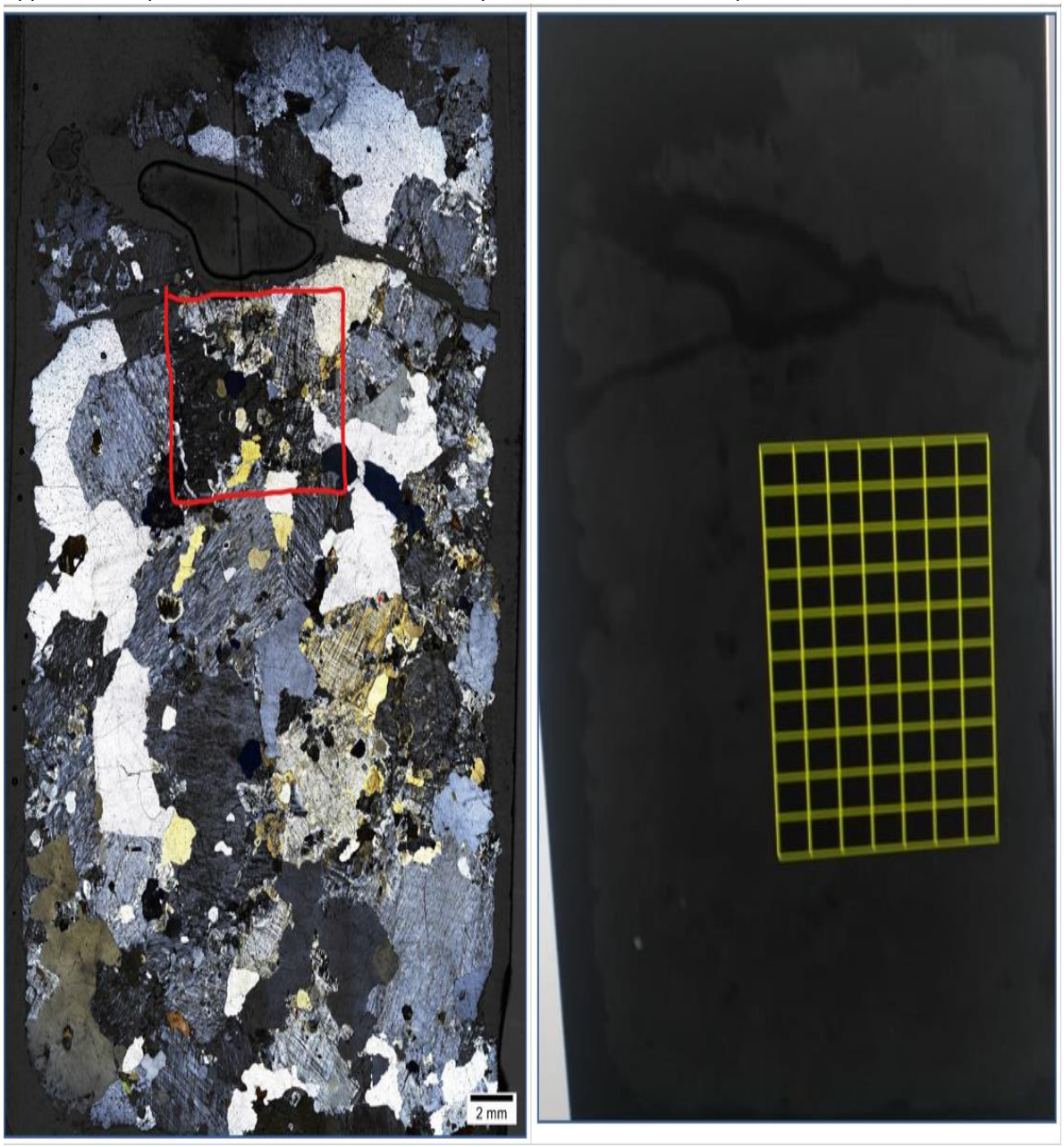
Sample section	Average grain size (mm)		Modal range (mm)		Range (mm)	
	Qz	Fsp	Qz	Fsp	Qz	Fsp
TS2-1 (TS2 section 1)	7	18	>10	>10	1-19	11-30
TS2-4 (TS2 section 2)	4	10	2-5	>10	1-16	3-23
TS2-6 (TS2 section 3)	4	5	2-5	5-10	1-14	2-13
TS2-5 (TS2 section 4)	3	4	2-5	2-5	1-12	1-7
TS2-9 (TS2 section 5)	3	4	2-5	4-5	1-9	4-23

Appendix 12: TS1 and TS2 mineral phases proportions (%) summary

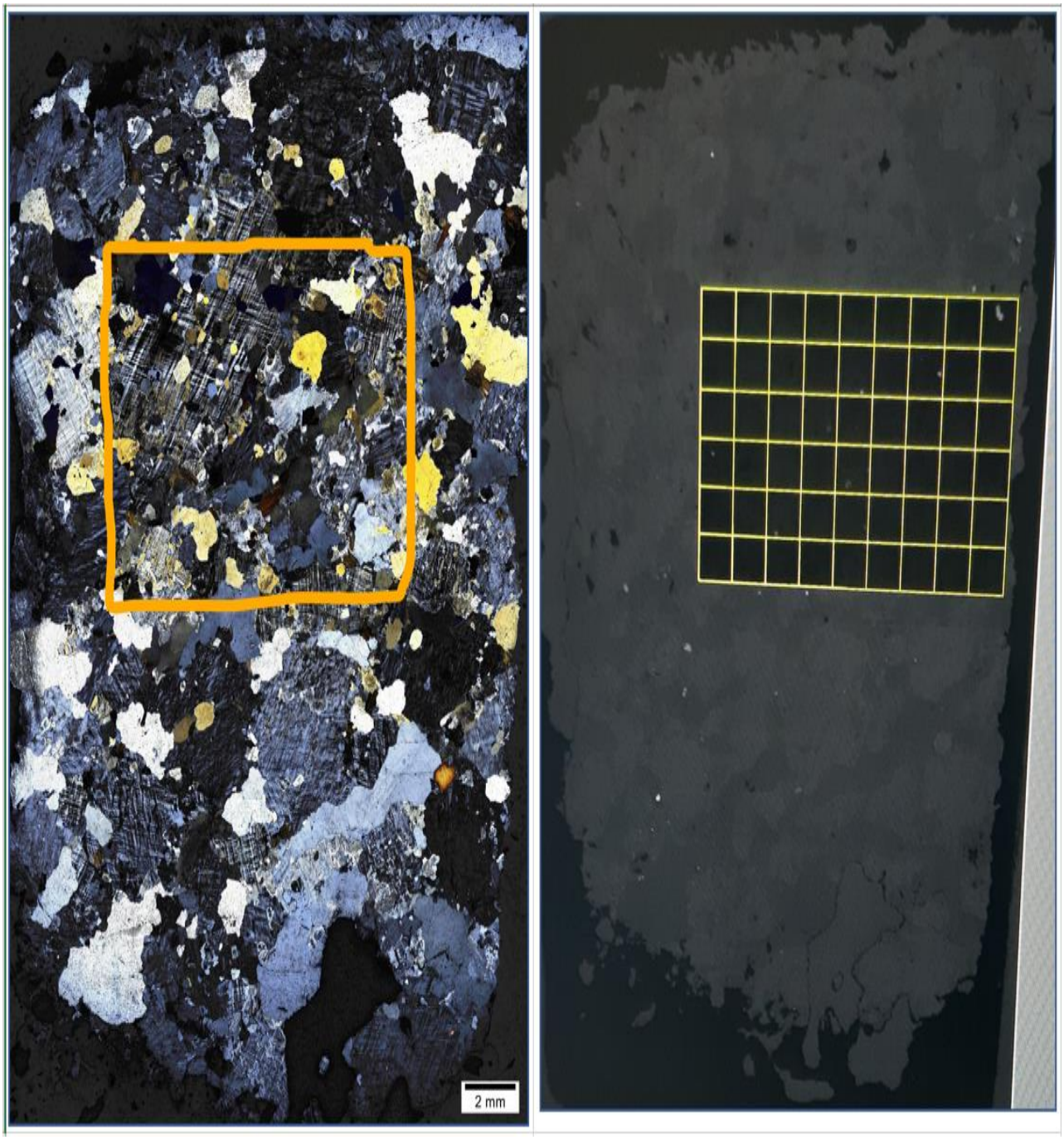
Rock sample Section	An	Or	Ab	Dio	Bt	Ms	Alt	Zrn	Hem	Qz	Urn	Total
TS1 section 3 (TS1-2)	0.2	1.8	54	0.0	0.0	1.5	0.5	0.1	0.4	41	0.0	99
TS1 section 4 (TS1-5)	0.4	0.1	15	34	0.0	0.8	1.4	0.0	0.0	44	0.0	96

TS2 section 2 (TS2-4)	2.2	41	28	0.0	0.3	0.1	0.7	0.0	0.0	27	0.0	99
TS2 section 3 (TS2-6)	1.3	40	28	0.0	1.0	0.1	0.6	0.0	0.0	29	0.0	99
TS2 section 4 (TS2-5)	1.8	38	26	0.0	2.9	0.1	1.1	0.1	0.1	29	0.1	99
TS2 section 5 (TS2-9)	2.0	41	24	0.0	0.5	0.1	0.5	0.0	0.1	33	0.0	100

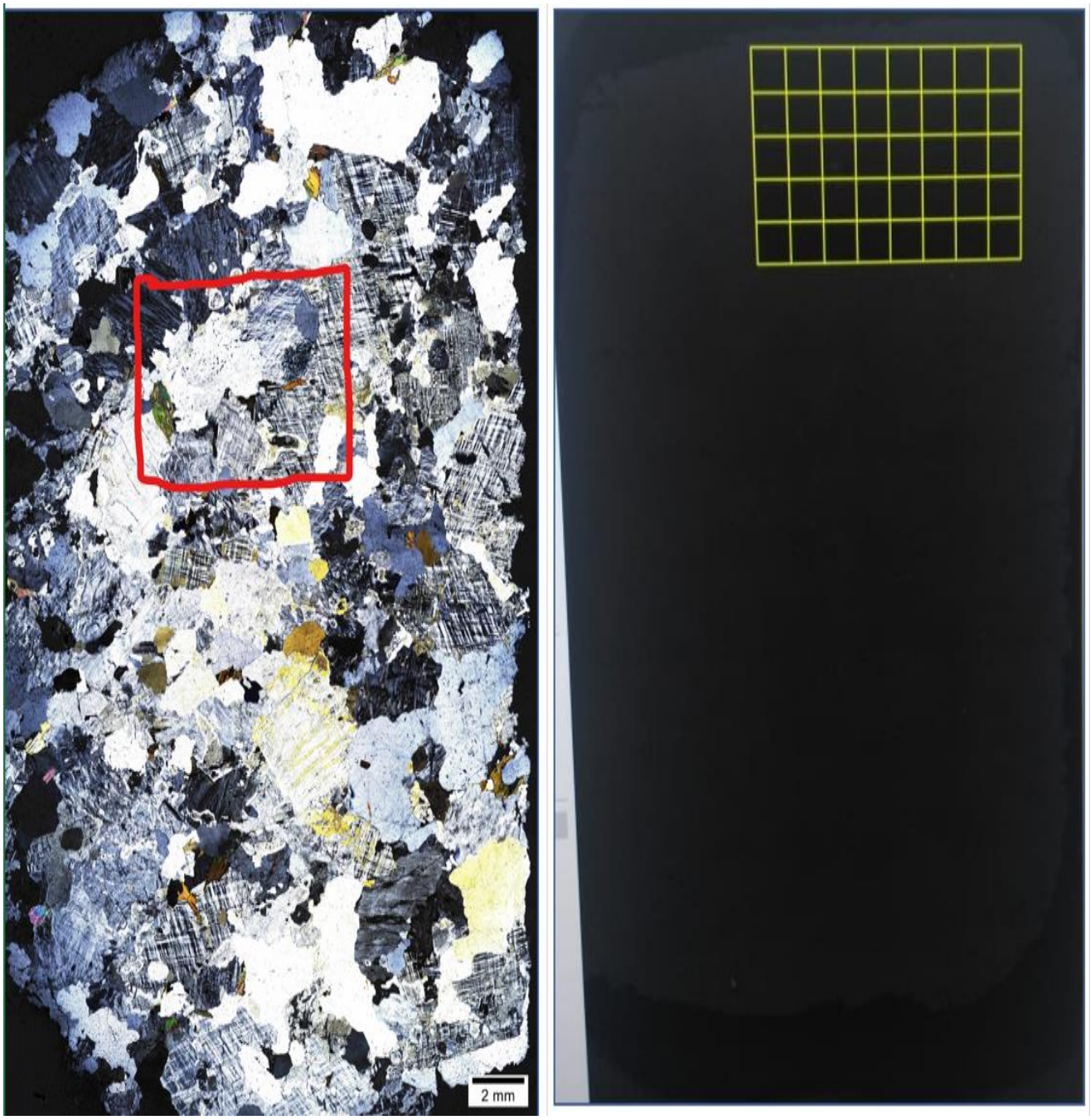
Appendix 13: Specific areas chosen for TIMA analysis from various rock sample sections of TS1 and TS2



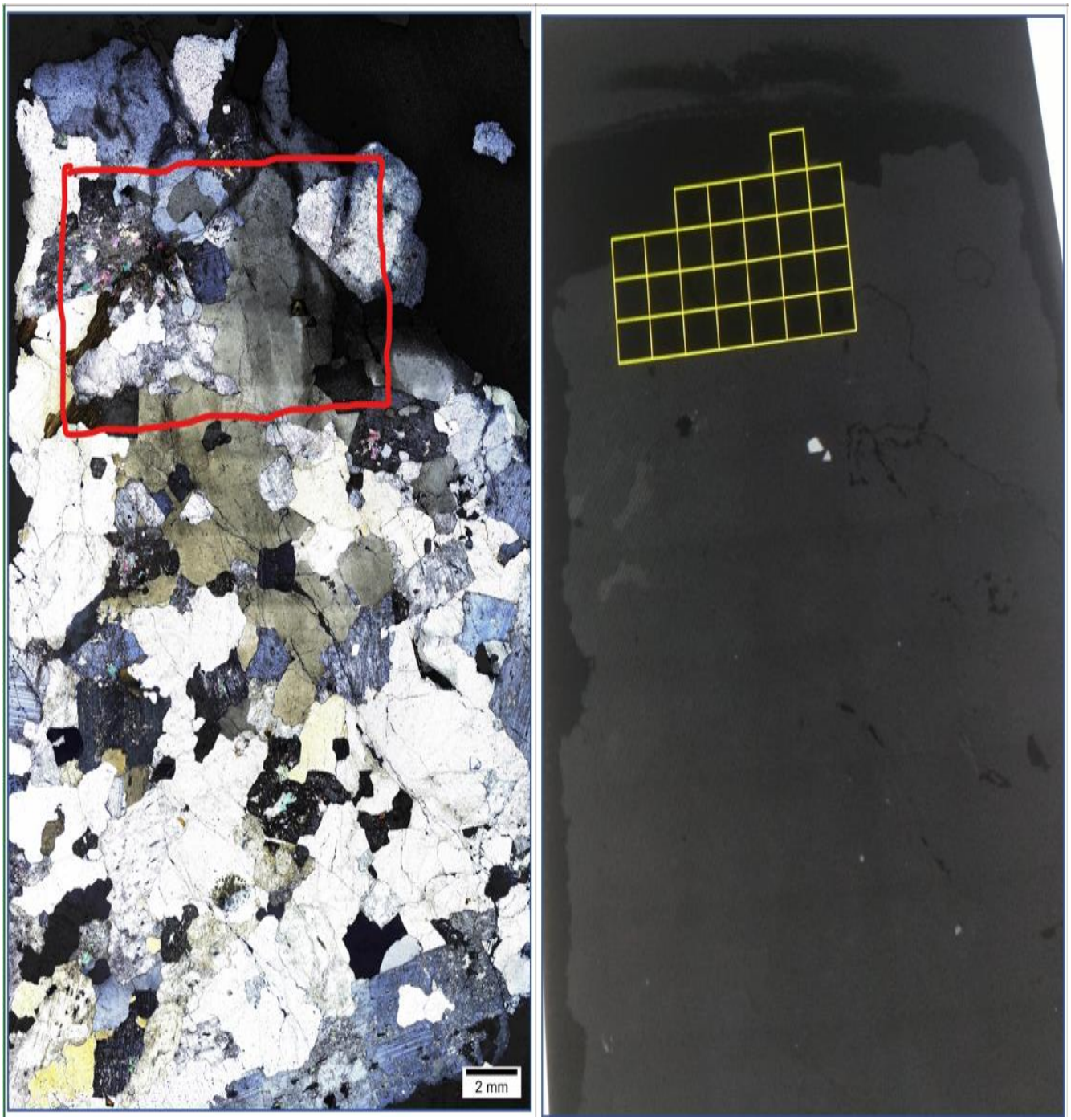
A. TS2-4 domain of TS2 section 2 showing the selected area for TIMA analysis



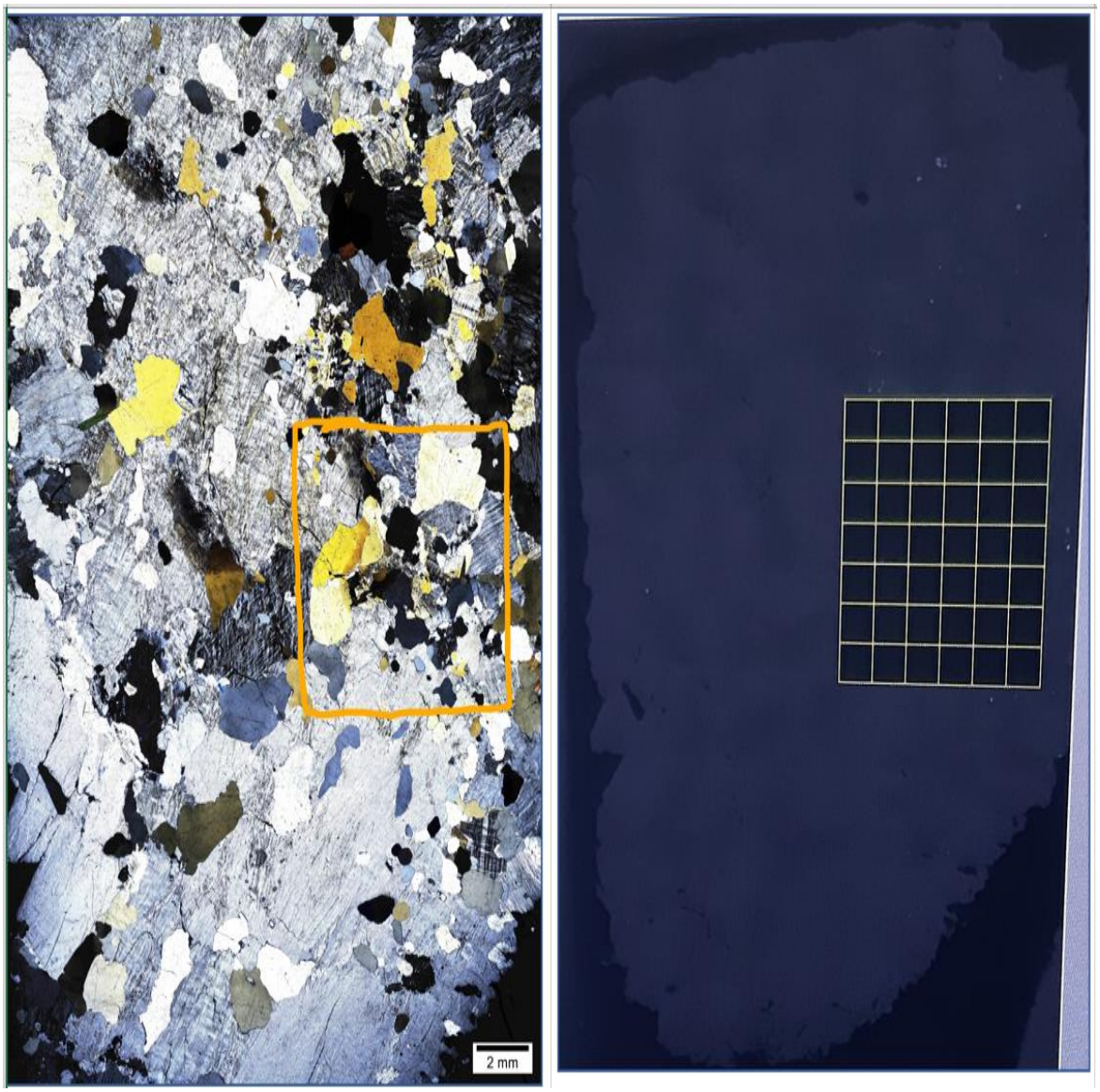
B. TS2 section 4 (TS2-5) full thin section showing the selected area for TIMA analysis



C. TS2 section 3 (TS2-6) shows the area selected for TIMA analysis



D. TS1 section 4 (TS1-5) shows the chosen domain for TIMA analysis. Note: The targeted area was missed during the analysis and this might have affected the results.



E. TS2 section 5 (TS2-9) shows the selected domain of the thin section for TIMA analysis